Danijel Obadic, BSc.

Dynamic Effects of Out-Of-Round Wheels

Correlations between Geometric Features of Out-Of-Roundness and their Dynamic Effects

Master Thesis

to achieve the university degree of

Master of Science

Master Program Mechanical Engineering

submitted at

Graz University of Technology

Supervisors

Ass.Prof. Dipl.-Ing. Dr.techn. Christian Moser

Institut für Thermische Turbomaschinen und Maschinendynamik, TU Graz

Björn Olaf Kämpfer

Siemens Mobility GmbH

Graz, June 2019

Acknowledgements

This thesis was created at the Institute of Thermal Turbomachinery and Machine Dynamics, within the Department of Structural Durability and Railway Technology, of the Faculty of Mechanical Engineering and Economic Sciences at Graz University of Technology, in cooperation with the Siemens Mobility GmbH competence center for bogies in Graz. Bogies for all classes of railway vehicles, ranging from light rail to locomotive, are designed and manufactured at this site.

Many people have provided their advice and expertise in their respective fields to help with the creation of this thesis, which I am very thankful for. First and foremost, I want to thank my supervising professor, Ass. Prof. DI Dr. Christian Moser (Department of Structural Durability and Railway Technology, TU Graz), for the supervision of this thesis and the input he has given me, which is a result of his many years of experience. Furthermore, I want to express my gratitude to Björn Kämpfer (Siemens Mobility GmbH), who was my main contact person at Siemens Mobility and who has given me a lot of input and guidance. All other employees at Siemens Mobility, especially in the Vehicle Dynamics working group, who have helped me acquire the measurement data, helped with their expertise in multibody simulation and provided me with the measuring equipment for the Eigenfrequency measurement also deserve my sincere thanks.

I would also like to take this opportunity to thank my parents for their encouragement during my time at university and for always supporting me in my decisions. I also want to thank my girlfriend Sandra for always supporting me.

Statuary Declaration

I declare that I have authored this thesis independently, that I have not used other than the declared sources / resources, and that I have explicitly marked all material which has been quoted either literally or by content from the used sources. The text document uploaded to TUGRAZonline is identical to the present master thesis.

Eidesstattliche Erklärung

Ich erkläre an Eides statt, dass ich die vorliegende Arbeit selbstständig verfasst, andere als die angegebenen Quellen / Hilfsmittel nicht benutzt, und die den benutzten Quellen wörtlich und inhaltlich entnommenen Stellen als solche kenntlich gemacht habe. Das in TUGRAZonline hochgeladene Textdokument ist mit der vorliegenden Masterarbeit identisch.

Graz, _____ _____

Date *(Datum)* Signature *(Unterschrift)*

Abstract

Train wheels are subjected to extremely high loads and stresses in service and characteristic damages and wear patterns occur as a result, one example are flats. The decision whether a damage or wear pattern is permissible or whether the wheels needs to be repaired or discarded is an important one, both from the standpoint of operational safety and economic efficiency. Operating within the bounds of the current European standard for the maintenance of wheelsets, EN15313:2016, this decision can only be made after each wheel has been inspected by a technician. Limit values prescribed by the standard must not be exceeded. The limit values are geometrical properties of damages to the wheel tread and radius deviations around the entire circumference. With the rise of condition-based maintenance and increasing availability requirements, a new approach for the assessment of the permissibility of wheel defects is required. Reviewing each wheel separately is far from ideal from an economic standpoint, it is also not clear whether the current limits even ensure the limitation of loads on the entire vehicle-track system. Furthermore, defects that are detrimental to both the vehicle and track are only detected during maintenance, possibly incurring damages before they are identified.

To help make a step towards condition-based maintenance for wheels, the dynamic effects of unround wheels in general were investigated. In the next step, existing automatic monitoring systems making use of those effects to detect and assess out-of-round wheels were examined within the scope of a market analysis. Especially the effects of flats and polygonization were studied. A multibody simulation model was built and validated with axle box acceleration measurements produced by a flat on a commuter train.

A search for a correlation between the length of a flat and the axle box acceleration it produces, as well as a correlation between the maximum radius deviation of a polygonized wheel and the axle box acceleration it produces was performed. It was shown that a direct correlation between geometric properties of wheel defects and the axle box accelerations they produce does not exist because of the strong influence of the track properties and other parameters. From this, it was further elaborated that the limits from EN15313 in their current form do not necessarily limit the loads produced by out-of-round wheels and that the introduction of additional acceleration limit levels is a viable alternative.

Kurzfassung

Räder von Schienenfahrzeugen sind im Betrieb extrem hohen Belastungen unterworfen, durch die sich charakteristische Schäden und Verschleißmuster bilden, beispielsweise Flachstellen. Die Bewertung der Zulässigkeit solcher Schäden und Verschleißerscheinungen und die Entscheidung über die Reparatur oder Entsorgung sind wichtige Faktoren für die Betriebssicherheit und Wirtschaftlichkeit. Um sich bei dieser Entscheidung innerhalb der Grenzen der aktuellen Europäischen Norm zur Instandhaltung von Radsätzen EN15313:2016 zu bewegen, müssen die Räder in regelmäßigen Abständen von einem technischen Sachverständigen untersucht werden. Dabei wird überprüft, ob die von der Norm vorgegebenen Grenzwerte eingehalten werden. Diese Grenzwerte sind geometrische Eigenschaften von Laufflächenschäden und Rundlaufabweichungen um den gesamten Radumfang. Mit der steigenden Verbreitung von zustandsabhängiger Instandhaltung und steigenden Verfügbarkeitsanforderungen an Fahrzeuge wird ein neuer Ansatz für die Bewertung der Zulässigkeit von Radunrundheiten benötigt. Eine manuelle Untersuchung jedes einzelnen Rades ist aus wirtschaftlicher Sicht nicht optimal. Zudem ist unklar, ob die derzeitigen Grenzwerte auch eine Begrenzung der Belastungen mit sich bringen. Außerdem können Unrundheiten meist nur bei geplanter Instandhaltung festgestellt werden und in den Instandhaltungsintervallen Schäden an Fahrzeug und Strecke hervorrufen.

Um die Einführung zustandsabhängiger Instandhaltung für Radsätze voranzutreiben, wurden im Rahmen dieser Arbeit die allgemeinen dynamischen Effekte von Radunrundheiten untersucht. Im Zuge einer Marktrecherche wurden bestehende, automatische Radsatzinspektionssysteme analysiert, die die zuvor untersuchten Effekte zur Erkennung und Bewertung von Radunrundheiten nutzen. Im Speziellen wurden dabei Flachstellen und Polygonisierung untersucht. Ein Mehrkörpermodell wurde aufgebaut und für die Simulation von Flachstellen mit maximalen Achslagerbeschleunigungen validiert, die an einem Triebzug mit Flachstelle gemessen worden waren.

Eine mögliche Korrelation zwischen der Länge einer Flachstelle und den entstehenden Achslagerbeschleunigungen, als auch eine mögliche Korrelation zwischen einer Rundlaufabweichung einer Polygonisierung und den entstehenden Achslagerbeschleunigungen wurde gesucht. Es konnte gezeigt werden, dass eine direkte Korrelation zwischen geometrischen Eigenschaften einer Radunrundheit und den Achslagerbeschleunigungen aufgrund des starken Einflusses von Streckenparametern und anderer Faktoren nicht existiert. Daraus wurde weiter geschlossen, dass die Grenzwerte der Norm EN15313 in ihrer derzeitigen Form nicht notwendigerweise zu einer Begrenzung der Belastungen führen, die durch eine Unrundheit hervorgerufen werden, und dass die Einführung zusätzlicher Beschleunigungsgrenzwerte eine mögliche Alternative wäre.

Content

Glossary of Symbols, Terms and Abbreviations

Symbol [unit]	Description
c_r	Rail pad stiffness (two-mass track model)
c_b	Ballast stiffness (two-mass track model)
c_h	Contact stiffness in the wheel-rail contact, calculated with the *Hertzian* [1] theory
$c_t = k_t$	Track stiffness (one-mass track model)
$c_{z,prim}$	Primary spring stiffness
$c_{z,sec}$	Secondary spring stiffness
d	Flat depth
d_{ref}	Contact reference damping in the wheel-rail contact
D	Nominal wheel diameter
D_{act}	Actual wheel diameter
f	A frequency
F_{prim}	Force which the primary suspension exerts on the unsprung mass
g	Gravitational constant, approximately 9.81 m/s²
k	Number of wheels
l	Flat length
l_{max}	Limit length for a tread defect from Table 7 of EN15313 [2]
m	Mass of the vehicle
m_{axle}	Axle load
m_r	Rail mass (two-mass track model)
m_b	Ballast and sleeper mass (two-mass track model)
m_t	Total track mass
m_w $m_{unsprung}$	Unsprung mass of the vehicle
n	Order of the polygonization
N	Normal force in the rail wheel contact
Q	Vertical component of the total wheel-rail-force in the wheel profile reference system, $Q = Q(t) = Q_{dyn}(t) + Q_{stat}$
Q_{dyn}	Vertical component of the total wheel-rail-force in the wheel profile reference system in a dynamic case, depending on the current time, $Q_{dyn} = fct(t)$
Q_{stat}	Vertical component of the total wheel-rail-force in the wheel profile reference system in a stationary case, constant, $Q_{stat} \neq fct(t)$
R	Nominal wheel radius
$R(\beta)$	Radius of a wheel at a given position on the circumference
R_0	Radius at the greatest flat spot depth
Δr	Circularity defect (Maximum radius difference between two points along the circumference of a wheel)

Symbol [unit]	Description
ΔR_0	Amplitude of the maximum radius deviation of a polygon, $\Delta R_0 = \Delta r/2$ for a polygon
$\Delta R_{0,max}$	Limit for the amplitude of the maximum radius deviation of a polygon from Table G.1 of EN15313 [2], $\Delta R_{0,max} = \Delta r_{max}/2$ for a polygon
$\Delta R(\beta)$	Radius deviation of a wheel from a perfect circle at a given position on the circumference, corresponds to $\Delta R(\beta) = R(\beta) - R$
s	Distance along the track centerline from a reference point
T	Total tangential force in the wheel-rail-contact (frictional force)
T_x	Component of the total tangential force in the wheel-rail-contact that points in the positive x-direction of the wheel profile reference marker (longitudinal)
T_y	Component of the total tangential force in the wheel-rail-contact that points in the positive y-direction of the wheel profile reference marker (lateral)
v	Vehicle speed
v_{crit}	Vehicle speed at which the axle box acceleration peaks reach their maximum, for both flats and polygons
v_{max}	Maximum operating vehicle speed
z	Vertical position of the axle box or center of the wheel
$\dot{z}$	Vertical velocity of the axle box or center of the wheel
$\ddot{z}$	Vertical acceleration of the axle box or center of the wheel
$\dot{z}_r$	Vertical velocity of the rail mass (two-mass track model)
$\dot{z}_{rel}$	Vertical relative velocity between a wheel and the corresponding rail
z_{max}	Maximum possible displacement of the wheel in the z-directon for a given circumference angle β
$\ddot{z}_{lim}$	Limit value for the axle box accelerations
$\ddot{z}_{max}$	Maximum absolute axle box acceleration for a given operating state
$\ddot{z}_{peak}$	Peak in the maximum absolute axle box accelerations $\ddot{z}_{max}$ for multiple vehicle speeds v
β	Circumferential angle of a wheel
μ	Coefficient of friction
υ	Slip in the wheel-rail contact
φ_0	Half the angle of a flat
ω	Angular velocity of the wheel

Term	Description
Circularity defect	Maximum radius difference between two points along the circumference
Continuous radius deviation	Any type of radius deviation that covers the whole wheel circumference

Term	Description
Crack	A fracture in or under the surface of the wheel profile
Discrete defect; discrete radius deviation	A type of radius deviation that does not cover more than 10% of the circumference
Cavity	More severe form of shelling, holes in the tread surface that develop from shelling or other defects, like flats
Flat (spot)	A discrete defect that results from the wheels sliding over the rail, often because of overbraking or a sudden drop in friction
Long local defect	A type of wheel defect that covers a large part of the circumference, usually more than 10%, but does not cover the whole circumference
Out-of-roundness	Any radius deviation of a wheel from a perfect circle, in some of the literature also a synonym for polygonization
P2-resonance	Resonance of the vehicle unsprung mass (i.e. wheelset and attachments) on the track stiffness, usually 50-100 Hz [3]
Polygonization	A type of wheel defect where the radius deviations follow a harmonic function of any order n around the circumference
Shelling	Material loss from the wheel profile, resulting from high stresses or fatigue
Spall	Superficial thermal cracks that can develop from tread braking
Stochastic radius deviation	A type wheel defect where the deviations follow a probability density function
Unroundness	Any radius deviation of a wheel from a perfect circle
Welding-on	A type of wheel defect where metal shavings embed themselves into the wheel profile as the wheel rolls over

Abbreviation	Description
CBM	Condition based maintenance
COG	Center of gravity
DAE	Differential-algebraic equation
DAS	Distributed acoustic sensing
FFT	Fast Fourier Transformation
GPRS	General Packet Radio Service
MBS	Multi-body simulation
TOR	Top of rail

1 Introduction

Modern rail vehicles are subject to many requirements, the most important are safety and availability. With service times of up to several decades, they need to be built in a way to withstand the harsh conditions out in the field. Current vehicles, especially passenger vehicles, usually possess two suspension stages. The first stage generally connects the unsprung wheelset with the bogie frame and acts mechanically as a filter for high-frequency movements of the unsprung mass, which should not be transferred to the bogie frame. The first stage is called primary suspension. The secondary suspension further decouples the movements of the wheels and the bogie frame from those of the car body, which contains the passengers or transported goods, in case the vehicle is not a locomotive. A full view of an example of a modern rail vehicle as well as a detailed depiction of a mechanical model of the most common two-stage suspension are shown in Figure 1-1.

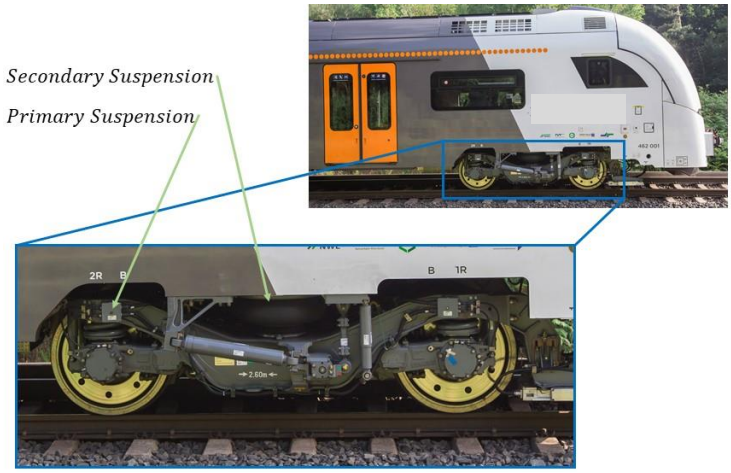

Figure 1-1 - Overview of a rail vehicle with a two-stage suspension. Source: *[4]*

Rail vehicles are track-bounded, which means they can only be operated on the proper infrastructure. One of their most important advantages compared to other forms of transport is their energy efficiency, which is a result of the wheels and the rail being made from steel, making the contact between the wheel and rail very stiff. The tracks deform under the high loads the vehicles exert on them, albeit the deformations are very small. They are orders of magnitude stiffer than the suspension stages of the vehicle. Tracks usually possess several layers of masses and stiffnesses themselves, similar to the vehicles. Most of the time, the rail is based on a row of sleepers, which themselves rest on an upper formation layer, sometimes with additional layers of other materials in between. The interface between the static track and the moving vehicle is formed by the wheel-rail contact. Both the wheel and the rail are usually made from steel and are, thus, very stiff, but not infinitely, so the 'contact points' between them are actually contact patches, as it can be seen in Figure 1-2. All forces acting between the vehicle and track are transferred via those contact patches, their size is in the order of magnitude of a medium sized coin. Considering that axle loads for commuter trains can reach up to around 20 t and their weight is supported by contact patches with a total size of about two coins, it is easy to imagine the kinds of stresses the wheel and rail material are subjected to. This is not even considering the additional loads introduced by traction forces, which are necessary for acceleration and braking.

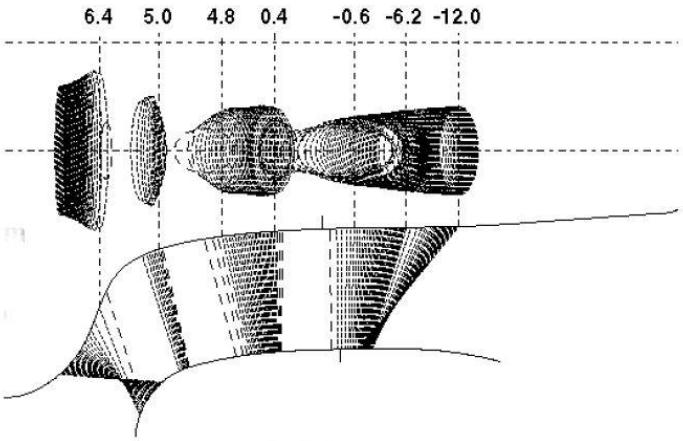

Figure 1-2 - Locations and shapes of contact patches for different contact positions on the wheel and rail profiles. Source: *[5].*

Resulting from the high loads acting on the wheel and rail in the contact patch, different wheel defects have been known to arise. Some of them, like flats, are a result of undesired conditions, e.g. wheel blocking. Others, like polygonization, are wear effects and form over a longer time period. Examples of such defects or their characteristics are shown in Figure 1-3 (a) and Figure 1-3 (b), respectively. What all wheel defects have in common is a change in the geometric shape of the wheel profile or the local wheel radius around parts or the whole wheel circumference, depending on the defect. This essentially creates a vertical excitation in the whole vehicle-track system, the wheel radius and profile deviations lead to additional relative movements between the wheel and rail resulting in additional dynamic forces.

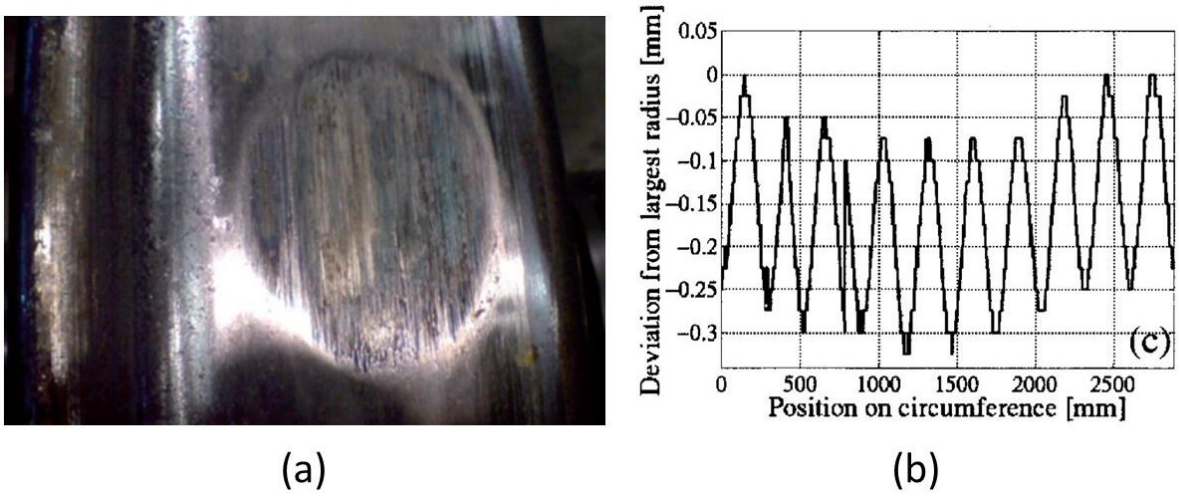

Figure 1-3 - (a) Example for a flat caused by a sliding wheel. Source: *[6]*. (b) Example for the radius deviations as a function of the circumference of polygonization. Source: *[7].*

They can become the cause of unsafe operational states, damages to components and failures of component mounts. To guarantee a safe operation of vehicles and minimize the damage caused by the additional loads induced by the wheel defects, they are limited by technical standards. The current limits from the standard EN15313:2016 [2] do not take into account the dynamic effects of wheel defects, but instead limit geometric properties of the defects themselves. The goal when establishing the current limits could be the definition of rules that can be checked easily, unambiguously and with the least possible effort and equipment, but still guarantee adequate operational safety. For this purpose, the standard EN15313:2016 distinguishes two kinds of wheel defects, namely tread defects and circularity defects. Tread

defects only cover a small part of the circumference, examples for this kind of defect are flats, spalls or cracks.

M (t)		*M* ≤ 18			18 < *M* ≤ 22.5				22.5 < *M*		
V (km/h)		*V* ≤ 160	160 < *V* ≤200	200<*V*	*V* ≤120	120 < *V* ≤160	160 < *V* ≤ 200	200 < *V*	*V* ≤ 100	100 < *V* ≤ 120	120 < *V*
D (mm)	1 000 < *d*	80	60	40	80	60	50	35	X	X	X
	840 < *d* ≤ 1 000	60	50	30	60	50	35	25	60	50	30
	630 < *d* ≤ 840	40	30	25	40	30	25	20	40	X	X
	550 < *d* ≤ 630	35	25	X	X	X	X	X	X	X	X
	d < 550	30	X	X	X	X	X	X	X	X	X
M: axle load in tonnes (t). *d*: actual wheel diameter X: reserved (no application known)											

Figure 1-4 - Table 7 from the current standard EN15313 limiting the lengths of tread defects. Source: *[2]*.

The assessment criterion for tread defects was defined as the greatest visible dimension of the defect, and limit values for this dimension were taken from experience. Figure 1-4 shows the limit values that are in place currently, prescribed in the standard EN15313. In the same standard, limit values for circularity defects Δr are also proposed in the informative annex, they can be seen in Figure 1-5. Circularity defects Δr are defined in Figure 1-6, they are essentially the difference between the largest and smallest radius of a wheel and therefore, limiting them also covers wheel defects that cover a large part of the wheel circumference.

Table G.1 — Permissible circularity defects

Wheel diameter d (mm) Speed range v (km/h)	Permissible circularity defects (Δr) (mm)
d> 840	
• $v_{max} \leq 60$	1,5
• 60 km/h < $v_{max} \leq 160$	1,0
• 160 km/h < $v_{max} \leq 200$	0,7
• $v_{max} > 200$	0,5
380 < d ≤ 840	
• $v_{max} \leq 200$	0,7
• $v_{max} > 200$	0,5
d ≤ 380	0,3

Figure 1-5 - Table G.1 from the current standard EN15313 limiting circularity defects (informative annex). Source: *[2]*.

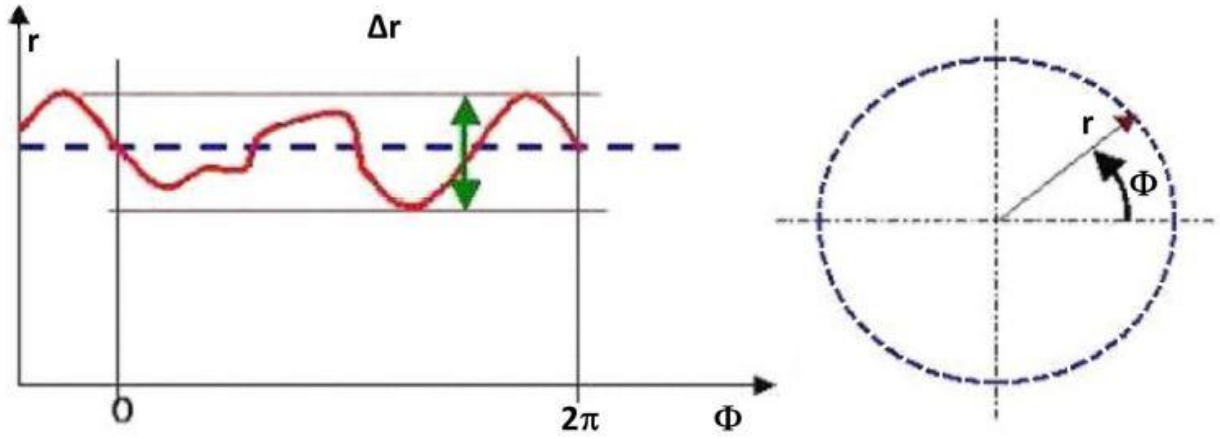

Figure 1-6 - Definition of a circularity defect Δr from the current standard EN15313. Source: *[2]*.

1.1 Motivations and Goals

All limit values have the aim of guaranteeing a safe operation of the vehicle. An unsafe state is not caused by a defect directly, but by the dynamic response it evokes. If the assumption is that limit values for geometrical defect sizes indirectly try to limit loads on the vehicle-track system, they assume a correlation between the geometrical sizes and the resulting loads. It is not clear whether this is the case. With the rise of on-board computing power and widespread sensor technology, assessing the dynamic response of a wheelset is becoming a feasible alternative to checking the limit values by hand. The current state-of-the-art method involves bringing the vehicle to a depot, where every wheel needs to be inspected by a technician manually, which is a very time-consuming and expensive process. It is also only possible to inspect the wheels of a vehicle between the prescribed service intervals, making it impossible to detect a defect right after it was formed. The greatest drawback of the current assessment method is that it is not clear whether mechanical loads can even be limited by limiting the sizes and radius deviations of wheel defects. This is only the case if a direct, monotonic correlation between the size or radius deviation and the resulting dynamic effect exists. Therefore, the main goal of this thesis is to question the current limits and check for a correlation between them and the dynamic effects that result from them. If a correlation can be found, it could be used to define an additional method to inspect out-of-round wheels using acceleration measurements, and still fulfill the current limits as stated in the standard EN15313.

There is a possibility that such a correlation does not exist. If this is the case, the current limit values in EN15313 do not implicitly limit the dynamic effects resulting from out-of-round wheels, and equivalent acceleration limits cannot be established because of the missing correlation. This would also mean that defects exist which are not covered by the current standard yet produce high loads and thus incur more maintenance costs. Using a dynamic-based assessment approach without considering the geometric properties, such defects could be easily identified. Defects that are covered and banned by the current standard, yet only have a small dynamic impact, could be tolerated, increasing the wheelset service life. From the standpoint of these improvement potentials, the ideal assessment method for wheel defects includes a continuous monitoring of the dynamic effects induced by them.

The possibility of checking the condition of the wheels using a track-side system also exists, and it is explicitly stated in EN15313. However, a fully automatic process is not permitted by the standard. In the case that a track-side system, no matter its working principle, detects a faulty wheelset, the wheelset needs to be inspected by a technical expert at a vehicle maintenance facility. The damage must be assessed according to the length limit values [2]. Another goal of this thesis is to assess whether this rule from the standard is often being made use of and whether such track-side systems are widely spread or even available in the railway industry.

1.2 Tasks

Specific tasks that needed to be performed to fulfill the goals were defined before the beginning of the present thesis, they are explained in this section.

The first task is to investigate general effects of out-of-round wheels on dynamic quantities of the vehicle-track system to better understand which of them are even affected by unround wheels. The subsequent task is to perform a market analysis to find out if any trackside or train-bound automatic vehicle inspection systems already use these effects to assess wheel defects and if so, which dynamic quantities are used for the assessment.

Furthermore, the dynamic effects investigated as the next task are accelerations of the axle box, which are easily measurable on vehicles. Advantages of onboard measurement systems compared to measurements from trackside systems is the existence of continuous measurements spanning all possible operational states, as well as the possibility to detect damages to the wheelset immediately after they occur. Trackside system, on the other hand, have the advantage that only a few of them are required to inspect the whole fleet, if they are placed properly within the rail network.

In the standard EN15313, tread defects essentially have the same definition as do discrete radius deviations in the current thesis, which is described in more detail in chapter 1.3.1. The maximum value for the length of the largest tread defect on the wheel tread is limited. The limit values depend on the maximum vehicle speed v_{max}, the axle load m_{axle} and the actual wheel diameter D_{act} of the respective wheel, as can be seen in Table 7 from EN15313, which is depicted in Figure 1-4. To check whether the wheels fulfill the standard using only an acceleration-based method, a correlation between the dynamic effects and the lengths of discrete radius deviations is required. However, the next task is to check whether such a correlation even exists. Even if no direct correlation exists, the subsequent task is an analysis about whether the length limits were chosen in a senseful way. Since tread defects have different shapes and therefore most likely induce different dynamic responses, only flats will be investigated within the scope of this thesis.

With measurements from enough vehicles with flats of different sizes, a correlation could be found empirically. However, as waiting for flats of different sizes to occur by chance on different vehicles to obtain axle box acceleration measurements is too time consuming, an MBS model shall be built and used to allow a relatively quick investigation of a wide range of parameters. Since measurements are available from one vehicle with one flat, the model shall be calibrated with the measured data so it can be trusted to produce accurate results for other parameter sets.

The standard EN15313 also covers circularity defects, albeit only in an informative annex. The circularity defect Δr is defined as the maximum difference between two radii around the whole wheel circumference, as shown in Figure 1-6, where it is represented by the green arrow. It is limited to a certain value, again depending on a few vehicle parameters. Limiting the maximum allowable circularity defect also implicitly limits flats that have a certain depth, although the length limit for tread defects is usually exceeded by flats and other discrete defects far before the circularity defect limit. The circularity defect limits, as seen in Table G.1 of EN15313 (see *Figure 1-5*), most commonly apply to continuous radius deviations around the complete circumference, like polygonization, which will be the subject of investigation in the scope of this thesis. The tasks are to check if a correlation between the circularity defect Δr of a polygonized wheel and the resulting axle box acceleration can be found, as well as to investigate the influence of other parameters, namely the polygonization order n and other

vehicle and track parameters. The main task is to assess whether limiting only the circularity defect, as currently done in EN15313, is a senseful way of limiting the dynamic responses of the unroundness. Because collecting enough measurements from vehicle and tracks with a wide parameter range is almost impossible, an MBS model shall be built and used to complete the given tasks, since an easy and quick investigation with a wide range of parameters can be performed.

1.3 Definitions

Even though rail systems exist all over the world, their dependency on the infrastructure and the lack of standardization, especially in the beginnings of this industry almost 200 years ago, have led to the rise of different independent terminologies. For the reader to get a clear and concise understanding of this work and see which defects are limited by EN15313, some terms that may have differing definitions throughout the existing literature are defined in this section.

1.3.1 Kinds of Out-Of-Roundness

An out-of-roundness or unroundness is a general term for a wheel, which does not have the same radius at each point along the circumference. It can be any kind of radius deviation and cover any part of the circumference. The most general distinction that can be made is that between radius deviations that only cover a part or the whole circumference. Radius deviations that persist along the whole circumference of a wheel will also be called continuous radius deviations.

Polygonization is a special kind of continuous radius deviation. This kind of radius deviation behaves like a sine wave of order n around the circumference, which means that it possesses n peaks and n throughs in the radius along the circumference. Another kind of continuous radius deviation is a stochastic radius deviation, for which no pattern in the radius deviations along the circumference is found. The circularity defect limits mentioned in chapter 1.2 mostly apply to continuous radius deviations. In the standard EN15313, polygonization and stochastic radius deviations are defined just like in the current thesis [2].

Radius deviations, which only cover a part of the wheel are divided into two subgroups. The first subgroup consists of radius deviations, which cover only a small part of the nominal wheel circumference and will be called discrete defects. The second subgroup consists of radius deviations, which cover a substantial part of the nominal wheel circumference, but not all of it, and are called long local defects, as defined in [8].

Examples for the most important discrete defects, also called discrete radius deviations, are flats, cracks, spalls, shelling, cavities and metal build-ups, the definitions of these defects are taken directly from EN15313 [2]. Flats or flat spots are the result of a blocked wheel sliding over the rail and usually only remove material from the wheel by abrasion. In some cases, the material from the wheel is not only worn off, but melts as a result of the extreme temperatures that arise from the sliding process. Some of the melt deposits right behind the flat spot, effectively creating a radius deficit where the flat spot is located and a radius surplus right behind it.

Cracks are fractures within the wheel material, no material is lost during their creation. If a wheel is subject to high thermal loading, which can occur as a result of tread braking, spalling can develop, which consists of superficial thermal cracks. Shelling is defined as material separation from the wheel tread due to high stresses or material fatigue. Cavities are essentially holes within the tread surface, resulting either from shelling that has already occurred, or other prior damages to the wheel tread.

When a wheel is subjected to high thermal loads, metal from either the brake block or the rail can accumulate on the wheel, which is called a metal build-up, like the one that can form on the rear edge of a flat, as explained earlier.

Another type of discrete radius deviation is known to exist, which is called a long local defect. Long local defects are usually 0.3-0.5m long and can be up to 6mm deep. Their formation is described in [8].

1.3.2 Coordinate Systems and the Wheel-Rail-Contact

The convention for a local coordinate system of a rail vehicle is an x-axis pointing in the positive driving direction of the vehicle, a y-axis pointing laterally to the right of the positive driving direction, and a z-axis pointing downwards. The positions of the vehicle and all parts of the vehicle are described relative to the track, using the s-coordinate to describe the position along the track centerline, the y-coordinate to describe movements in lateral direction with respect to the track plane and the track centerline, the z-cordinate to describe vertical movements with respect to the track plane, and the φ-, ψ, and γ-coordinates to describe the rotational angles for roll, yaw and pitch, respectively. The track coordinate system is shown in Figure 1-7 (a).

In a wheel-rail-contact, two kinds of forces are distinguished. The first kind are forces acting within the normal plane of a contact, which basically slices the wheel and track so that their respective profiles become visible, as can be seen in Figure 1-7 (b).

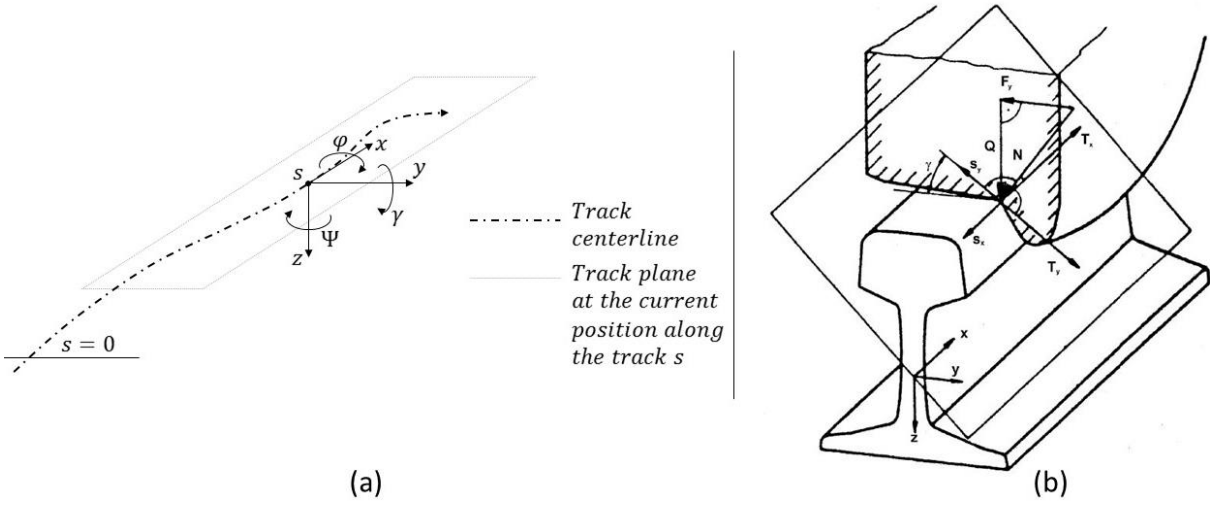

Figure 1-7 - (a) Rail vehicle coordinate system. (b) Forces acting within a wheel-rail-contact, normal and tangential plane. Source: *[5]*.

Assuming the contact is frictionless and the vehicle stationary, the magnitude of the normal force N can be simply calculated from the weight force G that the vehicle exerts on the wheel-

rail-contact and the slope γ of the wheel and rail profiles in the contact point. Therefore, those forces are also called constraining forces. The so-called Q-force is defined as the component of the normal force acting in the vertical direction of the rail coordinate system, parallel to the z-axis. An overview of the whole vehicle with the Q-forces resulting from the weight force is depicted in Figure 1-8. The second kind of forces that exist in a wheel-rail-contact are frictional forces T, which only occur when the relative speed v_{ref} between the rail and the wheel is not zero in the contact point. In other words, they only occur if a certain creepage ν is present in the wheel-rail-contact. Since the normal forces N are mostly affected by unround wheels, the tangential forces T are not relevant to this thesis and a further description is therefore omitted. For more information about the wheel-rail contact, refer to [9]. Since the Q-force in the multibody-simulation software used within this thesis, *SIMPACK* (refer to chapter 5.1 for more details), is defined as the vertical component of the resultant of both the normal and tangential forces expressed in the wheel profile reference system, this is also used as the definition of the Q-force for this thesis [10], unless otherwise specified. It differs from the usual definition shown in Figure 1-7, where the Q-force is strictly a part of the normal force and not a part of the tangential forces.

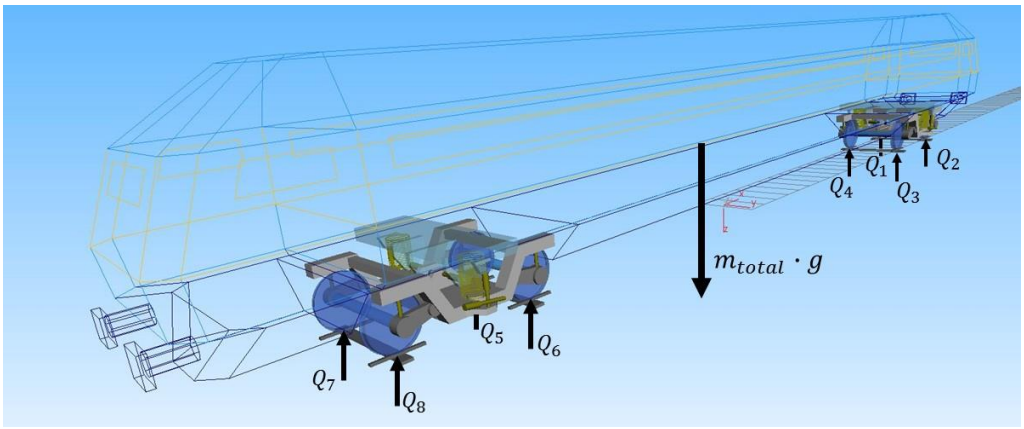

Figure 1-8 - Vehicle Overview. Q-forces resulting from the weight force. Created by the author with *SIMPACK*.

Additionally, all calculations in this thesis are performed with running bogies on a straight track, with little or no creepage and, thus, small or nonexistent tangential forces. The contact patch is located on the wheel tread on a straight track, which has a small slope γ, making the Q-force almost identical to the normal force N, yet not exactly the same, resulting in a negligible error.

1.4 Existing Research

Numerous papers have been published on the formation and dynamic effects of out-of-round wheels, most of them concentrating on their effect on the wheel-rail-force, albeit with different results. Almost all numerical models found in the literature use the *Hertzian* theory for the normal force calculation. The following summaries are not complete, only the most relevant aspects for this thesis are presented. For reference, refer to the respective sources.

An extensive amount of research on both the formation and effects of unround wheels has been performed by *A. Johansson* in his PhD thesis [8], which consists of an introduction and six appended papers.

Within paper A [11] of this work, an extensive literature survey has been carried out, giving an overview over the classification, detection and formation of different types of radius deviations, as well as existing wheel removal criteria. The different types of out-of-roundness are classified in a similar manner as in the present thesis. Criteria for wheel removal for different railway systems are discussed. Unlike the European standard EN15313, that is based solely on a visual inspection of the wheel and limits lengths of tread defects, an additional criterion exists in North America that limits the peak impact force caused by a wheel flat to 445 kN. A length limit exists in parallel, which limits the length of a flat to 2.5 in, which corresponds to 63.5 mm and is the same order of magnitude as the limits in the European standard. Swedish national wheel removal criteria are discussed, which are also based on the length of the tread defect. A general approach to simulate the formation of polygonization is laid out.

Paper B [7] deals mostly with the dynamic wheel-rail-forces that any type of out-of-round wheel induces. It is laid out that some types of defects exist that are not covered very well by the length limit criterion because they are not visible by a simple visual inspection, yet produce impact forces that can be higher than that of some better visible defects, like flats or spalls. One of these defects is called long local defect. Additionally, the paper suggests that the depth of a flat has a greater influence on the impact force that it produces than its length. A method utilizing axle bearing vibration (i.e. acceleration) and temperature measurements to detect out-of-round wheels is mentioned briefly. The numerical model used for simulations is presented. Measured radius deviations of a wheel with a flat, a long local defect and a polygonised wheel are used as input for the simulation. Field tests were carried out with the vehicle the radius deviations had been measured on, during which the wheel-rail-force was determined.

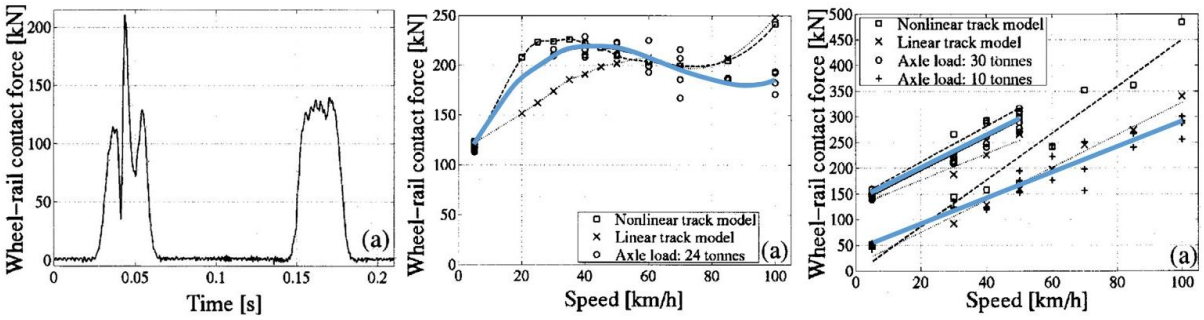

Figure 1-9 - (a) Wheel-rail contact force measured by a single strain gauge while a wheel with a 100 mm flat passed the measuring site. Source: *[7]*. (b) Wheel-rail contact force maxima for a 100 mm flat for different vehicle speeds, measurements and calculations. Source: *[7]*. (c) Wheel-rail contact force maxima for a 0.5 m long, 5.5 mm deep long local defect over a vehicle speed range, measurements and calculations. Source: *[7]*.

A characteristic response in the wheel-rail force was found for flats, decreasing first, as the flat enters the contact patch and the radius deviation becomes larger, with a shark peak when the radius deviation starts becoming smaller and contact is reestablished, a depiction of which is shown in Figure 1-9 (a). Wheel-Rail contact force maxima for various vehicle speeds are presented for flats and long local defects, as shown in Figure 1-9 (b) and (c). The trendlines that were calculated using measurements are marked blue. For flats, a peak in the maximum forces is reported at a certain vehicle speed. After the peak, the maximum force begins to decrease,

with another increase at higher speeds. For the long local defect, a monotonic increase of the maximum wheel-rail force with the vehicle speed can be observed. The influence of the flat length was examined, by simulating a flat of different lengths, always with 1 mm depth. The maximum of the contact force Q is shifted to higher speeds for longer flats, but the length had almost no impact on the maximum force value. This value was better influenced by changing the depth of the flat. For polygons, simulations and measurements are performed as well. Both measurements and simulations with linear and state-dependent track models show a slight peak of the wheel-rail contact force at a certain vehicle speed, owing to the P2-resonance of the system, which is explained in the corresponding chapter 5.2, and shown in Figure 4-1.

A lot of research has been performed on the formation of polygonization on wheels. *Wu* et al. have investigated the formation of polygonization on high speed trains in [12]. They concluded that a resonance in the coupled train-track system is excited by the excitation of a bogie frame resonance frequency through normal track irregularities and initial wheel defects. Like the study of *Johansson* [7], this shows the importance of train-track interactions for the formation and effects of out-of-round wheels, even though many other effects can lead to polygonization as well.

L. Baeza et al. investigated the error resulting from the use of *Hertzian* [1] contact models for modeling flats in [13]. For typical railway wheels, the assumptions for the validity the *Hertzian* contact theory are fulfilled to a large degree. For wheels with flats, this is not the case, especially for flats with sharp, non-rounded edges. A non-*Hertzian* contact model was established, differences of up to around 18 % in the contact force for rounded flats could be observed, albeit only for a certain speed range. The difference only occurs in the peak of the contact force Q, outside of the impact, the simulation results almost do not differ at all.

R. Dukkipati and *R. Dong* did some research work on the dynamic effects and impact loads due to dipped joints, wheel flats and shells in [14] and [15]. In [15], an FE model for simulating flats has been validated. Experimental data from [16], which shows a peak in the maximum wheel-rail force at a certain vehicle speed for flats, was used to validate the model. After this speed is exceeded, the magnitude of the peaks in the Q-force decreases. The model shows the same characteristic as the experimental data with increasing vehicle speed. The impact forces show a monotonic increase with the axle load. The unsprung mass had almost no effect on the impact forces Q, neither did the primary stiffness. This is explained by the smaller impact velocities of the wheelset as the unsprung mass is increased. The impact loads rise due to an increase in both rail pad and ballast stiffness. The flat length with a constant flat depth had an effect similar to the vehicle speed, with a peak at a certain flat length and a decrease for longer flats.

A peak in the maximum wheel-rail forces Q at a certain vehicle speed, with a decline when this speed is further increased, has also been reported by *R. Zunsong* for flats in [17]. This tendency is not confirmed by *R. Uzzal* et al. in [18], where the vertical acceleration $\ddot{z}$ of a wheel with a flat shows a monotonic increase with vehicle speed v for most flat depths d, although for some flat depths, a slight peak can be distinguished, albeit not as clear as in some of the references mentioned before.

Analytical calculations have been performed by *M. Steenbergen* to determine the maximum wheel-rail contact force Q produced by a flat in [19] and [20]. Ideal, fresh flats and worn flats

have been studied and an equation for the maximum impact force has been derived. Because of the singularity resulting from the flat part of a flat, a curvature has been applied to the flat part to yield an analytical solution. This introduces another unknown quantity, which makes the analytical calculation of loads resulting from flats difficult.

To conclude, a lot of research has already been conducted on the dynamic effects of wheel defects and their formation. Many of the models used in the citation, but also other studies, are not validated with measurement results collected by the authors themselves but instead based on measurement results from a few other studies. If the models are validated, this is often only done for one particular vehicle speed, with no validation over the whole vehicle speed range. Most importantly, most studies in this area try to determine the impact force Q resulting from a given wheel defect, concentrating on track-side inspection systems that measure the Q-force. In the current thesis, the approach is to try to find the correlation between the axle box acceleration $\ddot{z}$ and the size of the wheel defect, to make the use of a continuous, train-borne unroundness detection system in accordance with the standard possible. Finding out whether such a correlation exists would enable the 'conversion' of the current size-based limits to 'acceleration-based limits' or, if no such correlation exists, the proposal of new, sensible acceleration limits.

2 Investigated Wheel Defects and their Effects

In this section, the causes and effects of the investigated types of unroundness are discussed. The current wheelset maintenance standard EN15313 covers many of the possible defects, but since this thesis focuses on flats and polygonization, only those are discussed in more detail. For other defects, see EN15313 [2] for reference. First, however, general effects of out-of-round wheels are discussed. Automatic systems utilizing measurements of the explained effects to detect and assess out-of-round wheels are presented in the following chapter 3, building on the explanations provided in the current chapter.

2.1 General Effects of Out-Of-Round Wheels

A perfectly round wheel rolling on a perfectly flat track theoretically does not move in the vertical direction. It leads to a dynamic Q-force Q_{dyn} of zero and to a Q-force of the same magnitude as the static Q-force Q_{stat}, which is the Q-force when the vehicle is not in motion at all, meaning that $Q(t) = Q_{stat}$. It can be calculated using Equation 2-1, where k is the number of wheels, neglecting any slight shifts of the COG with respect to the geometric center of the vehicle.

$$Q_{stat} \cong \frac{G}{k} = \frac{m \cdot g}{k} \qquad \text{Equation 2-1}$$

In this equation, m corresponds to the total mass of the vehicle and g is the gravitational constant. In such a case, the wheel COG does not move in the z-direction, and there is no acceleration $\ddot{z}$ in the z-direction. This situation is depicted in Figure 2-1 (a).

In case the wheel is not perfectly round, still considering a perfectly flat track, it can be found by kinematic analysis alone that the position z of the wheel in the vertical direction changes as it moves along the track, since the radius of the wheel at the contact patch changes with the rotation angle (neglecting the possibility of loss of contact). If the wheels and the whole vehicle are at rest in the z-direction at first, a change in position of a wheel can only be achieved if the forces acting on in that direction are no longer in equilibrium. Assuming that the mass of the vehicle and, thus, the force exerted on the wheelset by the primary suspension F_{prim} remain the same[1] during the measurement, it is $Q(t)$ that must have changed in magnitude, as shown in Figure 2-1 (b). Since the static Q-force Q_{stat} is constant, a dynamic part in the total Q-force must have arisen, meaning Q_{dyn} is no longer zero. If loss of contact between the wheel and rail occurs, the impact force when the contact is re-established also differs from the static Q-force Q_{stat}. When the downwardly moving wheelset hits the rail, it is accelerated upwards so its downwards trajectory comes to a sudden stop. The force causing the upward acceleration is the dynamic part of the total Q-force Q_{dyn}, which needs to be larger than zero for an upward acceleration to occur. This reasoning shows that the dynamic part of the total Q-force Q_{dyn} of each wheel depends on its out-of-roundness and can be used to assess it, barring too much influence from factors other than the radius deviation of the wheel from a perfect circle, like imperfections of the rail or the track. The same reasoning also shows that the vertical

[1] Typical primary stiffnesses are around 1 kN/mm per wheel. Typical axle loads are around 20 t. This leads to a change in F_{prim} of around 0.1 % if the wheelset moves 0.2 mm vertically, which corresponds to the depth of a flat of length l = 30 mm, which is negligible considering the change in the force exerted by the primary suspension.

acceleration of the wheelset $\ddot{z}$ is directly related to the vertical forces acting on the wheel and can also be used to assess the unroundness.

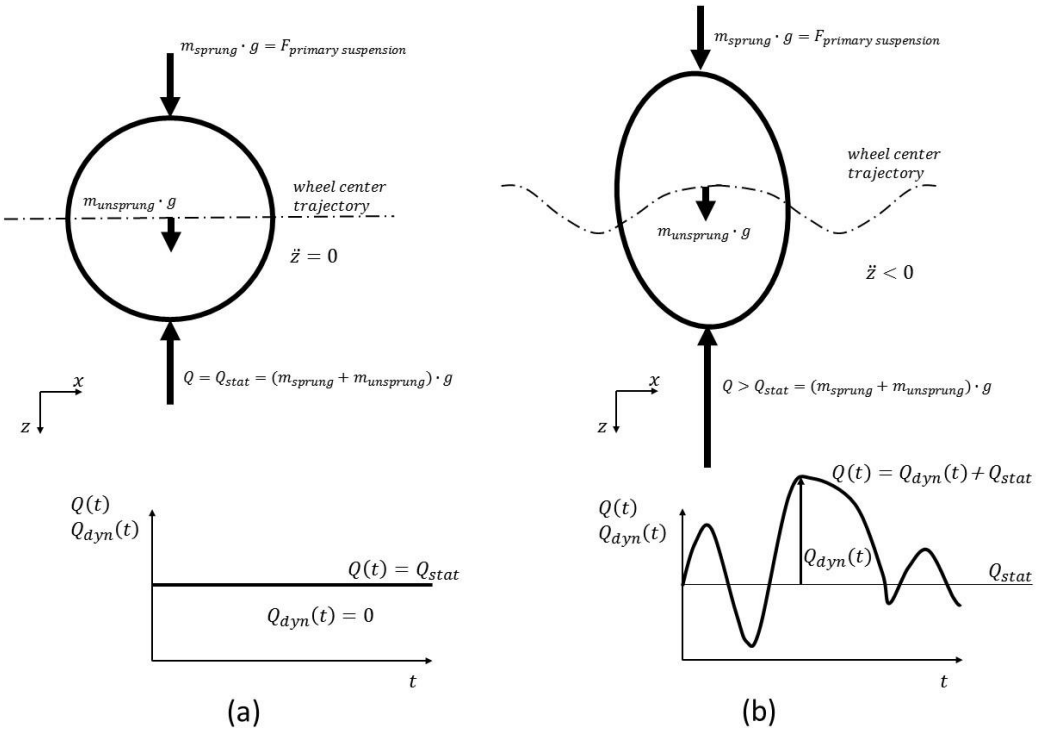

Figure 2-1 - (a) Dynamic situation of a perfectly round wheel. (b) Dynamic situation of an out-of-round wheel.

So far, the flexibility of the wheels and rails has not been mentioned. Since they are both not infinitely stiff, changing Q-forces induce changing deflections and vibrations of parts of the vehicle and track. Especially discrete defects, like flats and cavities, produce sharp impacts, which excite a large range of frequencies, among them audible frequencies. Those impacts induce structural deformations, which are partly radiated into the air. Depending on the size and shape of the unroundness and some other parameters, the structure-borne and air-borne noise, produced by the out-of-round wheel, can reach different noise levels. The formation of sound waves as a result of structural deformations of the rails is shown in Figure 2-2. Depending on the kind of out-of-round and the sound characteristics, the sound level may be measured and used to detect and assess out-of-round wheels.

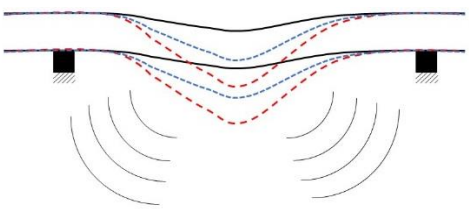

Figure 2-2 - Sound radiation from a bending rail subjected to changing Q-forces.

A consequence of the changing total Q-force is that the rail is subject to changing deflection, depending on the magnitude of the Q-force currently acting on it, which is shown in Figure 2-3 (a) and (b). As the Q-force acting on a rail changes because the wheel is not perfectly round, the deflection of the rail changes. In order to accommodate the new deflection, the rail is accelerated to reach its new position. Both the deflection and acceleration of the rail are effects that depend on the characteristics of the out-of-round wheel and can be used to detect and assess it.

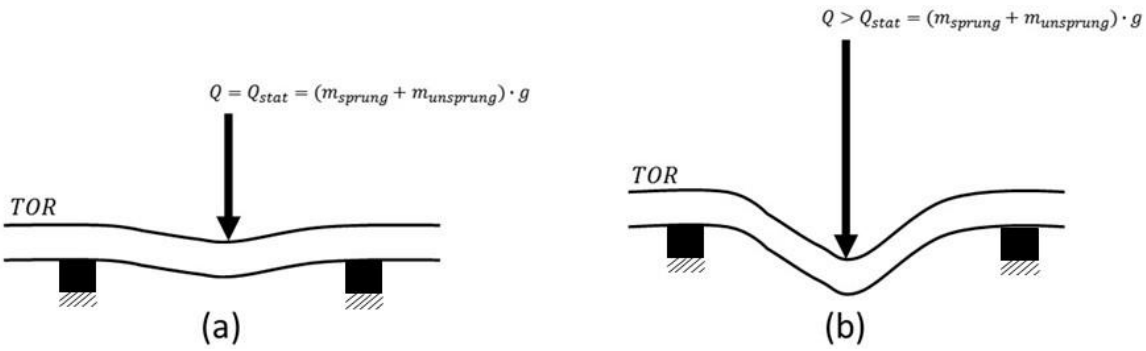

Figure 2-3 - (a) Small deflection of a rail under a static Q-force with $Q = Q_{stat}$. (b) Large deflection of a rail under a total Q-force that is larger in magnitude than Q_{stat}.

2.2 Polygonization

Polygonization is a special case of a stochastic radius deviation. The radius deviation is a function of the wheel circumference angle $\Delta R(\beta)$ of a polygonized wheel and contains almost only one frequency or wavelength. Many different mechanisms for the development of polygonization exist. They have been studied thoroughly in the existing literature, but many of them are not yet fully understood. Most of the time, the interaction of multiple effects leads to the formation of a polygonized wheel. A large study was performed in [21], showing some of the possible causes of polygonized wheels. Some causes have their underlying effects in the manufacturing of the wheels and wheelsets. It is reported that initial polygons of first or third order have been found on newly produced wheels, resulting from a dirtied clamping cone or the use of a three-jaw chuck, respectively. Other causes can be increased wear in certain spots on the wheel tread because of lateral movements of the contact patch, if certain eigenmodes of the wheel or wheelset are excited. Most of the time, those are bending eigenmodes of the wheelset or twisting eigenmodes of the wheel disc. Other possible causes listed are inhomogeneities in the wheel material, as well as inhomogeneous heating or cooling during heat treatments of the wheel. Even small flats have been identified as causes for polygonization in the study [21]. Polygonized wheels usually cannot be identified with the naked eye, a roundness measurement is of necessary. Radius deviation amplitudes ΔR_0 of polygons are in the order of magnitude from a few micrometers, up to a millimeter. The result of a roundness measurement can be looked up in Figure 1-3 (b). In other studies, it was shown that the formation of polygonized wheels can be the result of the excitation of track and bogie frame eigenmodes, see [12] for reference. Other effects not specifically mentioned in this thesis which lead to the formation of polygonized wheels may exist.

Polygonization, like all other wheel defects, increases the dynamic loads on vehicles and tracks since it induces vertical relative motions. Depending on the order of the polygonization, the change of the wheel radius in the contact patch can lead to the excitation of certain eigenfrequencies. Those can be eigenfrequencies of the train-track system or of the vehicle itself. They can lead to damage of components of both the track and the vehicle. Even the lift-off of wheels has been observed as a result of polygonization. Other effects that occur are increased rolling noise and further development of already existing polygons, worsening the effects.

2.3 Flats

Flats are discrete wheel defects and cover only a relatively small part of the wheel circumference. They are created by wheel blocking and subsequent sliding. The wheel blocking can be the result of a sudden drop of the friction coefficient in the wheel-rail contact or overbraking, meaning that the braking force applied by the brake control is larger than the maximum force that can be transferred by the wheel-rail contact. Depending on the frictional conditions and sliding duration, flats can reach different sizes. For regular wheelsets, both wheels are rigidly connected by the axle, meaning the sliding should happen on both wheels simultaneously. However, if the adhesion conditions are different for the two wheels, a flat may only form on one wheel, or the flats may be of different sizes. This could be the result of one rail being wet, covered in leaves or other materials that have an influence on the frictional properties. Usually, flats have pronounced edges right after their formation, which become rounded as the wheel rolls over the flat repeatedly. In some cases, flats have even been found to be the cause of other types of unroundness [21]. Under certain conditions, the temperature in the contact point can become so high during the sliding process that molten material starts to deposit at the rear edge of the flat, an example for which is shown in Figure 2-4.

Figure 2-4 - Wheel flat with a subsequent material deposit. Source: *[22]*.

As stated before in chapter 1.1, flats have negative effects on both the vehicle and track. They usually produce sharp Q-force and vertical wheelset and rail acceleration peaks. In rare cases, this can lead to cracks in the wheel or rail material, for example, in very cold conditions. Most of the time, however, the effects are not as detrimental, but can still lead to dangerous or uncomfortable situations. Flats can produce a very loud and annoying noise every time they hit the rail, which is not desirable for passenger vehicles. Also, because of the high acceleration and force peaks induced, parts that are mounted to the axle box, like earthing contacts, may be damaged.

3 Commercially Available Systems

There exist many commercially available systems for the detection of out-of-round wheels, which is usually not their sole purpose. Most systems, which are available on the market, are track-side systems, which means that vehicles must pass a certain point or points within the railway network where one of these systems is installed to be inspected. As mentioned in chapter 1.1, track-side systems may not be operated without human intervention in case pre-set limit values are exceeded, which is prescribed by EN15313.

Some systems are installed directly on vehicles and allow a continuous inspection. In the case of train-borne systems, at least one system is needed for each vehicle or car, unlike track-side systems, where in theory only one is required to inspect a whole fleet – given that all vehicles pass the inspection site regularly. The fact that a smaller number of trackside systems than train-borne systems is needed to inspect a whole fleet constitutes one of the advantages of trackside systems. A downside resulting from this is that trackside systems only provide short and sometimes irregular measurements, meaning that a faulty wheelset may not be detected by chance. The working principles that are used by these systems to detect out-of-round wheels are numerous. The systems presented in this thesis will be grouped into one out of four categories, depending on the measurement variable they use to assess the magnitude or severity of the wheel unroundness. The four categories of the presented wheelset inspection systems are as follows, the exact working principles are explained in the corresponding chapters:

- Geometry (chapter 3.1)
- Force (chapter 3.2)
- Acceleration (chapter 3.3)
- Sound (chapter 3.4)

The general detection and assessment process for out-of-round wheels is shown in Figure 3-1. How each variable is measured can differ between the systems within each category and does not affect the category a system is assigned to. In this thesis, the relevant criterion for the grouping is the usage of a variable for the severity or size assessment of the unroundness. A relation between the size or severity of the unroundness and the measured variable is used to deduce the size from the measured variable. In Figure 3-1, this part of the process is shown in the topmost, right block.

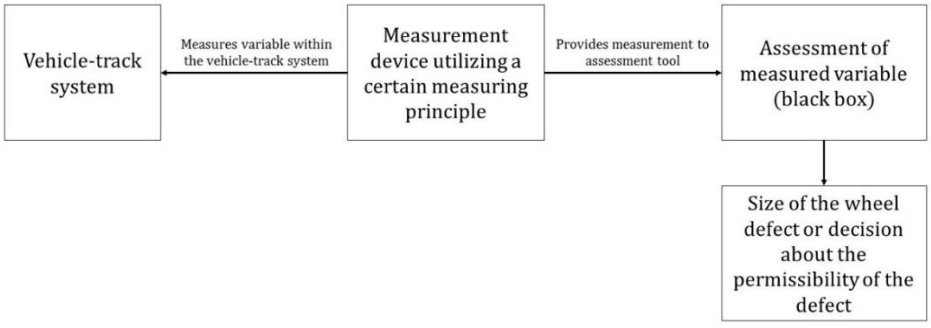

Figure 3-1 - General unroundness assessment process, applicable to each of the systems presented, using any measurement variable.

Each variable describes a physical quantity in general terms. This means that the measurement variable "Force" does not automatically refer to a special force, like the wheel-rail-force, but to a measured quantity with the physical unit of a force is that used for the evaluation of the out-of-roundness. The same applies to the measurement variables "Acceleration", "Geometry" and "Sound", which constitute any quantity measured within the vehicle-track-system with the physical unit acceleration, length and sound pressure, respectively. Table 1 shows an overview of the different systems, including the kinds of unroundness that can be detected using each system, as well as the measurement variable used to assess the severity of the unroundness. For the definitions of the errors in the "Detectable errors"-column of Table 1, refer to chapter 1.3.1.

Table 1 - Overview of commercially available unroundness detection systems.

Name	Company	Measurement Variable	Detectable errors
ARGUS II	Hegenscheidt MFD GmbH [23]	geometry	flats, continuous radius deviations
WTMS	MRX [24]	geometry	flats, continuous radius deviations, spalls
Calipri	NEXTSENSE GmbH [25]	geometry	flats, continuous radius deviations, spalls
TreadView	BeenaVision [26]	geometry	flats, continuous radius deviations
VEMS - A.V.I.S.	Bombardier [27], IBM [28], MRX [24]	geometry	flats
W-Inspect	MERMEC [29]	geometry	flats, spalls
Geopar-VKPSystem	RIFTEK Ltd. [30]	geometry	discrete defects, continuous radius deviations
ARGOS WTMS	Höttinger Baldwin Messtechnik GmbH [31]	force	flats, polygonization
WDMS	MRX [24]	force	flats
DafuR	DB Systemtechnik GmbH [32]	force	flats, polygonization, build-ups, other tread surface errors
MULTIRAIL Wheel Scan	Schenck Process Europe GmbH [33]	force	flats, continuous radius deviations
ATLAS FO	Voestalpine SIGNALING Siershahn GmbH [34]	force	flats, polygonization, spalls, build-ups
LASCA	INNOtec Systems GmbH [35]	force	flats, continuous radius deviations, spalls
GOTCHA	Lloyd's Register Rail [36]	force	not specifically listed
ARGOS	Höttinger Baldwin Messtechnik GmbH [31]; ÖBB [37]	acceleration	flats, continuous radius deviations

Name	Company	Measurement Variable	Detectable errors
Perpetuum	Perpetuum Ltd. [38]	acceleration	not specifically listed
Erfassung von Laufflächenschäden an Eisenbahnrädern	PCB Synotech GmbH [39]	acceleration	polygonization, discrete defects
Insight Rail	SKF [40]	acceleration	not specifically listed
WORM	i-moss NV [41]	acceleration	flats, polygonization, continuous radius deviations
Detection Of Flat Spots On Wheel Profile	RAFAMET S.A. [42]	acceleration	flats
Fahrwerksdiagnose und -überwachung	Siemens Mobility GmbH [43]	acceleration	flats, continuous radius deviations
DSR	Talgo [44]	sound	not specifically listed
WMS	Mueller-BBM GmbH [45]	sound	flats, polygonization
Versteckte Flachstellen- und Polygonermittlung	Deutzer Technische Kohle GmbH [46]	sound	flats, polygonization
FTS	Frauscher Sensortechnik GmbH [47]	sound	flats
RailBAM	Wabtec Corp. [48]	sound	not specified

3.1 Wheel Geometry

This group of systems does not measure any dynamic or other effect of the unroundness of a wheel, but instead determines the geometry of the wheel profile around the circumference directly. Although this method may appear very straightforward at the first sight, measuring the wheel surface directly is generally more complex than measuring other quantities like the wheel-rail-force or the acceleration of the axle bearing, for which many commercially available and reliable sensors from many manufacturers exist, see chapters 3.2 and 3.3 for reference. In general terms, measuring the geometry of the wheel is more prone to errors, because the equipment used is more dependent on the environment. Optical sensors or cameras, for example, can be covered by dust or dirt and rendered useless, which is far less likely to happen to, for example, strain gauges. Physical sensors which follow the circumference of the wheel can get stuck or impaired by dirt or debris. Strain gauges and accelerometers, on the other hand, are much sturdier and less dependent on the environment. The advantage of wheel geometry measurement systems is that they measure a quantity directly regulated by the valid European standard EN15313, which is the dimension of the unroundness. This means that no algorithm or any other kind of conversion from the measured variable to dimensions of wheel defects is necessary, which could also be prone to errors. Another advantage for some of these systems is that not just the unroundness of wheels can be assessed, but also other profile dimensions (e.g. flange width) can be checked, although this is not the case for all of them.

Generally optical sensors are used to measure the profiles, but systems using cameras or sensors, which physically track the surface of the wheel are in use as well.

3.1.1 ARGUS II

ARGUS II and its predecessor system *ARGUS* produced by *Hegenscheidt MFD GmbH* [23] are both track-side systems and measure the radius deviations $\Delta R(\beta)$ of the wheel using the same principle, from which the circularity defect Δr, as stated in EN15313, can be easily determined. For the measurement, it is assumed that a wheel tread undergoes wear and, thus, all possible variations of out-of-roundness only affect the tread of the wheel. The assumption that the top of the flange is not subject to wear and that the radius remains constant around the circumference, like when it was newly produced, is even more important for this measuring principle. Figure 3-2 (a) shows a comparison between the profile outlines of a newly produced and a worn wheel.

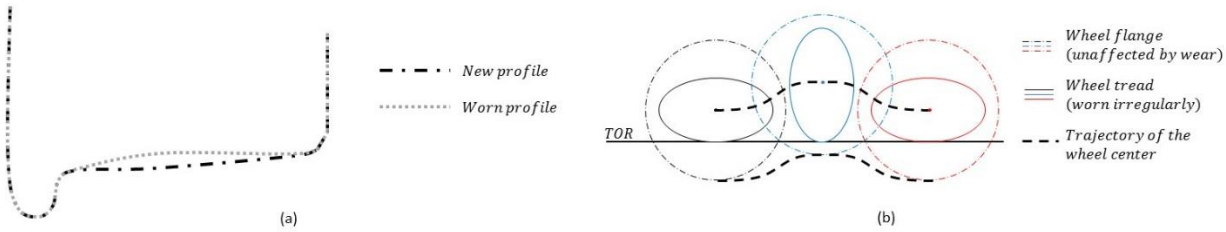

Figure 3-2 - (a) New and a worn wheel profile, the flange is unaffected by wear. (b) Top of the flange and center of the wheel follow a trajectory resulting from the polygonization on the wheel tread.

As can be seen, the flange diameter remains unaffected by wear. These assumptions are correct to a large degree, since the tread of a wheel is where the contact patch is located most of the time. The top of the flange never meets the rail. Thus, the tread is mainly subjected to wear. To use this fact to determine the radius deviation $\Delta R(\beta)$, the vehicle must pass the measuring site with low speeds of 15 km/h or less. An array of movable rollers with a small diameter are placed right next to the rail in such a way that the flange presses them downwards as the vehicle moves along the track, as depicted in Figure 3-3. It is recorded how far each roller has been pressed down. Since the wheel follows its circumference and kinematically moves up and down as the radius in the wheel-rail contact point changes when the wheel is turning, as shown in Figure 3-2 (b), the flange moves up and down with the wheel. What is effectively measured is the distance between the tread and the top of the flange, whose radius is considered to be constant around the circumference, as mentioned before.

Figure 3-3 - ARGUS II flange height measurement mechanism. Source: *[50]*.

In other words, the flange height is measured with this system. From this, it is very easy to calculate the radius $R(\beta)$ as a function of the angle around the circumference by subtracting the measured flange height from the constant outermost radius of the flange. Different types of unroundness can be identified from the measured flange height. The algorithm or process used to check the measured data for specific types of radius deviations is not disclosed by the company [49].

3.1.2 Wheel Tread Measurement System

The trackside vehicle inspection system developed by *MRX* [24] comprises multiple modules, one of which is called *Wheel Tread Measurement System*. Another module of the same vehicle inspection system is explained in chapter 3.2.2. It can detect flats as well as spalls and continuous types of undroundness. A camera is utilized to produce multiple pictures of the profile of each wheel. For a standard vehicle configuration with two-axle bogies, the measurement is carried out as follows. In order to be able to cover the whole circumference, the camera is mounted on a sled that moves alongside the track, as shown in Figure 3-4. The sled intercepts the first wheel of the bogie while the vehicle is passing and moves with it until the measurement of the whole wheel circumference is complete. This means that the two main tasks are producing images and keeping a constant distance between the sled and the wheel. A picture is taken every few milliseconds or for a 1-2 mm spacing along the circumference. Next, the sled with the mounted camera stops and starts moving backwards to intercept the second wheel of the first bogie. After that, the same measurement is performed for the two other wheels of the second bogie, which reaches the measurement device a few seconds later, depending on the vehicle speed. Since the velocity of the sled is limited, minimum bogie and wheelset spacings are required. For the camera to produce images of a sufficient quality, the vehicle speed must not be greater than 10 km/h.

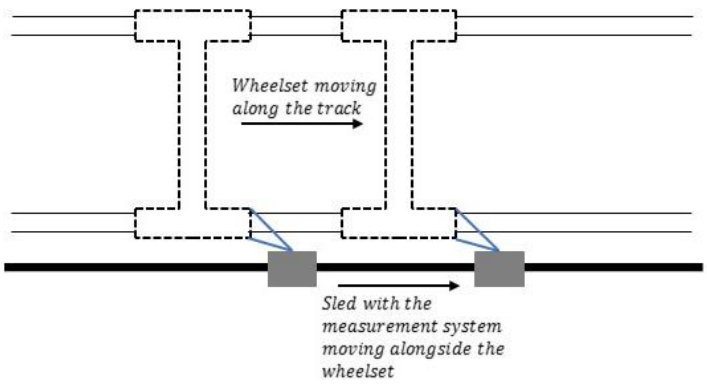

Figure 3-4 - Sled with the measurement system follows the wheelset to acquire measurements around the whole wheel circumference.

The measurement itself is performed as follows. A scattered beam of light from a laser, which is also mounted on the sled, forms a line on the wheel profile. It acts as an aid to the software calculating the shape of the profile. The picture taken by the camera is in greyscale, which in combination with the color of the laser-light used produces a white line on the final picture. This line can be detected by the algorithm, which later uses the information from the images to produce a topography of the surface of the wheel. Since reflections of light from the laser and other objects may resemble a white line in the final picture, the system uses the longest continuous white curve for the profile calculation.

Out-of-round wheels can then be determined by a software by analyzing the resulting calculated surface topography. For a simple classification, a damage index is calculated depending on the severity of the unroundness. The full exact process is not disclosed publicly.

It is assumed by the author that flat lengths l and circularity defects Δr, which are relevant for fulfilling the limits imposed by EN15313, can be calculated from the resulting topography. The camera and laser are built into a housing with a transparent window for the camera to be able to take pictures. Dust and debris can impair the vision of the camera. This issue is eliminated by an automatic cleaning function, the housing window is cleaned inside of a larger housing at the end of the track of the sled using water [51].

3.1.3 Calipri

In comparison to the other systems presented in this section, *Calipri* by *NEXTSENSE GmbH* [25] is not a fully, but instead a partially automated system, but it is still used to determine the geometry of wheels and is, therefore, mentioned for the sake of completeness. *Calipri* is a handheld device and the measurement is performed semi-manually, as seen in Figure 3-5. The measurement is taken by the means of lasers from a small distance, no contact to the wheel is required. The beams of light coming from the device are aimed at the part of the wheel profile that needs to be measured and the device is slightly moved until the measurement is completed. The measurement is processed automatically. Using this system, flats, spalls and continuous radius deviations can be determined [52] and the assumption is that flat lengths l and circularity defects Δr can be determined.

Figure 3-5 - Calipri handheld measurement device. Source: *[52]*.

3.1.4 TreadView

TreadView is a system developed by the company *BeenaVision* [26] and is a contactless system, utilizing optical imaging and laser-scanning to produce multispectral and multi-illumination images and subsequently, a surface map of the wheel profile, as shown in Figure 3-6.

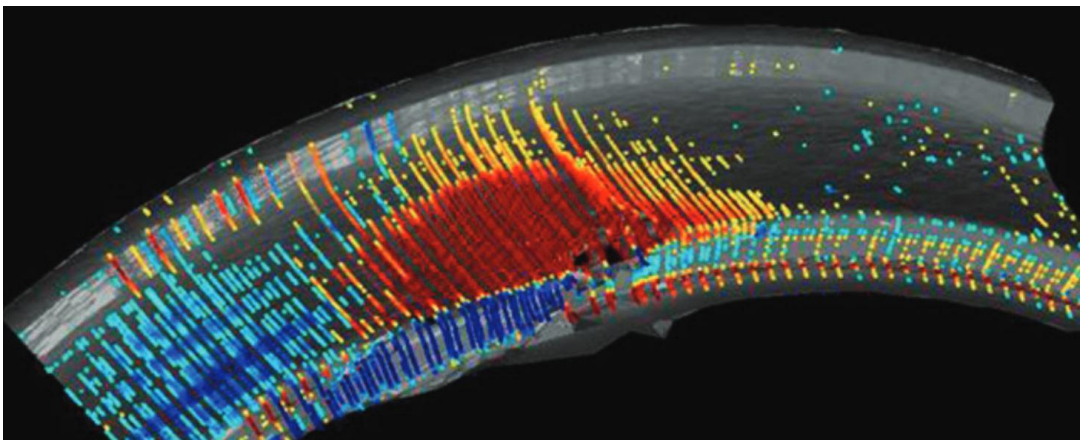

Figure 3-6 - Surface map of a wheel profile produced with TreadView. Source: *[53]*.

Image processing algorithms then assess the condition of the wheel indicating flats, spalls, build-ups, tread grooves and continuous radius deviations. It is not publicly disclosed how

exactly the data is processed to obtain this information. Other types of wheel defects, like broken flanges, can be identified as well but are not relevant for this piece of work. *Tread View* is a track-side system and can be used for high vehicle speeds of up to 100 km/h but can also be used at very low speeds [53].

3.1.5 Automatic Vehicle Inspection System

VEMS (Vehicle Equipment Measuring System) is a subsystem of the *Automatic Vehicle Inspection System* (*A.V.I.S.*), which was developed in cooperation between *MRX* [24], *Bombardier* [27] and *IBM* [28]. Lasers and optical imaging are used to produce measurements of the wheel surface, the assumption is that geometrical sizes of wheel defects can be determined. *VEMS* is a modular system and able to monitor axle end temperatures, brake pads, brake discs, wheel profiles, pantographs and wheel damages like flats. If a certain threshold is exceeded, the wheel is marked for re-profiling [54]. It is not publicly disclosed which threshold is used and how wheel damages are calculated from the data collected by the laser scanners and imaging system, but it is assumed that quantities relevant for the limits from EN15313 can be determined. Part of the installed system in depicted in Figure 3-7.

Figure 3-7 - Part of the VEMS equipment, at Midrand Depot. Source: *[54].*

3.1.6 W-Inspect

MERMEC [29] is the manufacturer of *W-Inspect*, a visual system that utilizes cameras and a lighting system can illuminate the wheel momentaneously. A depiction of how the system is set up is shown in Figure 3-8. The whole wheel circumference is examined. The resulting images are analyzed by the system.

Figure 3-8 - Visualizing the working principle of MERMEC W-Inspect. Source: *[55].*

This way, damages on the wheel tread can be detected, but no information is given on how exactly this occurs. However, it is assumed by the author that geometrical sizes of defects

relevant for an assessment conforming EN15313 can be determined. For a proper function of the system, the vehicle speed must be at or below 30 km/h [55].

3.1.7 Geopar-VKPsystem

RIFTEK Ltd. [30] offers multiple systems for the inspection of wheelsets, although none of them is fully automatic, i.e. the measurement takes place in a depot or shop and the wheelset must be removed from the vehicle, but it is mentioned for the sake of completeness. The system detects defects on the rolling surface and out-of-roundness by means of 2D laser scanners. It is not disclosed how exactly the information provided by the laser scanners is processed [56], but the assumption is that flat lengths l and circularity defects Δr can be determined.

3.2 Wheel-Rail-Force

Measurement of the forces between the rail and the wheels is currently one of the most common methods for detecting and assessing out-of-round railway wheels among commercially available systems. All systems presented in this section measure the vertical components of the normal forces N of the different wheels as defined in chapter 1.3, which are usually referred to as Q-forces. They are determined as the components of the normal wheel-rail-forces N that point in the positive z-direction of the reference system of the corresponding rail, which is explained in more detail in chapter 1.3. Those forces are measured as a function of time. Depending on how they change over time, an estimation can be made on how severe the radius deviations of the individual wheels are, with a perfect circle as a baseline.

Depending on the system, different measurement techniques are applied to determine Q_{dyn} for each individual wheel. The evaluation of the obtained Q-forces also differs between the systems. In the following subchapters, commercially available systems and the measurement techniques they use are described in greater detail.

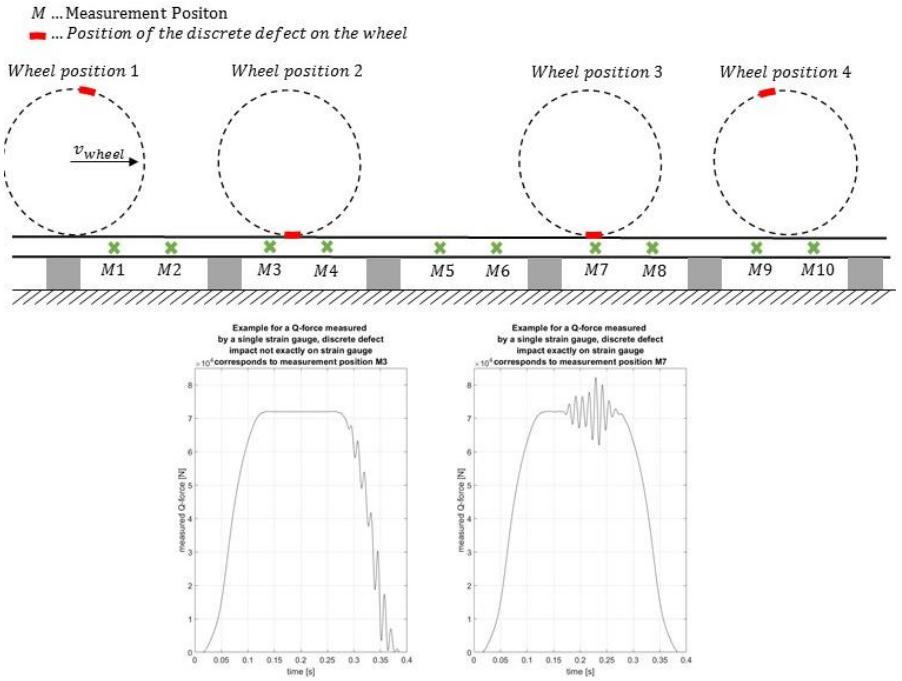

Figure 3-9 - Positions of the sensors and impact positions of a discrete defect for a wheel rolling on a rail. In measurement position M7, the discrete defect hits the sensor exactly and is easily detected.

One important detail that all the described systems have in common is that the measurement of the rail deformation, which is eventually translated into the Q-forces or bending moments, is confined to a very small length along the track. The measurement has a very small catchment area along the length of the track. This can be a problem for discrete defects, which usually extend over a very small part of the circumference, if the measuring spot is not hit exactly by the defect. To counteract this problem, most of the systems presented use a whole array of consecutive measuring devices, the total length of which often spans multiple wheel revolutions, usually around two. This increases the probability of a small discrete defect being in the catchment area of one of the measuring devices. Depending on the system, the measurements of the single measuring devices can be combined to a continuous, total Q-force signal, if the devices are close enough to each other, so that their catchment areas overlap. However, some of the systems assess each measurement separately and try to find the one during which the discrete defect hit the rail closest to a measuring point. An example of the setup of one of the systems and the effect on the detection of discrete defects is shown in Figure 3-9.

3.2.1 ARGOS Wayside train monitoring system

ARGOS is a system jointly developed by *Hottinger Baldwin Messtechnik GmbH* [31] and *Österreichische Bundesbahnen AG* [37]. An array of strain gauges attached to the side of each rail measure the strain in the rail at multiple, equally spaced points along the track, all placed in the middle between the sleepers, as shown in Figure 3-10. The rail deflections are largest at those points. Since the cross-section of the rail is known, the Q-force acting on it can be calculated, for example by means of finite element analysis.

As the cross-section is never exactly as specified due to imperfect manufacturing and tolerances, a calibration of the measurement is necessary. For this purpose, a vehicle of known mass must pass over the track section where the measurement is performed [57]. From the measured Q-force Q_{dyn}, the radius deviation is calculated as a function of the circumference of the wheel. However, the exact procedure of how this is done is not disclosed publicly and constitutes the special knowledge and experience of the manufacturer of the system [59]. This is not only the case for ARGOS, but for all other systems presented in this section.

Figure 3-10 - ARGOS Wayside Train Monitoring System, Source: *[58]*, cropped to remove other content.

An adaptation of the ARGOS system used by *Österreichische Bundesbahnen* [37] additionally measures the vertical acceleration of the rail when the vehicle passes [57], more information on this is given in chapter 3.3.

3.2.2 MRX Wheel Damage Measurement System

Another module of the aforementioned trackside vehicle inspection system by *MRX* [24] is the Wheel *Damage Measurement System*. Just like ARGOS, which is described in chapter 3.2.1, it measures the Q-forces acting between the rails and the wheels indirectly by measuring the strain in the rails by means of strain gauges. Figure 3-11 shows the strain gauge array on a set of rails without any protective covers installed, with two strain gauges attached to the rail per sleeper bay.

Figure 3-11 - MRX WDMS, Source: *[60]*.

No strain gauges are attached to the rail right above the sleepers, because it almost does not deflect in those places. Wheel flats are the only type of unroundness this system is designed to identify. For a perfectly round wheel, the force-time-curve determined by each strain gauge looks somewhat similar to an equilateral trapezoid with rounded edges and is very smooth, shown in the left graph of Figure 3-12. A wheel with a flat spot, on the other hand, produces a curve with a higher amplitude of the Q-force and oscillations. Refer to Figure 3-12 for an example of a possible measured signal. The deviation of a Q-force-signal of a wheel with a flat spot from that of an ideally round wheel can then be used to determine the length of the flat spot. How exactly this assessment is done is not disclosed by the manufacturer of the system [60]. Using this method, the signal from one strain gauge is theoretically sufficient to detect and assess a flat. Since it is not known where on the wheel the flat spot is located and where it will hit the rail, an array of multiple strain gauges placed along the length of the track is used to make sure a possible flat spot is detected by at least one of the strain gauges. Because of the spacing between the strain gauges, the

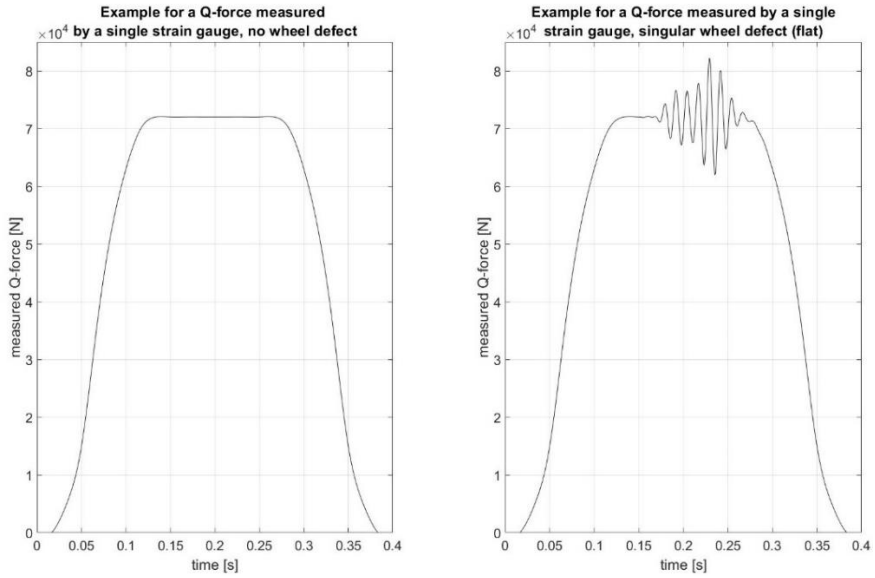

Figure 3-12 - Examples for Q-force measurements of a single strain gauge, difference between a Q-force signal without and with (defect hit the rail exactly above the position of the strain gauge) a singular wheel defect.

length covered by them corresponds to multiple wheel rotations, in order to be sure that the flat impact occurs in the vicinity of one strain gauge.

3.2.3 Detektionsanlage für unrunde Räder

*Dafur (*short for *Detektionsanlage für unrunde Räder*, or literally translated from German *detection system for out-of-round-wheels*) is a system developed by *Deutsche Bahn Systemtechnik GmbH* [32], which is a subsidiary of *Deutsche Bahn AG*.

Just like the two systems previously described, this system utilizes strain gauges to determine the Q-forces exerted on the rail by the wheels. This way, the Q-force for each wheel is obtained as a function of time, the signals of the whole array of strain gauges is converted into the total Q-force per wheel. An example for how such a Q-force signal may look is depicted in Figure 3-13. Like already explained in chapter 2.1, an ideally round wheel exerts a constant Q-force on the rail, which is equal to the static Q-force or the weight of the vehicle. This system uses the deviation of the Q-force from the static Q-force Q_{stat} over time as a baseline for the assessment of the severity of an unroundness by calculating a so-called dynamic coefficient (literally translated from the German original *dynamischer Beiwert*), the calculation if which is not publicly disclosed. Since the static Q-force cannot be easily identified from a Q-force signal of an out-of-round wheel, it is simply calculated as the average of the Q-force signal over time, as can be seen in Figure 3-13. Each wheel is deemed fit for service or in need of reprofiling or a replacement depending on the dynamic coefficient that was calculated for the specific wheel [61].

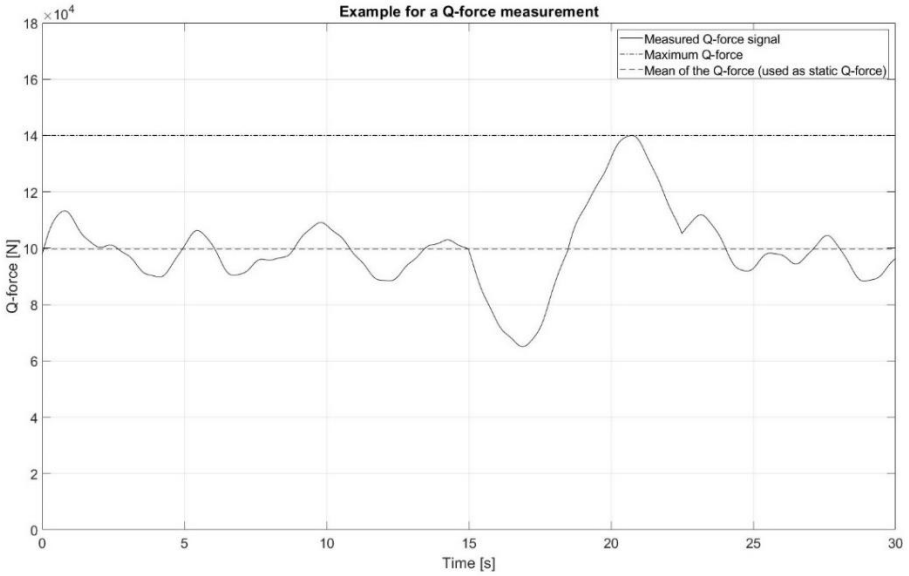

Figure 3-13 - Example of a possible Q-force-signal. Qualitative example created by the author.

This method constitutes a pure assessment of the dynamic effect a wheel has on the rail and does not try to determine the radius deviation around the circumference or any other geometrical features of the unroundness, which makes it a very easy and straight-forward method. Inspecting the wheels of a vehicle using this system only meets the criteria stated in the current standard EN15313 if the wheels that produce a high dynamic coefficient are subsequently inspected by a technician by hand.

3.2.4 MULTIRAIL Wheel Scan

MULTIRAIL Wheel Scan developed and manufactured by *Schenck Process GmbH* [33] measures the Q-force by means of force sensors in the sleepers. Several sleepers are replaced by concrete sleepers with force sensors built between them and the rail, as shown in Figure 3-14.

Figure 3-14 - Force sensors built into the sleepers.

This way, the whole force exerted on the rail is transferred to the sleepers through the force sensors. The variable that is used to assess the severity of the unroundness is still the Q-force, but it is measured differently than with the first three systems presented in this thesis. This system can detect and assess flat spots as well as continuous types of unroundness. The measured Q-force is then used to determine the severity of the unroundness. How exactly this is done and whether any geometrical dimensions of the unroundness are calculated is not disclosed by the manufacturer [62].

3.2.5 LASCA

INNOtec Systems GmbH [35] is the manufacturer of *LASCA*, another detection system for out-of-round wheels that bases its assessment on the Q-force. In the case of *LASCA*, the deformation of the rail is measured by an optical sensor that is clamped onto the rail, an illustration of which is visible in Figure 3-15 (a). Since the sensor is only clamped to the rail, no modification to the track itself is necessary, just like all systems that use strain gauges to measure the deformation of the rail. The optical sensor used functions like a slide resistance. Depending on the position where the laser beam hits the sensor, the voltage is divided accordingly. From the deformation, the bending moment within the rail can be calculated, which is a direct measure for the Q-force, as shown in Figure 3-15 (b). The resulting Q-forces are then analyzed to determine the severity of the out-of-roundness. With this particular system, sizes and numbers of flats can be detected. It can also measure the shape of continuous radius deviations (e.g.

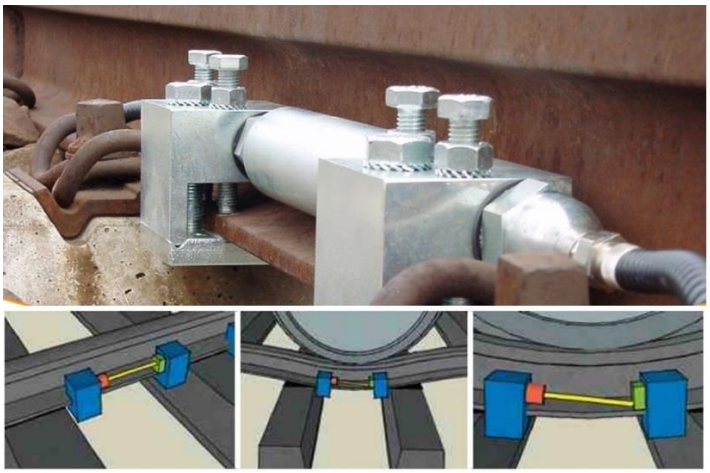

Figure 3-15 - (a) Optical sensor clamped to the rail. Source: *[63]*. (b) Measurement principle. Source: *[63]*.

polygonization). How exactly this is being determined is not publicly available knowledge [63].

3.2.6 ATLAS FO Wheel Defect Detection

The *Wheel Defect Detection* function of the *ATLAS FO* system can determine localized and continuous kinds of unroundness (e.g. flats and polygonization). The system is developed by *Voestalpine SIGNALING Siershahn GmbH* [34]. The principle is very similar to that of *LASCA*, which was already discussed in chapter 3.2.5. Clamp-on optical sensors are used to measure the deformation of the rail when the vehicle is passing, see Figure 1-6 for an illustration.

Figure 3-16 - Clamped on optical Sensors: Source: *[64]*.

This information is then used to calculate the force acting on the rail. In the case of *ATLAS FO*, the force is not used to assess the severity of the wheel unroundness. The system can differentiate between different kinds of unroundness. It gives a warning if pre-set tolerances for force levels are exceeded. This means that this system operates within the boundaries set by the standard EN15313. However, this also means that an extra effort needs to be put into the wheelset inspection, since a surveyor must check the wheel manually after a tolerance level for the wheel-rail-force has been exceeded [64].

3.2.7 GOTCHA

Lloyd's Register Rail [36] developed the system *GOTCHA*. Similar to previously described systems, the deformation of the rail is measured by means of optical sensors that are clamped onto the rails, as can be seen in Figure 3-17. From the measured force, wheel defects can be detected. In order to calibrate the force measurement, a vehicle with known mass must pass the measurement point. How exactly the size of the wheel defect is calculated is not publicly disclosed, just that the assessment is based on the measured force [66].

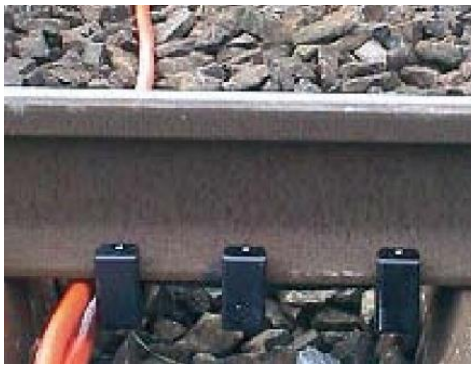

Figure 3-17 - Optical sensors clamped to the rail. Source: *[65]*.

3.3 Acceleration

Another variable used by multiple systems to assess the size or severity of an out-of-roundness is the acceleration of the axle bearing or the acceleration of the rail, depending on the system. This means that some of the systems presented in this subchapter are track-side systems, but for this measurement variable, train-borne systems exist as well. Based on the acceleration as a function of time, conclusions can be drawn about the geometrical features or the severity of the unroundness.

Systems in this category apply different techniques to measure accelerations, but in most cases commercially available acceleration sensors are utilized. For acceleration sensors attached to the rail, the fact that they can best detect a discrete defect that impacts right above or in the vicinity of the sensor needs to be considered, similar to the force measurement systems, like shown in Figure 3-9.

3.3.1 ARGOS Wayside train monitoring system in the railway network of *ÖBB*

The *ARGOS* system described in an earlier chapter is a force-measurement system and is shown in Figure 3-10 in chapter 3.2. However, one of the companies partly responsible for its development and also a railway operating company, *Österreichische Bundesbahnen* [37] (short: *ÖBB*), additionally utilizes acceleration sensors in its railway network which measure the acceleration of the rails. In this adapted version of *ARGOS*, the acceleration signals are mainly used for detection of out-of-round wheels. The force measurement explained in chapter 3.2.1 is mainly used to detect overloaded vehicles in order not to damage the infrastructure [57]. Since the valid standard EN15313 limits only geometrical sizes of flat spots and radius deviations of continuous types of unroundness, *ÖBB* uses the acceleration signal to calculate the radius deviation of the wheel around the circumference. How exactly this is done is not disclosed by the company. This way, a dynamic measurement method can be used (in this case, an acceleration measurement), while still satisfying the standard.

3.3.2 Perpetuum

Perpetuum developed by *Perpetuum Ltd.* [38] is a train-borne health monitoring system. The installed system is shown in Figure 3-18.

Figure 3-18 - Installed Perpetuum system. Source: *[67]*.

Its main advantage is a so-called energy harvester, which provides power by converting the continuous vibration and movement of the vehicle into electric energy, similar to a mechanical watch. It measures the acceleration as a function of time on each wheelset axle box. From the measured data, the health condition of the vehicle is assessed, including any possible out-of-round wheels. The data is transmitted via GPRS [67]. There is no publicly available information on how exactly the measured acceleration data is processed to derive a health state.

3.3.3 Erfassung von Laufflächenschäden an Eisenbahnrädern

A system for the detection of tread damages on railway wheels (literally translated from the German name *Erfassung von Laufflächenschäden an Eisenbahnrädern*) is manufactured by *PCB Synotech GmbH* [39]. The system consists of accelerometers, which are attached to the rails and measure their acceleration when a vehicle is passing. The recorded acceleration signal is used to detect out-of-round wheels. How exactly this is done is not publicly disclosed by the company. Both continuous and singular defects can be detected [68].

3.3.4 Insight Rail

The Swedish bearing manufacturer *SKF* [40] offers a train-borne monitoring system as well, which can also detect out-of-round wheels. It is battery-powered and measures the acceleration of the wheelset bearing, Figure 3-19 shows how it is mounted. Since *SKF* is a bearing manufacturer, the main purpose of the system was to detect damaged bearings. Because the acceleration is measured to achieve this, the data that is recorded can be used to assess the unroundness of the wheel, too. This system can wirelessly send the acquired data to a computer via a regular mobile phone network [69]. As with most of the other systems, it is the manufacturers trade secret how the unroundness is assessed using the data from the accelerometers.

Figure 3-19 - SKF monitoring system Insight Rail mounted on the axle box bearing. Source: *[69]*.

3.3.5 Wheel Out-Of-Roundness Monitoring

WORM (short for *Wheel Out-Of-Roundness Monitoring*) is developed and produced by *i-moss NV* [41]. The system consists of acceleration sensors which are glued to the rails and the sleepers using a two-component epoxy, like shown in Figure 3-20. Two sensors per rail are enough to cover the whole circumference of the wheel. The signal is saved in time domain and analyzed both in time and frequency domain in order to detect and classify out-of-round wheels. However, the exact procedure on how this is done is not publicly available. Both singular defects like flats and continuous radius deviations like polygonization can be detected [70].

Figure 3-20 - Acceleration sensors glued to the rail. Source: *[70]*.

3.3.6 Detection Of Flat Spots On Wheel Profile

RAFAMET S.A. [42] is the company responsible for the development of *Detection of Flat Spots on Wheel Profile*. Vibroacoustic sensors are installed over a distance of ten meters along the track, a depiction of which can be seen in Figure 3-21. They measure vibrations, which are presumably the accelerations of the track, but no further information is given about this. A software analyzes the recorded signal for patterns that are characteristic for flat spots, which this system can detect [71]. No information is given about the exact process that is used to analyze the signal and detect an out-of-round wheel.

Figure 3-21 - Vibroacoustic sensors installed along the track. Source: *[71]*.

3.3.7 Fahrwerksdiagnose und -überwachung

A train-borne system for the detection of out-of-round wheels was developed by *Siemens Mobility GmbH* [43] and is called *Fahrwerksdiagnose und -überwachung*. It is shown in Figure 3-22, where the cables leading to the axle box accelerometers can be seen. It is a system for the continuous monitoring of bogies and includes a flat and out-of-round detection using acceleration data from the axle box bearing. How exactly the data are processed to assess out-of-round wheels is not disclosed publicly [72].

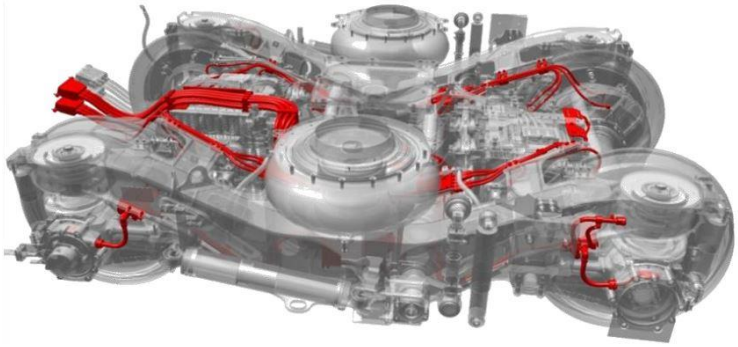

Figure 3-22 - Bogie monitoring system installed on a bogie. Source: *[72].*

3.4 Sound

As explained earlier in chapter 2.1, wheel defects constitute deviations from an ideal circle and, therefore, always induce some kind of dynamic response, resulting in sound waves. Acoustic wheelset inspection systems use this fact as a basis for assessing the unroundness of a wheel based on noise measurements. They measure either structure-borne or air-borne noise and draw conclusions on the severity of the unroundness based on certain characteristics of the recorded noise.

3.4.1 DSR

DSR by *Talgo* [44] is one of the four modules of the automatic measuring equipment of Talgo and is also called Wheel Surface Defects Detection module and shown in Figure 3-23. It utilizes ultrasonic sound waves to detect abnormalities in the wheel tread surface. Defects like flats, cracks or cavities can be detected by this method. Like most of the other mentioned systems, it is an automatic vehicle inspection system which examines the wheels as the vehicle passes the measuring site at a maximum speed of 10 km/h [73].

Figure 3-23 - Automatic measurement system. Source: *[73].*

The detection of wheel tread defects is based on the propagation of superficial ultrasonic waves, which is impaired by any imperfections in the tread surface. Superficial waves are called Rayleigh waves and can be found in the ground as a part of seismic waves produced by earthquakes, too. Two sensors for each rail are coupled to the wheel as the vehicle passes by, which effectively means they touch the wheel. Piezoelectric transducers are the main parts of the sensors. If a voltage is applied to them, they produce surface waves and vice versa, so they can both transmit and receive superficial ultrasonic waves. A defect is detected through a decrease of the signal, which one of the sensors receives, as some of the energy is reflected in the defect and does not reach the sensor [74]. An algorithm evaluates the measured data. How exactly the data is evaluated is not disclosed publicly.

3.4.2 Wheel Monitoring System

Mueller-BBM [45] is a German company responsible for the development of the *WMS* (short for *Wheel Monitoring System*). It is a track-side system that uses microphones to record the noise of a passing vehicle. That means that this system utilizes the noise produced by a vehicle to assess the condition of its wheels, detecting polygonization and flats. Aggregates like air conditioning units can also be monitored with this system but are not relevant for this thesis. The recorded noise is processed, and the results are saved for long-term monitoring of the condition of the vehicle [75]. It is not disclosed publicly how exactly the recorded noise is processed.

3.4.3 Versteckte Flachstellen- und Polygonermittlung

The system *Versteckte Flachstellen- und Polygonermittlung* (or literally translated from German *Hidden Flat- and Polygon Detection*) was developed by *Deutzer Technische Kohle GmbH* [46] and is another example for an acoustic wheelset inspection system. To detect out-of-round wheels, sensors measuring structure-borne noise are attached to the foot of each rail. An array of sensors in shown in Figure 3-24. The structure-borne noise in the rail is recorded this way as a function of time when a vehicle passes by. Flats or other discrete defects lead to a high peak in the recorded noise. A software evaluates the recorded noise signal and calculates the size of the irregularity on the wheel. It is not disclosed how exactly the size is calculated. The vehicle speed is also calculated by measuring the time between consecutive wheels reaching the measurement point. Since the distance between two wheels is a known constant, the speed of the vehicle can be calculated. It is also checked whether peaks in the noise level stem from one or from multiple surface irregularities. This is done by checking whether the time between two noise impulses corresponds to one turn of the wheel [76].

Figure 3-24 - Array of sensors measuring the structure-borne noise in the rail. Source: *[76].*

3.4.4 Frauscher Tracking Solutions

FTS (short for *Frauscher Tracking Solutions*) is a system by *Frauscher Sensortechnik GmbH* [47] that uses fiber optic cables to monitor the condition of trains. One of the purposes of this system is to detect flats. A technology called DAS (short for distributed acoustic sensing) is used. The name is due to the fact that noise traveling through the ground in the proximity of a track can be detected. The noise is the result of vehicles passing by on the track. It can be measured by using a fiber optic cable that is placed in the ground alongside a track, like shown in Figure 3-25. The distance between the cable and the track is a known constant.

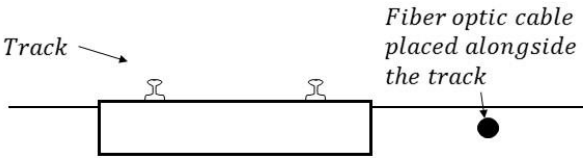

Figure 3-25 - Placement of the fiber optic cable in the ground next to the track. Interpretation of this system by the author.

Laser pulses are sent through one optic fiber of the cable. The light travels through the cable and is absorbed on the other end. Many particles and imperfections within the optic fiber smaller than the wavelength of the light lead to backscatter and, thus, reflection of part of the light. This phenomenon is also known as Rayleigh scattering. After the light pulse has reached the end of the cable and the light reflections of the light pulse have traveled back to its starting point, another pulse can be sent. This means that the time resolution of measurements with this system is a function of light speed in the optic fiber medium and the length of the cable. Additionally, the cable length is limited by the attenuation of light as it travels through the fiber. Typical maximum cable lengths of 40-50 km can be achieved, *Frauscher* limits the cable length to 40 km and pulses are sent with a frequency of 2500 Hz. This means that every 80 km along the track an optoelectric device needs to be installed, which generates and measures the outgoing and incoming light pulses and its reflections [77], as depicted in Figure 3-26.

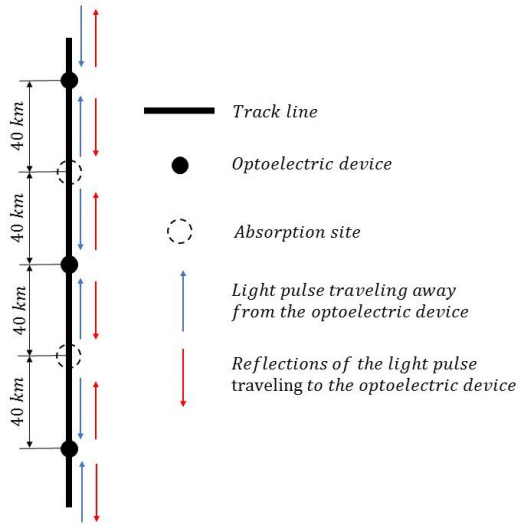

Figure 3-26 - Placement of the optoelectric devices along the track. Created by the author for a visual representation.

The measurement itself is a light intensity measurement. The intensity of the reflections of the light pulse resulting from Rayleigh scattering is measured as a function of time at the starting point of the light pulse. When a soundwave hits the fiber, it is slightly deformed. This happens because soundwaves are compression waves traveling through a medium, which lead to strains within that medium. As a result of the deformation of the fiber, the amount of light that is reflected changes. The changes in the light intensity of the reflections between two pulses are a measure for the change in noise hitting the optic cable between the same two pulses. As the noise hitting the cable changes, so does the deformation of the fiber and with it the amount of light reflected. This effectively turns the optic cable into a microphone along its whole length. Depending on the time at which a change in the intensity of the reflected light is identified, the distance along the track at which the noise hit the optic cable can be calculated. The measurements are then processed by a computer and the severity of the unroundness is calculated. How exactly this is done is not disclosed publicly.

3.4.5 RailBAM

RailBam by *Wabtec Corporation* [48] is a trackside automatic inspection system that monitors the sound level produced by passing vehicles. A picture of the system is shown in Figure 3-27. The main function of the system is the detection of faulty wheelset bearings, but wheel defects

that emit noise as the vehicle passes by can be detected as well. Certain sound characteristics of wheel defects can be recognized by the system, how exactly the recorded sound is processed is not publicly available knowledge [78].

Figure 3-27 - Acoustic automatic inspection system installed alongside a track. Source: *[78]*.

4 Measurements of the Effects of Unround Wheels

In chapter 2, general effects of out-of-round wheels were explained. Specific effects and consequences of polygonized wheels and flats were shown qualitatively. In the present section, actual quantitative Q-force and axle box acceleration measurements induced by unround wheels are discussed.

4.1 Polygonization

Since no measurements with polygonized wheels could be conducted by the author because of the lack of a vehicle with both polygonized wheels and the necessary measuring equipment, measurements from the literature are used to investigate the effect of polygonized wheels on dynamic quantities. Measurements are available in Paper B [7] of the PhD thesis [8] of *A. Johansson*, which was previously described in chapter 1.4. The measured effects are the Q-force and the rail bending moment. The polygonized wheel had a polygon with a wavelength of 0.29 m with an amplitude of 0.125 mm, a roundness measurement is shown in Figure 1-3 (b). The wavelength of 0.29 m corresponds to a polygon of order $n = 10$ or $n = 11$, depending on whether the small, irregular peak at a circumference position of around 800 mm in Figure 1-3 (b) is considered part of the polygonization or as an irregularity. Measurements and simulations have been performed for two axle load values. The measurements, as well as simulation results from the source paper are shown in Figure 4-1. The blue solid lines in Figure 4-1 are trend lines of the measurements performed, the dashed lines represent values obtained from numerical models. The blue lines have been added by the author to better visualize the measurements. The peak vertical wheel-rail contact force and bending moment are shown in the left and right diagram, respectively.

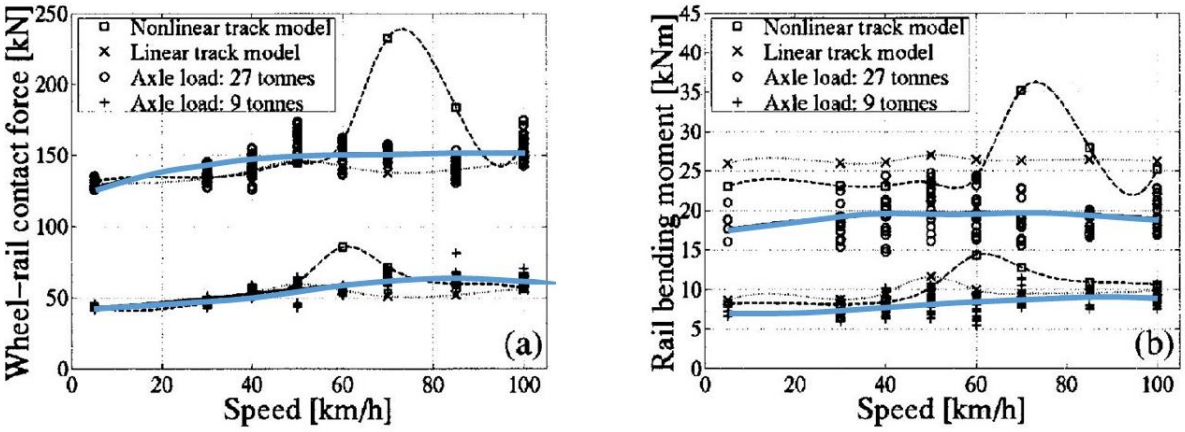

Figure 4-1 - Wheel-rail contact force and rail bending moment from a vehicle with a polygonized wheel, measurements and simulations. Measurements were performed on Svealandsbanan in 2000. Source: *[7].*

For small speeds, the measured peak wheel-rail contact force corresponds to the static Q-force Q_{stat}. With increasing speed, the measured Q-force increases, albeit the increase only corresponds to a few ten percent of the static Q-force Q_{stat}. Especially for a high axle load of 27 tons, a maximum in the measured peak forces can be observed at a vehicle speed of around 50 km/h, with a decrease and another increase with increasing vehicle speed. According to *Johansson* [7], the peak at 50 km/h is a result of the P2-resonance, where the track and unsprung

masses oscillate around the track stiffness. More information on the P2-resonance frequency can be found in chapter 5.2.2. An important property of the axle box accelerations and Q-forces induced by polygonized wheels is the continuity around the entire wheel circumference. A peak in the dynamic Q-force Q_{dyn} occurs for every peak in the radius deviation, and the resulting acceleration and force amplitudes are relatively small. This is in contrast to the short, but high-amplitude peaks in acceleration and force amplitudes induced by flats, which are investigated in the following chapter 4.2.

4.2 Flats

For flats, axle box acceleration measurements were performed. The axle box acceleration measurements that are investigated were recorded on a commuter train with a single-axial accelerometer mounted to the cover of the axle box, with a sampling rate of 8 kHz. The vehicle possesses two two-axle bogies, and the investigated flat is present on the right wheel of the second axle of the leading car, which is indicated in Figure 4-2 (b). The left wheel of the same wheelset also shows peaks within the axle box acceleration data, indicating a small damage to the wheel tread, although they are much smaller on average. The length of the flat on the right wheel was measured to be 12.4 mm in longitudinal direction, which is also the largest dimension of the flat. A total of about 6 hours of recorded acceleration data exist. However, not all data can be used for this investigation, since it was found that the flat only shows in right-hand curves in driving direction, the most likely position of the flat is depicted in Figure 4-2 (a). This reduces the usable data considerably to about 1 hour. In a right-hand curve, the vehicle moves to the left in lateral direction, which means that the flat must be located on the field side of the wheel tread of the right wheel.

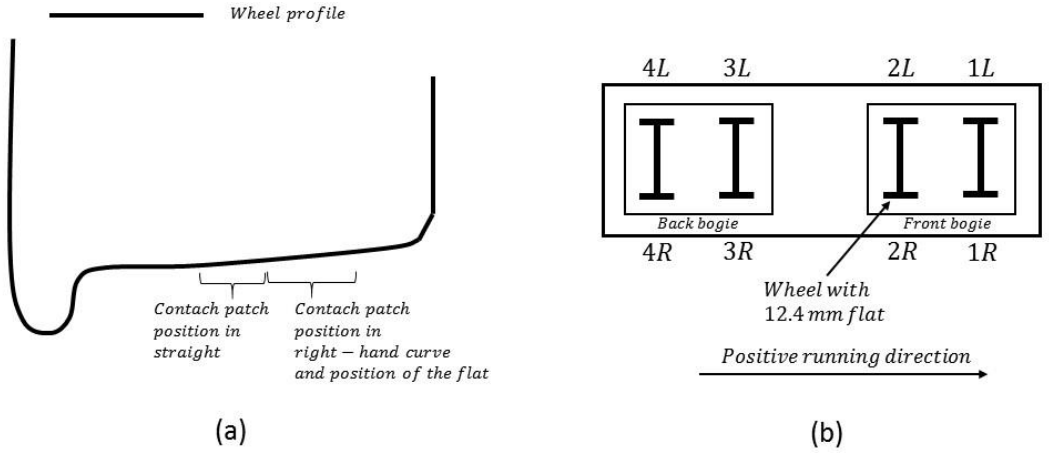

Figure 4-2 – (a) Most likely position of the flat that produced the measured accelerations. (b) Position of the wheel with the flat on the car, it is present on the right wheel of the second wheelset.

Typical data, which were recorded with the flat on wheel 2R as indicated in Figure 4-2 (b), are shown in Figure 4-3. The upper graph shows the acceleration measurement on the bearing box of the wheel with the flat, the middle graph shows the curvature of the track with respect to the driving direction of the vehicle, and the lower graph shows the vehicle speed. The higher acceleration peaks where the curvature takes a large, positive value can be clearly seen. For this reason, only data where the curvature exceeds $5 \cdot 10^{-4}$ m^{-1}, which corresponds to a curve radius of 2000 m or smaller, is considered. An example of a detailed view of the acceleration data is shown in Figure 4-4 (a). The repeated flat impacts can be distinguished very well, and

the time difference between two peaks corresponds to the vehicle speed and wheel radius, as indicated in Figure 4-4 (a). In Figure 4-4 (b), the acceleration of a single flat impact can be seen. The available data was sorted by track curvature and vehicle speed. Only data with a track curvature as explained above was considered. The speed range was divided into intervals of length 10 km/h, starting at 0 km/h.

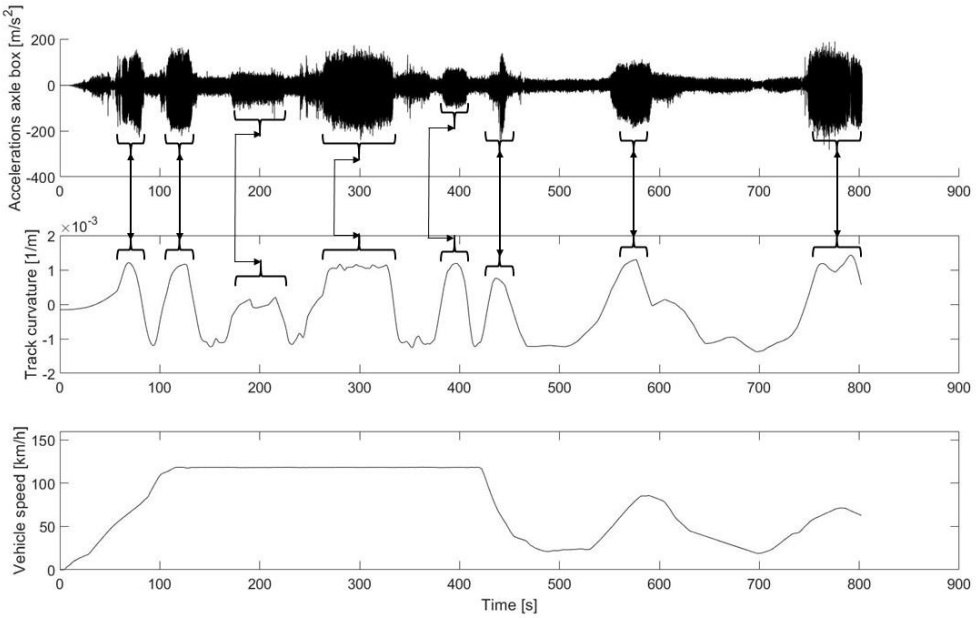

Figure 4-3 – Example for vertical axle box acceleration data, track curvature and vehicle speed as a function of time. High acceleration values correspond with a positive curvature (right-hand curves), which are marked up.

The characteristic or representative speed for each interval was set at the middle of each interval. Figure 4-5 shows how the speed range was divided into intervals. For each speed interval, the absolute maxima of all flat impacts of all available data for that speed and curvature range were determined.

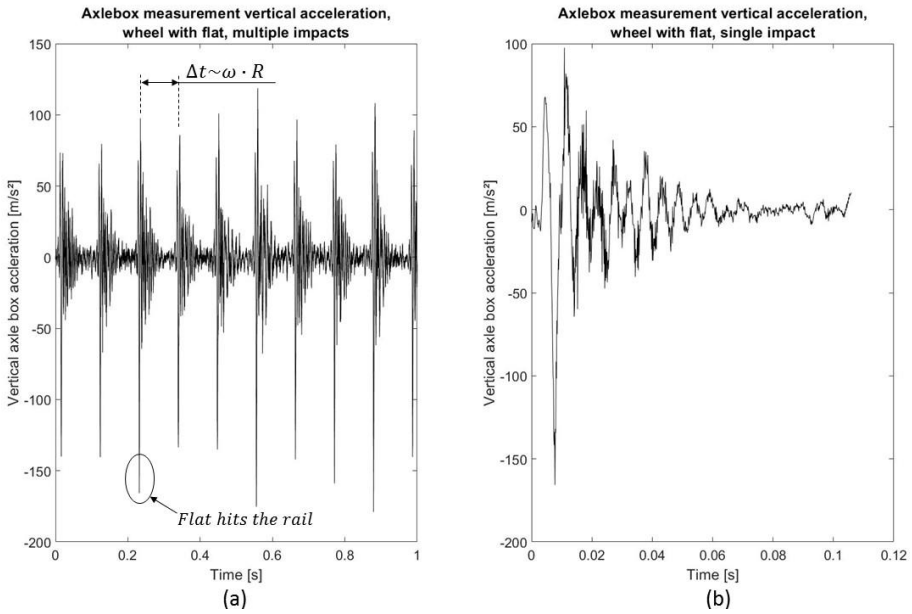

Figure 4-4 - (a) Several subsequent flat impacts lead to significant maxima of the vertical acceleration. (b) Acceleration (z-direction at axle box) during one wheel revolution.

After determining the maximum accelerations, the mean values and standard deviations of the available maximum accelerations were calculated per speed interval. A boxplot of the available acceleration maxima of the axle box is depicted in Figure 4-6 for each speed interval. It is clearly visible that the measurement data is very scattered.

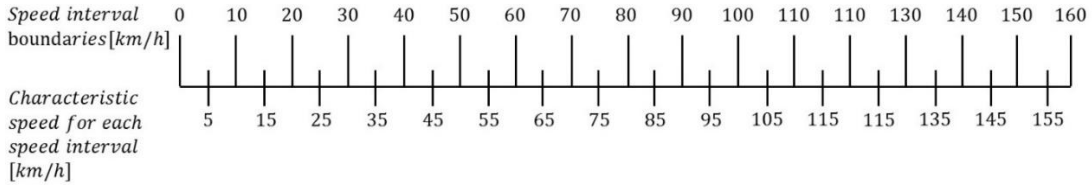

Figure 4-5 - Speed intervals used for sorting the acceleration data.

It is clear that the same flat, which has a constant length l, can lead to different axle box accelerations. This may be due to differences in the track structure, rail condition, track irregularities and other uncontrollable environmental conditions and already indicates the complexity of deducing the flat length from the acceleration data.

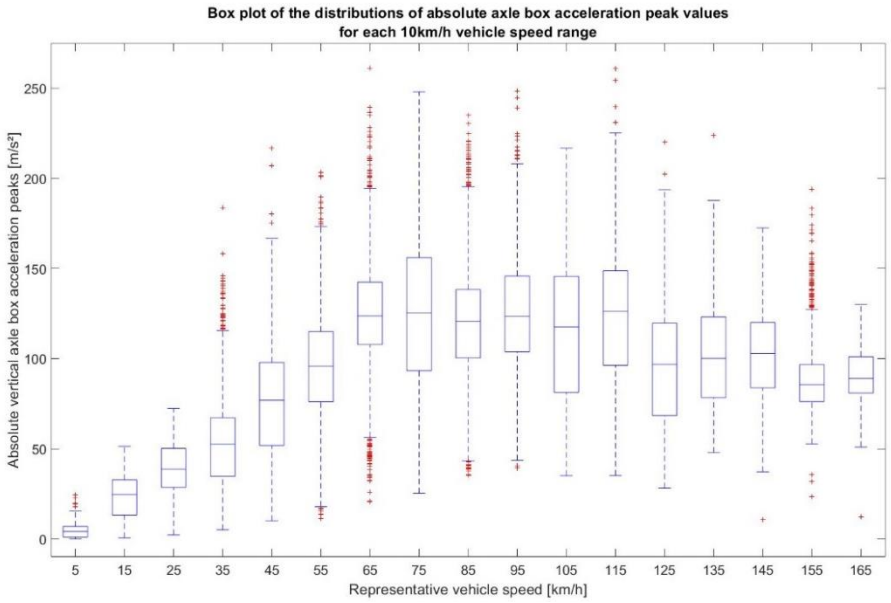

Figure 4-6 – Box plots of the available maximum accelerations for each vehicle speed interval. The median, upper and lower quartiles and outliers are shown. The maximum whisker length corresponds to 1.5 times the interquartile range.

Looking more closely at the acceleration data of a single flat impact, as shown in Figure 4-4 (b), an oscillation can be seen that fades away and seems to have a characteristic frequency. After performing frequency analyses of acceleration data packets (each of one second) for all speeds and all available data, it can be shown that the frequency of this oscillation barely changes with vehicle speed. A typical result of one FFT of an acceleration data packet that is one second long is depicted in Figure 4-7. For each FFT performed, the frequency, at which the largest peak occurs, can be found, which is 117 Hz in the example in Figure 4-7. Some more examples of frequency analyses of acceleration data packets at different vehicle speeds can be found in Appendix C. A probability distribution has been created of all frequency values acquired this way, which is shown in Figure 4-8. For most data packets (each of one second), the frequency with the largest amplitude in the FFT can be found in a range between

106 and 117 Hz. Therefore, the conclusion is that a characteristic eigenfrequency, either of the complete track-vehicle system or the vehicle itself is excited.

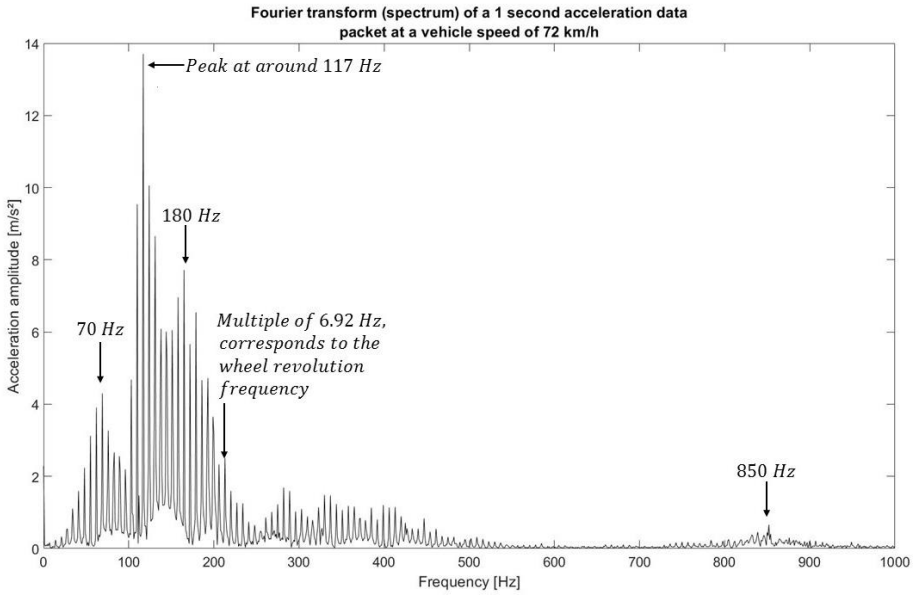

Figure 4-7 - FFT of an acceleration data packet of one second length. The largest peak shows at 117 Hz, smaller peaks at ~180 Hz and 70 Hz. For this FFT, the highest peak occurs at 117 Hz.

Judging from the value of the frequency range determined from the measured data, it could be the first bending eigenmode of the wheelset. To show that it is likely that this is the eigenfrequency that was excited, an eigenmode measurement is performed on a wheelset in installed condition, which is documented in chapter 4.2.1. For some of the data packets, the largest amplitude occurs in a lower frequency range, which is about 60 Hz to 80 Hz. This is most likely the P2-resonance frequency of this vehicle on the track, which is known to be in the range of 50-100 Hz [3]. Two more small resonances can be observed in frequency ranges of about 180 Hz to 190 Hz and 870 Hz to 880 Hz.

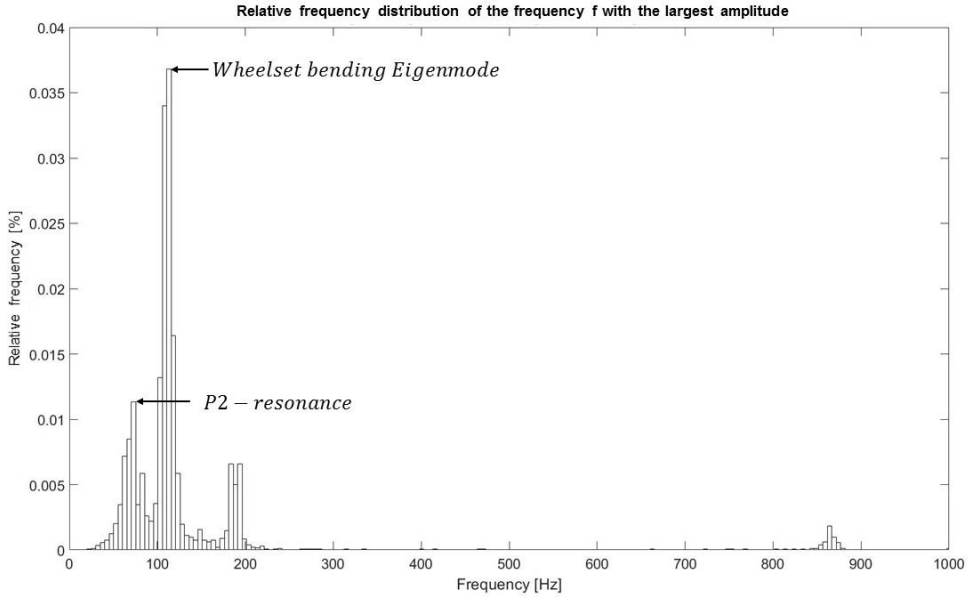

Figure 4-8 – Relative frequency distribution of a frequency f being the largest in an FFT of an acceleration measurement data packet one second long (data from all vehicle speed intervals). Over 3000 data packets were examined.

4.2.1 Eigenfrequency Measurement of a Wheelset

In order to show that the oscillation that is induced by the flat impact is likely to be the first wheelset bending eigenmode, the corresponding eigenfrequency is determined experimentally. To determine eigenfrequencies of any structure, all frequencies need to be excited (broadband excitation), and the subsequent oscillation of the structure will be dominated by the eigenfrequencies. To excite a whole range of frequencies, an impulse hammer may be used. The measurement itself is an acceleration measurement. If the eigenfrequency of a known eigenmode is measured, the positions of the nodes can be estimated in advance of the measurement in order to avoid an incorrect measurement.

The first bending eigenmode of a wheelset possesses two nodes with equal distance from the center of the axle, if a symmetric wheelset is assumed, as shown in [79]. The center of a wheelset and the outermost parts on the axle show the largest movement in vertical direction in this case, as depicted in Figure 4-9. This figure is theoretically only valid for a wheelset suspended by an infinitely soft spring. A wheelset supported by the rails is subjected to other boundary conditions. This changes the shape and the frequency of the eigenmodes. The large deflections in the middle and at the ends of each axle should still appear, albeit they may become smaller. The measurements were performed by attaching single-axis accelerometers to a wheelset of the same type of vehicle that the axle box accelerations with a flat were measured on, in the measurement positions marked in Figure 4-9. Wax was used to attach the accelerometer to the wheelset. It was excited by hitting it with an impulse hammer in the excitation positions marked in the same figure. The attached acceleration sensor can be seen in Figure 4-10 in measurement position 1. The resulting acceleration measurements were transformed into the frequency domain by means of FFT to analyze the oscillations resulting from the broadband excitation.

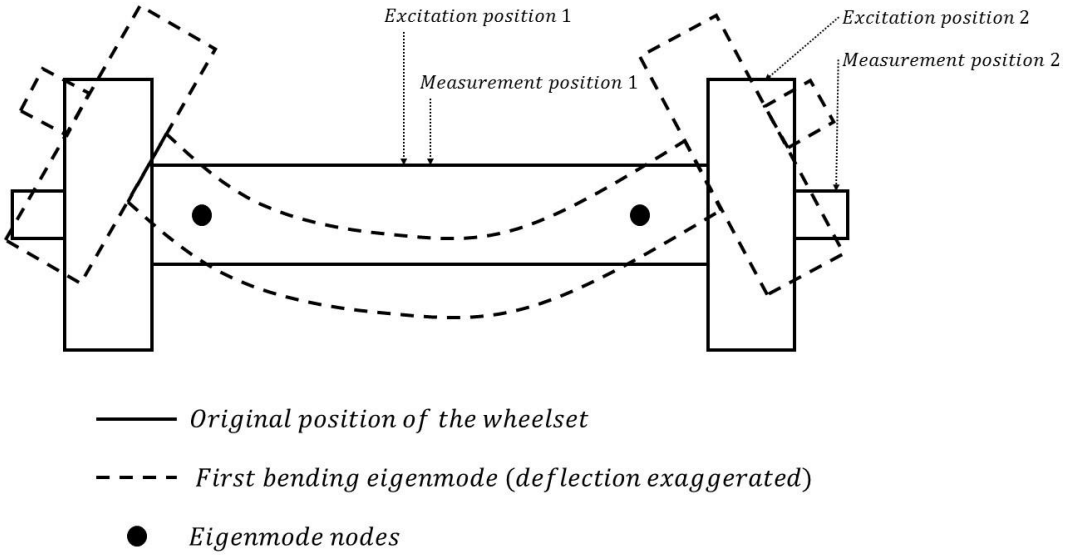

Figure 4-9 - Depiction of the first bending eigenmode of a general wheelset. The measurement and excitation positions for the eigenfrequency measurement are marked.

Measurement and excitation positions 1 are perfectly suited for detecting a bending eigenmode of the wheelset, because the middle of the axle is where the largest deflections occur. This way, the oscillation can be excited very well and the acceleration sensor is subjected to the largest accelerations.

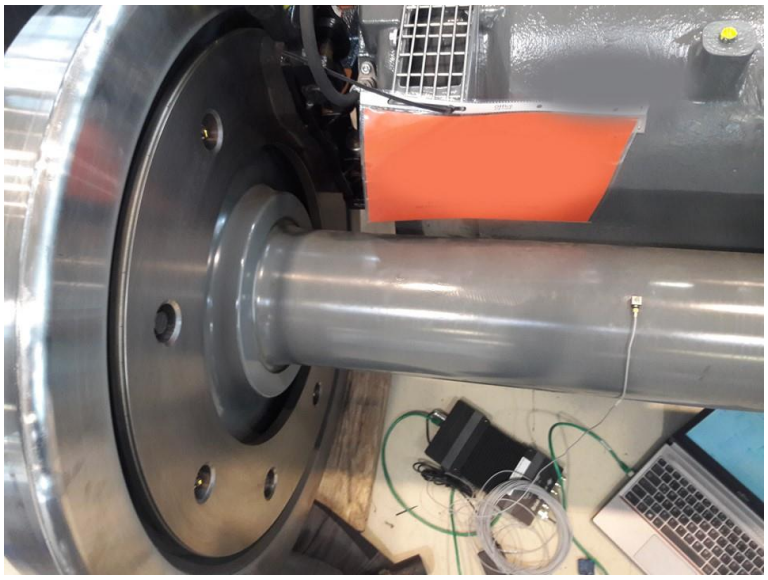

Figure 4-10 - Single-axis acceleration sensor (vertical), attached to the middle of the wheelset axle using wax.

For this reason, the excitation and measurement in this position yield a very clear result with large acceleration amplitudes at the expected frequency. This is shown in an FFT of the measured accelerations, which is shown in Figure 4-11. The most dominant peak value can be found at 110 Hz. The peaks between around 200 Hz and 400 Hz may be the result of higher order bending or other eigenmodes but are not investigated further, as they are not within the investigated frequency range.

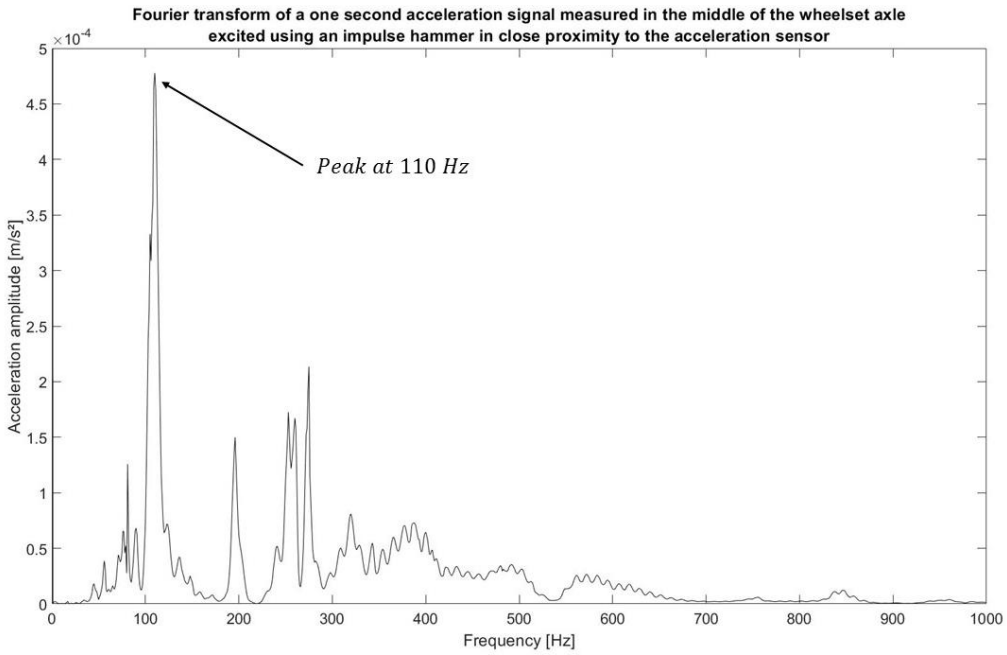

Figure 4-11 - FFT of an acceleration signal measured in the middle of the wheelset axle. The excitation of the eigenmode was accomplished using an impulse hammer. The peak occurs at a frequency of 110 Hz.

The measurement position 2 in Figure 4-9 corresponds to the measurement position of the acceleration data acquired from the driving vehicle, the excitation position 2 corresponds to the excitation by the impacting flat. However, for the eigenfrequency measurement, the

excitation occurs on a wheelset standing on the ground, on the topmost point of the wheel tread, in a downwards vertical direction, in contrast to the impact by the flat, which occurred on the lowermost point of the wheel tread. Because the wheel disc is very stiff radially and the excitation occurs close to a node, the bending eigenmode is barely excited, yet still visible at 117 Hz in Figure 4-12, slightly shifted in frequency, presumably because of the additional mass and stiffness of the bearing (because the measurements are performed on the outer axle box cover), as well as the changed excitation position. The other peaks are the result of other eigenmodes being excited by the hit with the impulse hammer.

In the axle box acceleration measurements, the frequency with the largest amplitude most commonly lies in the range 106 – 117 Hz. In the eigenfrequency measurements of the wheelset, values of 110 Hz and 117 Hz with high acceleration amplitudes were found. From the completed eigenfrequency measurements and the axle box acceleration data, it is concluded that the oscillation present in the acceleration data is likely to be the first bending eigenmode of the wheelset, excited by the flat hitting the rail. However, what must be kept in mind is that other, so far unidentified mechanisms may play a role in the formation of the dominant frequency range.

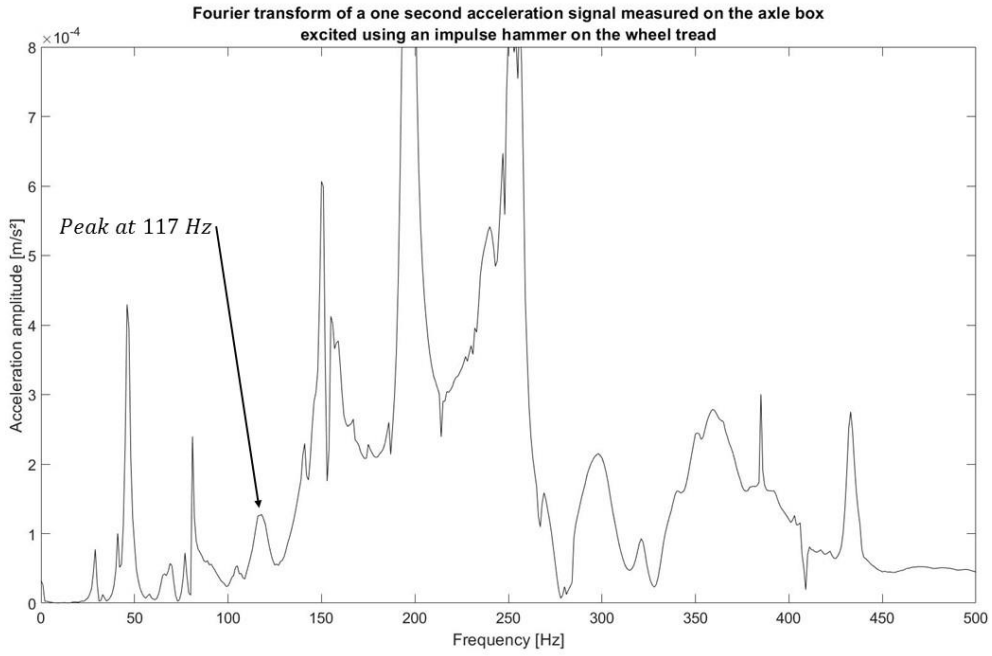

Figure 4-12 – FFT of an acceleration signal measured on the axle box housing. The excitation of the eigenmode was accomplished using an impulse hammer on the wheel tread. A peak occurs at a frequency of 117 Hz.

5 Analytical and Numerical Investigations

Because no or just a few measured data of accelerations at the axle box is available for both polygonization and flats, it has been decided to create a multibody simulation model for the investigations of the correlations between geometrical properties of out-of-round wheels and the axle box accelerations they induce, as well as effects of vehicle and track parameters on the axle box accelerations. For flats, measurement data is available, and it is used for model validation.

5.1 Simulation Model for Numerical Investigations

Multibody simulation, or short MBS, is a commonly used method to simulate the motion behavior of mechanical systems. A mathematical model of the simplified mechanical system is created, and the resulting differential equations are solved by the means of numerical integration. The simplified system consists of either rigid or elastic bodies which are connected to each other or the inertial system by massless force elements or constraints [80].

The software tool *SIMPACK 2018x Rail* has been used for all MBS calculations performed in this thesis. Some functions specific to the railway industry are implemented in this software, the most important one for this thesis presumably being the modeling of wheel-rail contacts. *SIMPACK Post 2018x* is the matching post processor. More information on *SIMPACK* can be found in references [10] or [81].

5.1.1 Wheel-Rail Contact Simulation

The wheel-rail contact is a mathematical tool to determine the forces resulting from the contact between the wheel and the rail. The total wheel-rail-forces are calculated in three steps. First, the contact patches between the wheels and corresponding rails are determined by analyzing the overlap of the corresponding profiles. Next, the normal forces are calculated, since they are input variables for the tangential force calculation. For this thesis, the normal force calculation is the most crucial step since the Q-force is mostly determined by the normal force. Using the normal forces, the tangential forces can be computed, completing the wheel-rail-force calculation. The contact search between the rail and wheel profiles is only performed in the y-z-plane, which is not desirable for simulating certain wheel defects, like flat spots, more information on this will be given later [10]. For the current model, the Equivalent Elastic Contact in *SIMPACK* is used, see the software documentation [10] for further information.

5.1.2 Vehicle Model

The MBS model used is a relatively simple model that possesses all main properties and characteristics of a railway vehicle. It is a modification of the *SIMPACK Rail* training model, see [10] for reference. The vehicle model does not represent a specific vehicle, but rather railway vehicles in general, since the analyses in this thesis should be applicable to most or all railway vehicles. The model parametrized with a typical set of parameters for a mainline vehicle is hereafter referred to as 'base model'. Starting from the base model, the goal is to study the influence of the main model parameters on the dynamic effects caused by out-of-

round wheels in a parameter study. As shown in Figure 5-1, it is a four-axle car with two bogies.

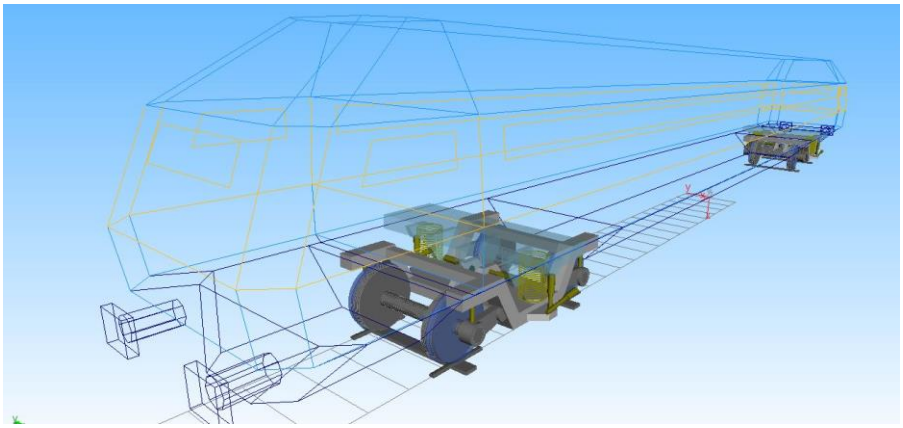

Figure 5-1 - Visual representation of the MBS vehicle model. Created by the author in SIMPACK.

For the simulation of discrete defects, the rigid wheelset is replaced by a flexible wheelset, modeled as a Euler-Bernoulli-Beam, see chapter 5.3.2 for more information. The body positions, masses, moments of inertia, spring stiffnesses and damping values for the base model are available in Table A-4 and Table A-5 in Appendix A. The damping characteristic of the nonlinear primary damper for the base model is depicted in Figure A-1 in Appendix A, since this damper acts in the z-direction, which is relevant for these investigations.

What is worth mentioning is the tendency of the unsprung vehicle mass to increase with increasing nominal wheel radius, which can be observed for existing vehicles. Therefore, a linear relationship between the two variables is implemented in the base model, with the unsprung mass as a function of the nominal wheel radius, like in Equation 5-1.

$$m_{unsprung}(R) = C_1 \cdot R + C_2, \qquad R \in [0.3; 0.625] \qquad \text{Equation 5-1}$$

The values for the constants are derived by applying a least-square linear fit to four data points typical for a light rail vehicle, commuter vehicle, coach and locomotive, respectively. The values for the constants from the least-square fit are C_1 = 7859.4 kg/m and C_2 = -1700.7 kg, the four data points and the least-square first-order polynomial fit are depicted in Figure 5-2.

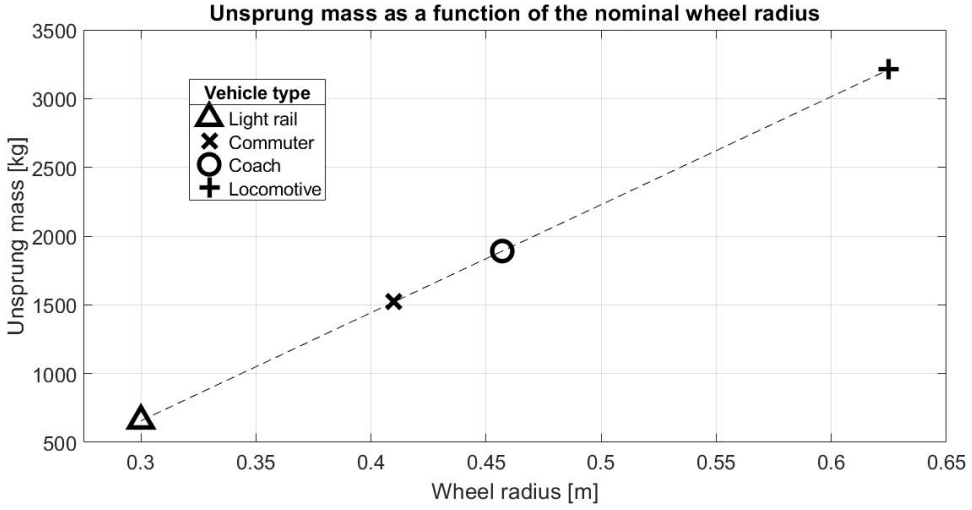

Figure 5-2 - Linear relationship between the wheel radius R and unsprung mass m_w of a vehicle, derived from a least-square fit of a line to four data points from actual vehicles.

Figure 5-3 shows the structure of the car model, including all modeling elements that influence the dynamic behavior in the vertical direction. Force elements that have a mostly lateral or longitudinal effect are not shown, e.g. the anti-yaw-dampers.

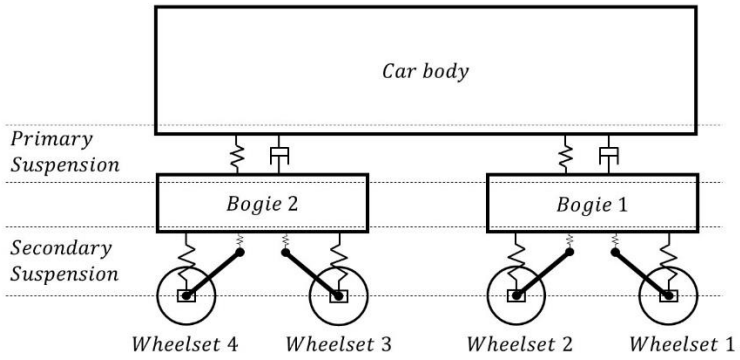

Figure 5-3 – Schematic structure of the vehicle model with all the main vertical components: Primary spring including damping, secondary spring and vertical dampers.

5.1.3 Track Model

Three kinds of track models were used for the calculations during this thesis. The simplest version of a track model is a completely stiff track, meaning the rails are connected to the inertial system. A more advanced track model consists of a single mass that represents all the masses in the track, connected to the inertial system via a single force element, which considers the stiffness and damping characteristics of the track with a linear characteristic and is shown in Figure 5-4 (a). Values for the mass of the track body as well as stiffness and damping values that have proven to best represent mainline tracks have been chosen for the base model and are available in Table A-6 of Appendix A. A more detailed track model can be achieved by modeling the mass of the rail and the mass of the underlying foundation and the corresponding stiffnesses separately, as shown in Figure 5-4 (b). For both track models, the masses and force elements move with the wheelset along the track. The masses as well as the stiffness and damping values used for the force elements that model the rail pad and the foundation stiffness and damping can be found in Table A-6 in Appendix A.

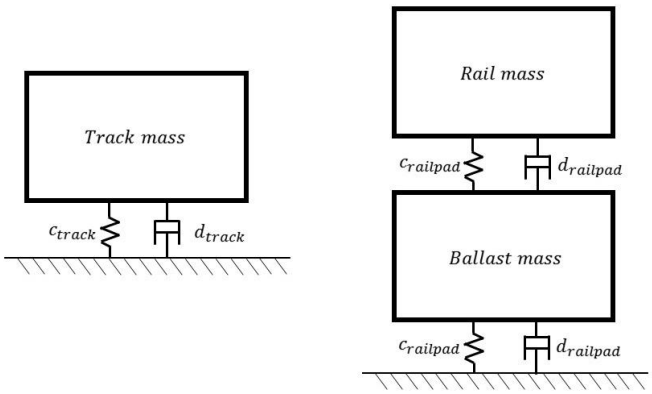

Figure 5-4 - (a) Topology of the track model using a single mass. (b) Topology of the track model using two masses.

5.1.4 Modeling of the Unroundness

One of the most crucial steps in the creation of an MBS model for this thesis was the application of the radius deviation on the wheel. *SIMPACK* [10] provides a possibility to add radius deviations $\Delta R(\beta)$ to the wheel as a function of the circumference angle β, which is measured as the angle between the starting position of the wheel and the y-z-plane of the wheel. The radius deviation can be provided to the program in three different ways [10], two of which

were used in the present thesis. For more information, refer to the corresponding chapters 5.2 and 5.3. With the radius deviation given as a function of the wheel circumference angle, it is applied by changing the nominal wheel radius, or in other words, shifting the wheel profile in the z-direction and changing the diameter of the whole wheel. This might be a consequence of the contact algorithm [10] of *SIMPACK*, which only looks for interpenetrations of the rail and wheel profiles in the y-z-plane of the wheel, as shown in Figure 5-5.

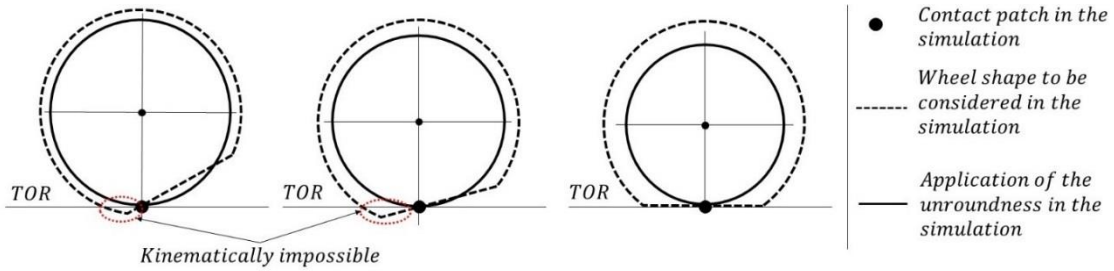

Figure 5-5 - Application of the unroundness by changing the whole wheel diameter, based on the radius deviation currently present in the y-z-plane of the wheel.

This is, of course, a simplification of reality, but should be sufficient for the investigations within the scope of this thesis, if it is dealt with properly. Because the wheel circumference angle β considered for determining the radius deviation that will be applied is always the one currently in the y-z-plane of the wheel and the whole wheel diameter is changed by the resulting radius deviation ΔR, there are cases in which the wrong radius is applied, as can be seen in Figure 5-5. This might occur when flats are modelled. The error occurs when a part of the wheel circumference that is not directly underneath the wheel center contacts the rail, outside of the y-z-plane of the wheel, as shown in the second depiction in Figure 5-5. In the model, the radius where the contact should actually occur is not considered, but instead the radius directly underneath the wheel center is used for the calculations. This can lead to inaccurate results if the contact patch should be outside of this y-z-plane. To avoid this issue, the radius deviation function $\Delta R(\beta)$ that needs to be applied in the case of flats, is the kinematic wheel center trajectory as a function of the wheel circumference angle β that the wheel center would follow if it were to roll with an infinitesimally small speed, instead of the actual radius deviation as measured on the wheel. This way, the vertical position of the wheel $z(\beta)$ as a function of the circumference angle β is accurately replicated and kinematically impossible positions of the wheel, as shown in Figure 5-5, are prevented. More information about the radius deviation function $\Delta R(\beta)$ for flats is presented in chapter 5.3.

For polygonized wheels, this approach works well, as can be seen from Figure 5-6, and the resulting errors are negligible.

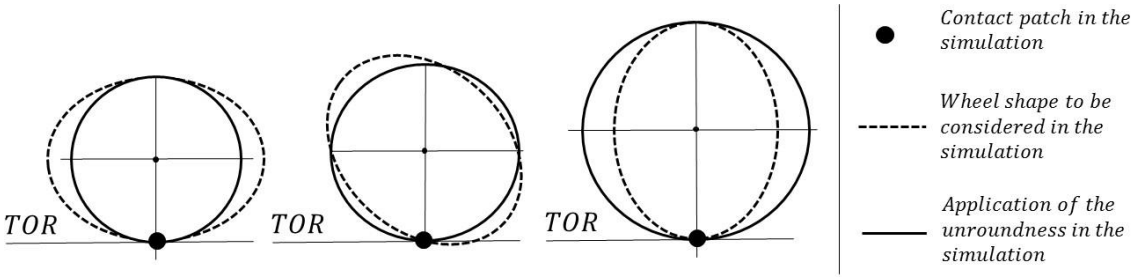

Figure 5-6 – Application of the unroundness by changing the nominal wheel diameter for the whole wheel.

5.2 Polygonization and Other Continuous Radius Deviations

As stated in chapter 1.2, limits for radius deviations from the perfect circle exist within the informative annex of standard EN15313, which contains suggested limit values for the maximum allowable circularity defect Δr. It is defined as the difference between the largest and smallest radius measured on the wheel, as depicted in Figure 1-6. The limit values can be found in Figure 1-5. They are a function of the actual wheel diameter D_{act} and the maximum speed v_{max} of the vehicle and do not depend on how the radius deviation evolves with the circumference angle. One goal in this section is to analyze whether this approach makes sense considering the dynamic loads induced by the out-of-round wheel. The main goal is to check for a simple correlation between the accelerations of the wheelset induced by a polygonized wheel and the amplitude of the polygonization. In the first step of this investigation, perfectly polygonized wheels are assumed, which means that the radius deviation follows a harmonic function perfectly and only contains one order or frequency, which is a valid assumption for polygonized wheels. A sample radius deviation of this type is shown in Figure 5-7 (a). Further calculations will deal with continuous radius deviations of mixed frequencies. An example for this type of radius deviation can be found in Figure 5-7 (b).

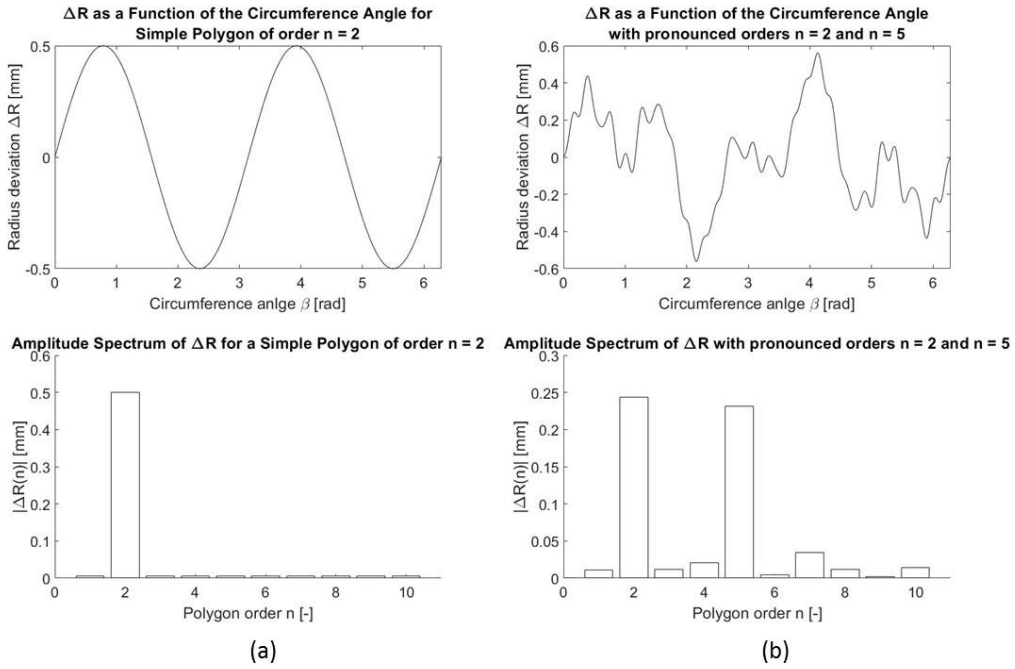

Figure 5-7 - (a) Example for a single-frequency radius deviation of order n = 2. (b) Example of a radius deviation including multiple frequency components, with dominant orders n = 2 and n = 5.

As already mentioned previously, radius deviations can be applied within *SIMPACK* in several different ways [10]. The following combinations of parameters can be provided to *SIMPACK*, which are ideal for modeling polygonization:

- Radius deviation amplitude ΔR_0 and polygonization order n for a polygon of a single frequency
- Fourier coefficients for mixed-order radius deviations

The first method can only apply radius deviations of a single wavelength or order. A polygonization of order $n = 1$ means that the radius deviation around the whole

circumference of the wheel has one peak and one trough, constituting an eccentricity. The maximum radius deviation amplitude ΔR_0 and the order of the polygonization n are input variables, the radius deviation as a function of the wheel rotation angle β is as follows.

$$\Delta R(\beta) = \Delta R_0 \cdot \sin(n \cdot \beta) \qquad \text{Equation 5-2}$$

In reality, radius deviations never occur with exactly one single order or wavelength. In some cases, however, one order can become dominant, meaning that the amplitudes of radius deviations of all other orders can become very small in comparison to the dominant order. Therefore, this method is perfectly suited to model radius deviations of such kind and is used to model polygonized wheels with one dominant frequency.

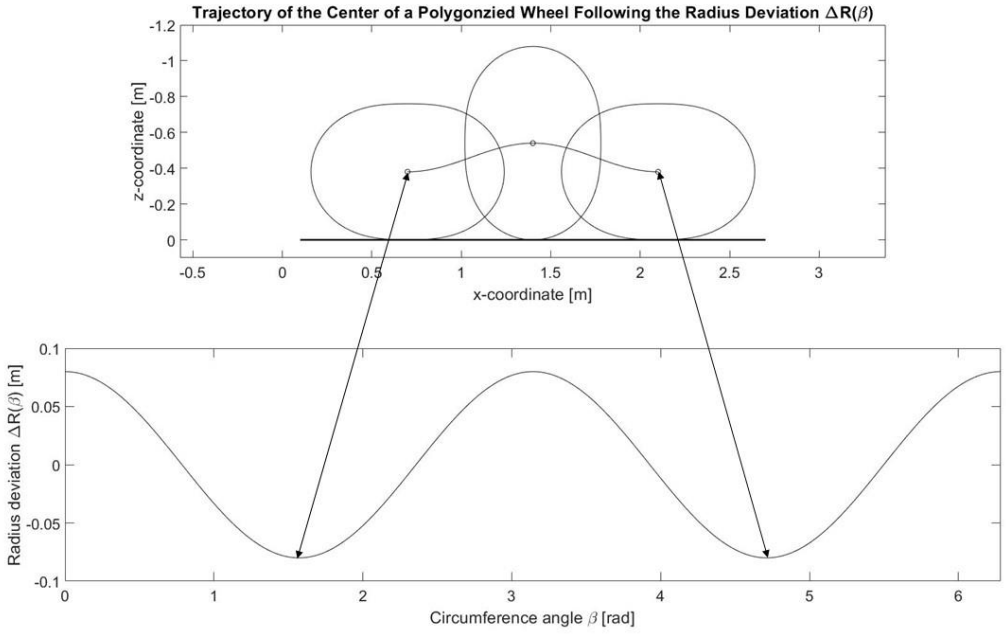

Figure 5-8 - Trajectory of a polygonized wheel (exaggerated) following the radius deviation, assuming a perfectly stiff track and wheel-rail contact, with no loss of contact.

For the second method, Fourier coefficients are the input variables that are used to specify the out-of-roundness. This method is suited to apply an arbitrary radius deviation to an arbitrary degree of accuracy, depending on the number of Fourier coefficients used. Radius deviation functions with large gradients require the development of the Fourier series to a high order, meaning that many Fourier coefficients need to be calculated to describe the curve with a small error. With given Fourier coefficients $A_0, \cdots, A_n$ and $B_0, \cdots, B_n$, the function describing the radius deviation as a function of the wheel rotation angle can be written as:

$$\begin{aligned} \Delta R(\beta) &= A_0 + \sum_{i=1}^{n} A_i \cdot \cos(i \cdot \beta) + \sum_{i=1}^{n} B_i \cdot \sin(i \cdot \beta) \\ &= A_0 + \sum_{i=1}^{n} C_i \cdot \cos(i \cdot \beta - \varphi_i) \end{aligned} \qquad \text{Equation 5-3}$$

5.2.1 Analytical Approach

Owing to the smooth, continuous radius deviation functions of polygonized wheels with no discontinuities, analyzing this problem analytically is the first method of choice to get a simple

understanding of the influence of the main parameters – namely, the maximum radius deviation ΔR_0 and the order of the polygon n – and for a first check of the results of the numerical model. The radius deviation $\Delta R(\beta)$ of a polygonized wheel is given in Equation 5-3. Assuming the wheel-rail contact and track to be completely stiff and allowing no loss of contact for simplicity, the trajectory of the center of gravity of the wheel corresponds to the radius deviation, as shown in Figure 5-8, which shows an exaggerated polygonization of a wheel of order $n = 2$. Under all the assumptions made previously, the wheel COG follows the contour of the wheel tread, which in turn can be expressed by Equation 5-2, making $z_{wheel}(\beta) = \Delta R(\beta)$. To obtain the radius deviation as a function of time, the wheel rotation angle β can be expressed like in Equation 5-4, ω being the angular velocity of the wheel. Double differentiation with respect to the time t yields Equation 5-5, which is the vertical acceleration of the wheel COG.

$$\beta = \omega t \qquad \text{Equation 5-4}$$

$$\ddot{z}_{wheel}(t) = \Delta R_0 \cdot \left(\frac{v}{R}\right)^2 \cdot n^2 \cdot \sin\left(n\frac{v}{R}t\right) \qquad \text{with} \qquad \omega = \frac{v}{R} \qquad \text{Equation 5-5}$$

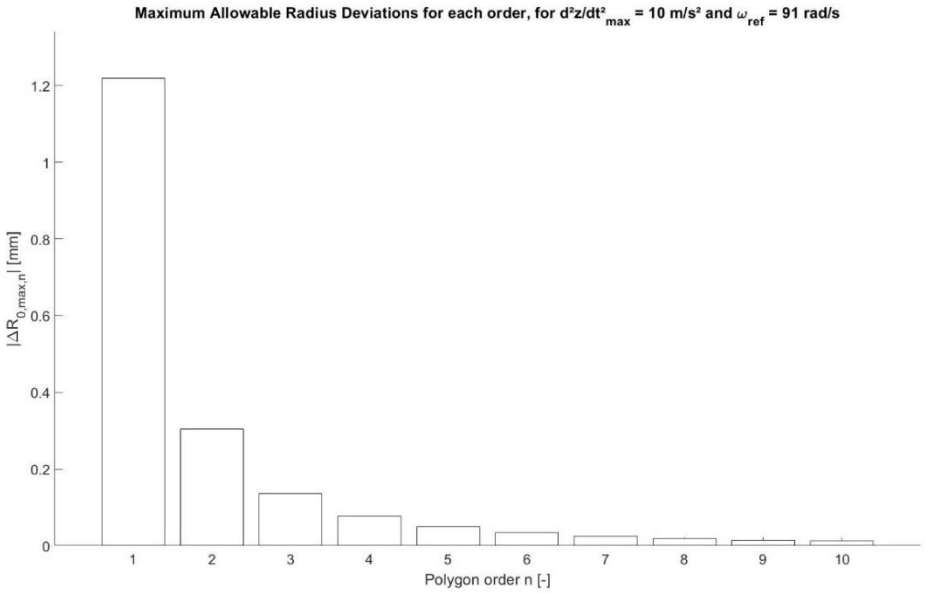

Figure 5-9 - Maximum allowable radius deviation for each order with inverse quadratic decline of the allowable radius deviation to maintain the same maximum acceleration.

Analyzing the influence of the main parameters, one can find that the radius deviation amplitude ΔR_0 only influences the acceleration linearly, whereas the vehicle speed v, the polygon order n and the nominal wheel radius R are squared. This indicates that limiting the maximum allowable vertical acceleration is not possible by simply limiting the radius deviation amplitude ΔR_0. The current limits of EN15313 do account for the vehicle speed v and wheel diameter D, but do not consider the order of the unroundness. Examining the influence order of the polygonized wheel, with a constant radius deviation amplitude ΔR_0, vehicle speed v and wheel radius R, it is clear that the accelerations rise with rising polygon order n. If the maximum acceleration should be limited to $\ddot{z}_{lim}$ for a given reference speed v and wheel radius R, this yields different radius deviation amplitude limits for different order polygons. The maximum radius deviation $\Delta R_{0,n,max}$ of order n, if only a single order is present, can be calculated as:

$$\Delta R_{0,n,max} = \frac{\ddot{z}_{lim}}{\omega_{ref}^2 \cdot n^2}$$ Equation 5-6

The rapid, inverse quadratic decline for higher order polygons to maintain a constant acceleration level can be seen in Figure 5-9. The same applies to out-of-round wheels with radius deviations that consist of multiple harmonics, which can be written like in Equation 5-3. Differentiation of Equation 5-3 and substitution of $\beta = \frac{v}{R}t$ yields Equation 5-7.

$$\ddot{z}_{wheel}(t) = \sum_{i=1}^{n} C_i \cdot \left(i\frac{v}{R}\right)^2 \cdot \cos(i\frac{v}{R}t - \varphi_i)$$ Equation 5-7

The coefficients C_i can simply be derived from a roundness measurement and a subsequent Fourier transform. Again, speed v and nominal wheel radius R are fixed for different orders, they can be placed outside of the sum. After rearranging and setting the acceleration to a limit value $\ddot{z}_{lim}$, a condition can be found that needs to be fulfilled to limit the acceleration $\ddot{z}$ to the specified limit value, if all phase angles φ_i are assumed to be equal. A more detailed study considering different phase angles will not be conducted at this point. The effective radius deviation $R_{0,eff}$ with regard to the wheelset acceleration is defined as the sum of the coefficients of the Fourier transform of the actual radius deviation, weighted with the squares of each respective order. The limit value $\Delta R_{0,eff,max}$, that is defined in Equation 5-8, can be calculated by setting the maximum allowable acceleration $\ddot{z}_{lim}$ at a reference speed v, which can, for example, be the maximum operating speed v_{max}.

$$\frac{\ddot{z}_{lim}}{\omega_{ref}^2} = \Delta R_{0,eff,max} \cdot 1^2 = \Delta R_{0,eff,max} > \Delta R_{0,eff} = \sum_{i=1}^{n} C_i \cdot i^2$$ Equation 5-8

The value $\Delta R_{0,eff}$ corresponds to the radius deviation of a first-order polygon that results in the same maximum acceleration value $\ddot{z}$ as the actual total radius deviation of all orders combined, $\Delta R_{0,eff}$. The limit value $\Delta R_{0,eff,max}$ can also be interpreted as the radius deviation ΔR_0 of first order that leads to the limit acceleration $\ddot{z}_{lim}$, hence the factor 1^2 in Equation 5-8. Checking this limit value can be performed in two ways. The roundness measurements required for checking the limit values from the current standard can be used to check the proposed limit value $\Delta R_{0,eff,max}$ with minimal computational effort. A more effective way of checking this limit value is using acceleration data from the vehicle. Since the acceleration was limited when deriving Equation 5-8, it is simple to continuously monitor the acceleration levels and check them against the set limit value to ensure that the wheels are fit for service and to detect an emerging polygon, without the large effort of bringing the vehicle to a depot for inspection.

5.2.2 Numerical Analysis

The analytical approach in chapter 5.2.1 has several drawbacks. First, a possible lift-off of the wheel is not considered. Considering the large accelerations for high order polygons and high speeds, this is not impossible. Secondly, the dynamic properties of the wheel-rail contact and track are not considered. They may influence the acceleration level $\ddot{z}$ and the behavior of the acceleration levels in the speed domain. Also, the dynamic effects of the whole vehicle have been neglected in this analytical method. For all numerical investigations, the base model with the base parametrization as described in chapter 5.1.2 is used, and all relative changes of the parameters are with respect to the base model. All bodies within this model, including the

wheelset, are modeled as rigid. The applied unroundness constitutes a simple polygon of a single order and is applied to the back wheelset of the front bogie, as shown in Figure 5-10.

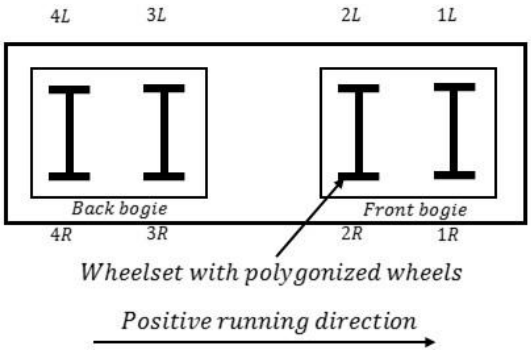

Figure 5-10 - Position of the polygonized wheelset in the numeric calculations.

To cross-check the analytical and numerical methods, a simulation with a $\Delta R_0 = 0.5\ mm$ was performed with a fixed rail body, meaning the track was modeled rigid. The track model was switched from rigid to elastic as the next step to assess the error resulting from the rigid track assumption in the analytical analysis. An analytical calculation, using Equation 5-5, was performed with the same parameters as the numerical calculations. The results of this comparison are shown in Figure 5-11.

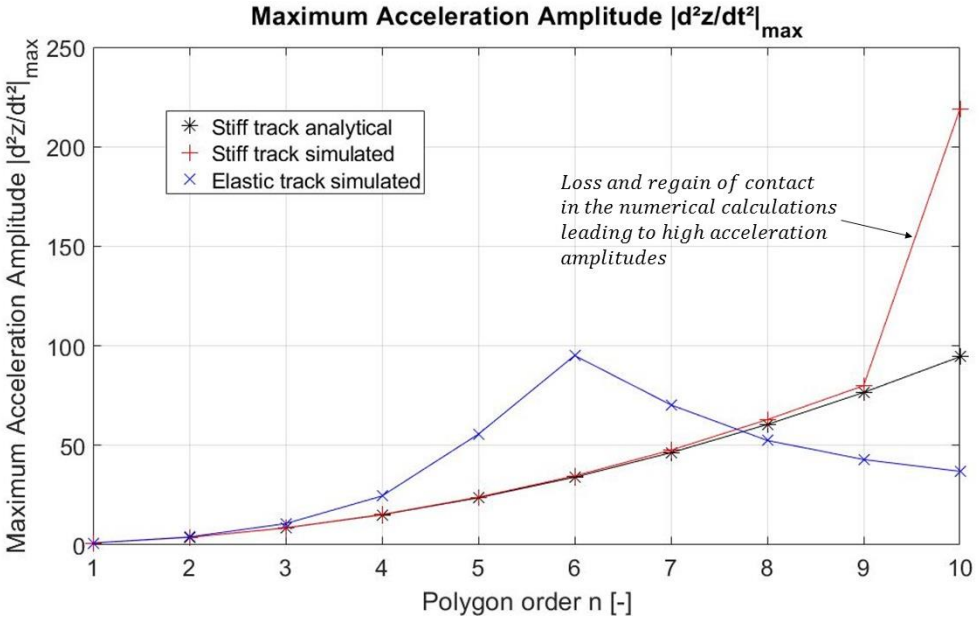

Figure 5-11 - Maximum acceleration values as a function of the polygon order for three different models, including the analytical analysis. Radius deviation amplitude ΔR_0 used is $\Delta R_0 = 0.5\ mm$.

The rigid track model and analytical results compare very well, because the influence of the very stiff wheel-rail contact appears to be rather small. It is interesting to note that the peak for the rigid track model for n = 10 results from a contact loss and regain of contact, which is not possible within the analytic approach. The elastic track model shows completely different results, with a peak at n = 6. At the simulated speed of 20 m/s, the wheelset rotation frequency in combination with the 6th-order polygonization corresponds to 41.5 Hz, which coincides with the P2-resonance for this model, which was found to be at 40.3 Hz in a linear eigenfrequency calculation. The P2-resonance is the oscillation of the unsprung mass of the vehicle and the track mass around the track stiffness. The frequency f_{exc} of the vertical excitation, which

results from the unroundness, is a combination of the wheelset rotation frequency $f_{wheelset}$, as well as the order of the polygonization n, and can be calculated by using Equation 5-9. When the excitation frequency f_{exc} and the P2-resonance frequency f_{P2} match, high acceleration amplitudes $\ddot{z}$ can be observed. It is worth noting that f_{exc} is the same for two completely different wheels, if the order of the polygonization n and the nominal wheel radius R are scaled with the same factor.

$$f_{exc} = f_{wheelset} \cdot n = \frac{v}{R \cdot 2\pi} \cdot n = \frac{\omega_{wheelset}}{2\pi} \cdot n \qquad \text{Equation 5-9}$$

5.2.2.1 Sensitivity Analysis

So far, some parameters important to the dynamic response of unround wheels have been established. To get a full understanding of the influence of all important vehicle and track parameters, a sensitivity analysis is performed with the base model as the foundation, the results of which are shown in Figure 5-12. The maximum acceleration values $\ddot{z}_{max}$ are shown as a function of each parameter. As it can be clearly seen, the order n and radius deviation amplitude ΔR_0 of the polygonization, as well as the track parameters, the vehicle speed v, the wheel radius R and the unsprung mass of the vehicle $m_{unsprung}$ have the greatest effects on the maximum acceleration of the wheelset $\ddot{z}$. The influence of the primary and secondary suspension stiffnesses $c_{z,prim}$ and $c_{z,sec}$ and the axle load m_{axle}, as well as the contact reference damping d_{ref} for the wheel-rail contact can be neglected.

The following investigations deal with the most influential parameters in more detail. Because the speed v is the only parameter that continuously changes for every vehicle and the effects behave strongly nonlinear with the vehicle speed v, as can be clearly seen in Figure 5-11 and Figure 5-12, all variations of the other parameters will be performed over a speed range. What is also noted is a very strong effect by all parameters that influence the P2-resonance frequency, more information on this is given later in this section.

5.2.2.2 Influence of the Polygonization Parameters

First, the effect of the order of the polygonization n is investigated. Figure 5-13 shows how the peak in the maximum acceleration amplitudes $\ddot{z}_{max}$ change with vehicle speed v for different polygon orders n. As the polygon order n rises, a smaller speed v is necessary to achieve an excitation of the track at the P2-resonance frequency. It is interesting to note that for orders 2 to 9, the peak value $\ddot{z}_{peak}$ of the maximum accelerations $\ddot{z}_{max}$ for each order almost does not depend on the order, in contrast to the analytical investigations in chapter 5.2.1.

For very high speeds v and high polygon orders n, the excitation frequency f_{exc} becomes very large and the track eventually cannot overcome its inertia quickly enough to move upward and accommodate the sudden radius decline, which leads to loss of contact.

If both the wheelset cannot reach the required downward acceleration and the track cannot accelerate upwards quickly enough, loss of contact occurs. Loss of contact leads to very high forces Q and accelerations $\ddot{z}$ when the contact is reestablished. For this set of model parameters, loss of contact occurred at v = 150 km/h for a 12th-order polygon and at v = 160 km/h for a 11th- and 12th-order polygon and can be identified by the high acceleration values of the corresponding curves in Figure 5-13.

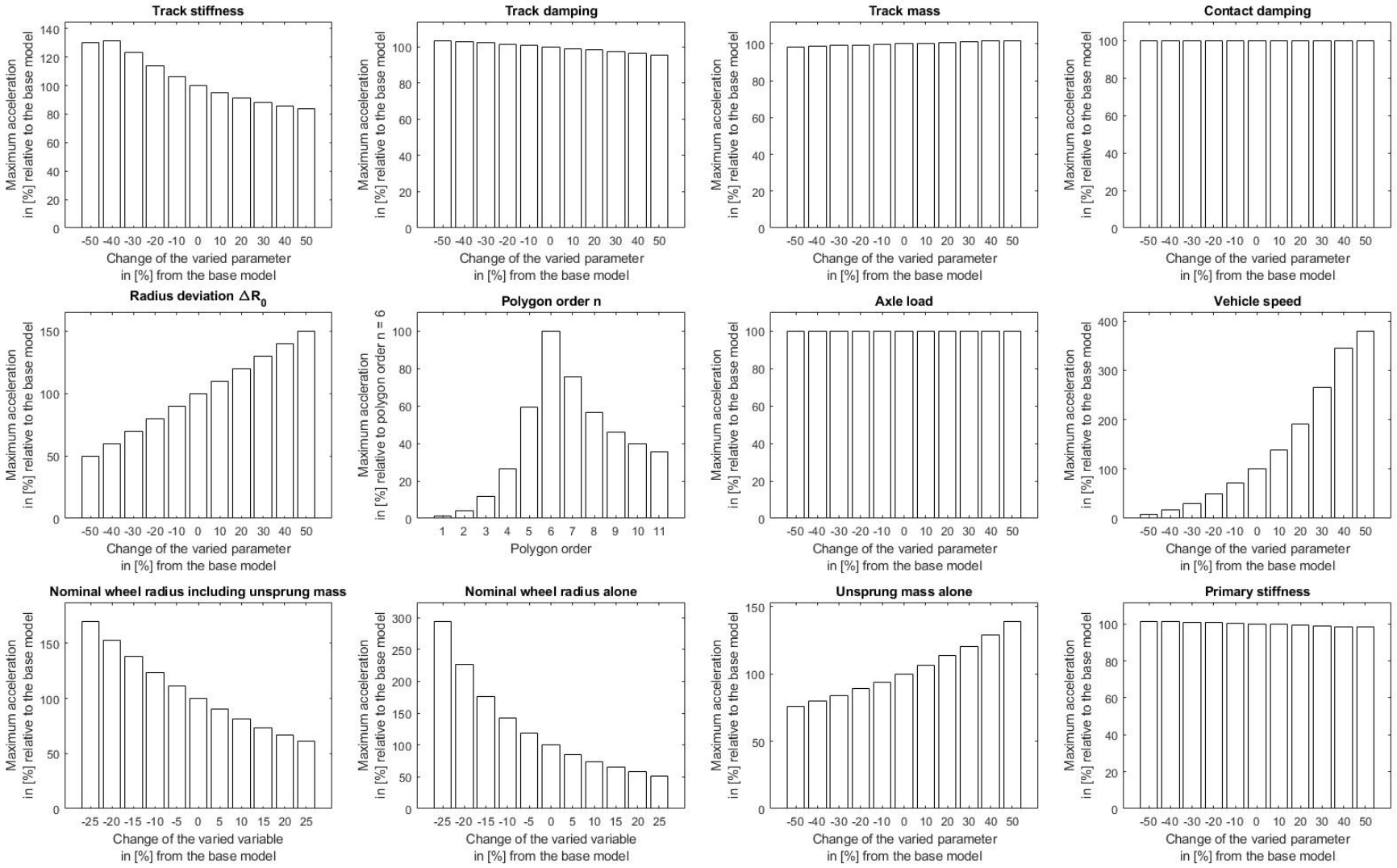

Figure 5-12 - Sensitivity analysis to find out the influence of each parameter on the maximum wheelset acceleration. Relative changes are given with respect to the base model, if not otherwise specified in each graph.

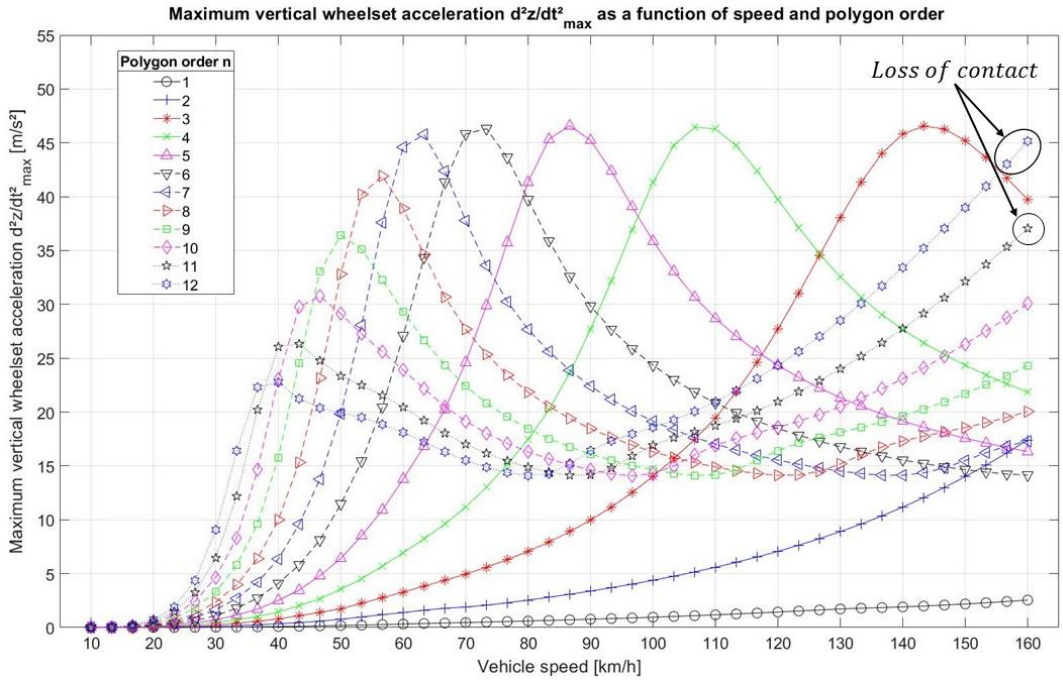

Figure 5-13 - A peak in the maximum wheelset accelerations can be observed at different vehicle speeds v for different polygon orders n. Polygon amplitude ΔR_0 simulated was ΔR_0 = 0.25 mm.

As for the peaks in the maximum accelerations $\ddot{z}_{peak}$ resulting from the P2-resonance, if the goal is the limitation of axle box accelerations $\ddot{z}$, the vehicle should be operated at a speed v that is sufficiently far away from the speed where the peak in the maximum accelerations $\ddot{z}_{max}$ occurs. This speed v is different for every polygon order n. If the vehicle is mainly operated within a certain speed range, polygon orders n for which the peak occurs in this speed range should be avoided to limit the resulting accelerations $\ddot{z}$. According to [3], typical values for the P2-resonance lie around 50-100 Hz.

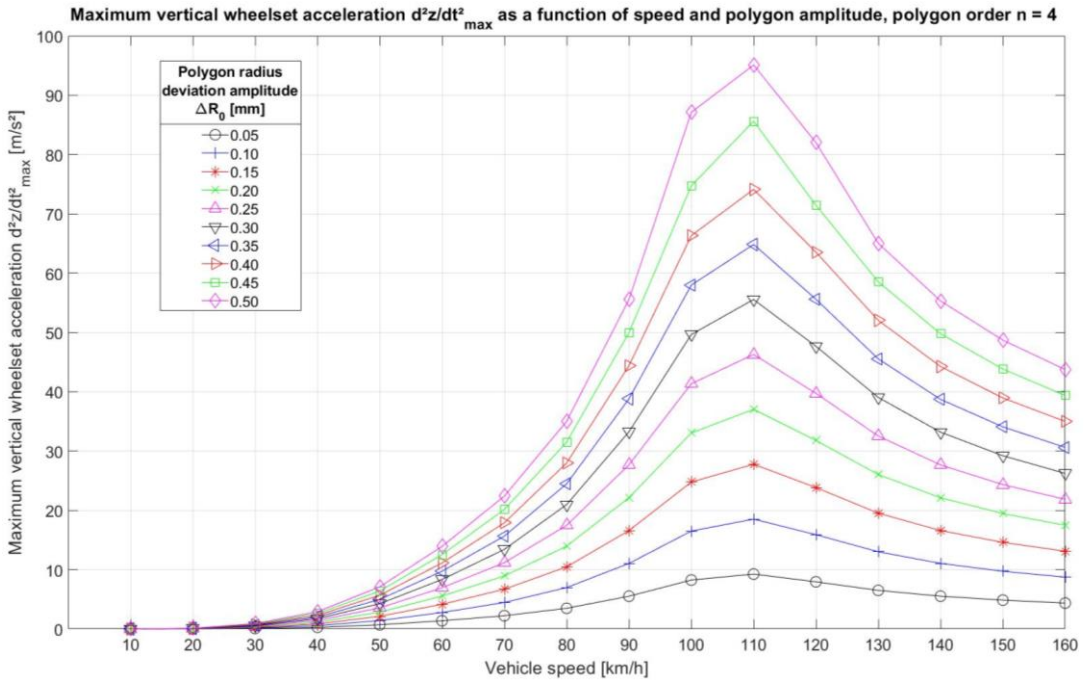

Figure 5-14 - A peak in the maximum wheelset accelerations can be observed at the same vehicle speeds for different polygon amplitudes. Polygon order n simulated was n = 4.

This means that for a polygon of order n, the speed v_{crit} where the peak of the maximum vertical acceleration occurs can differ by up to a factor of two, depending only on the track properties, making it even more difficult to find a general limit for maximum radius deviations ΔR_0 that takes the polygon order n into consideration. Considering a variation of the radius deviation amplitude ΔR_0 of the polygonization, no change in the characteristics in the speed domain can be observed, as shown in Figure 5-14. The maximum acceleration amplitudes $\ddot{z}_{max}$ scale almost perfectly linearly with the amplitude of the radius deviation ΔR_0.

5.2.2.3 Influence of the Track Properties

So far, only parameters of the polygonization (i.e. order n and amplitude ΔR_0) and the vehicle speed have been considered. Since the acceleration response of the wheelset is strongly influenced by the P2-resonance frequency, the influence of a variation of the track stiffness will be analyzed. The P2-resonance frequency is not only a function of the track properties, but also depends strongly on the unsprung vehicle mass. A simplified model to replicate the P2-resonance is a one-mass spring damper with the track stiffness and sum of the vehicle unsprung mass m_w and active track mass m_t, for which the wheel-rail contact is considered infinitely stiff, as shown in Figure 5-15.

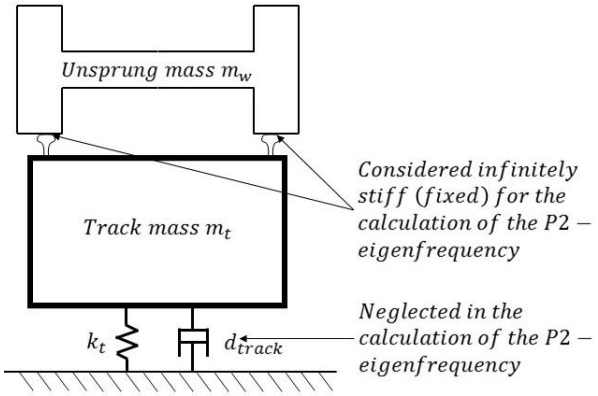

Figure 5-15 - Simplification of the track and wheel-rail contact model to approximate the P2-frequency.

In [82], this fact is used to derive the mathematical term in Equation 5-10 for the P2-resonance. As already stated, the contact stiffness in the wheel-rail contact is considered as infinite for this simplification, the effect of it is very small because it is an order of magnitude larger than the track stiffness and the track damping is neglected. The P2-resonance frequency f_{P2} varies with the root of the track stiffness k_t.

$$f_{P2} = \sqrt{\frac{k_t}{m_w + m_t}} \cdot \frac{1}{2\pi} \qquad \text{Equation 5-10}$$

For the base model, a value of 41.1 Hz is obtained for f_{P2}, which corresponds well to the value calculated in the eigenmode analysis within *SIMPACK* for the linearized model, which is 40.3 Hz, as mentioned before. The slight difference can be attributed to the neglected damping of the track model as well as the stiffness of the wheel rail contact, which are both considered in the numerical analysis, but not in the simplified model for the analytical calculation of the P2-resonance frequency. Figure 5-16 shows how the maximum acceleration amplitudes $\ddot{z}_{max}$ change with varying track stiffness k_t in the speed domain. For a comparison, Table 2 shows analytically calculated values of the P2-eigenfrequency as well as the vehicle speed v at which

the excitation frequency f_{exc} corresponds to the analytically calculated P2-frequency for the base model. The vehicle speeds v from Table 2 are also marked on the abscissa in Figure 5-16. The correlations are complex, since the change does not only affect the position of the peak, but also the peak magnitude.

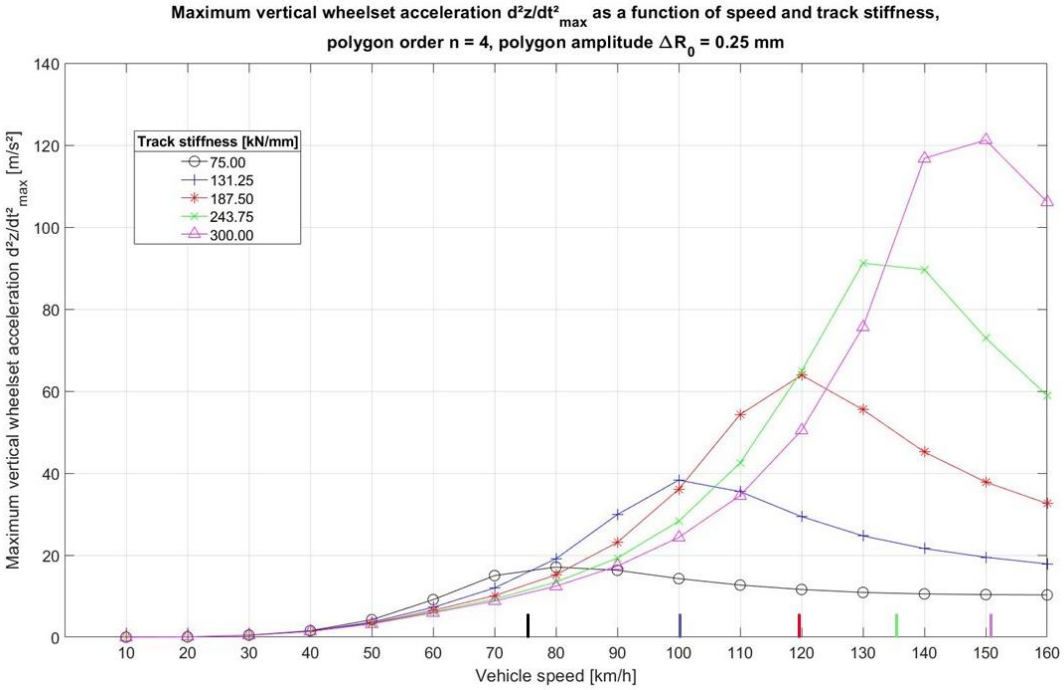

Figure 5-16 - The maximum acceleration peak position and the peak value both shift with changing track stiffness k_t. The calculation was performed using a fourth-order polygon with an amplitude of ΔR_0 = 0.25 mm.

Table 2 - P2-frequencies and vehicle speeds that lead to excitation frequencies corresponding to the P2-frequencies are shown for different values of the track stiffness, with a polygon order n of 4.

Track stiffness [kN/mm]	**P2-frequency [Hz], analytically calculated**	**Vehicle speed v [km/h] at which the excitation frequency corresponds to the P2-frequency**
75.00	29.09	75.68
131.25	38.49	100.11
187.50	46.00	119.65
243.75	52.45	136.43
300.00	58.18	151.35

As expected, the peak position does approximately change with the square root of the track stiffness k_t. The peak maximum acceleration amplitudes $\ddot{z}_{peak}$ behave almost perfectly linear with a change of the track stiffness k_t. Fitting the data by linear regression, the root mean square of the errors of the fitted curve amounts to $RMSE_{linear\ fit}$ = 2.02 m/s², making the relationship between track stiffness k_t and peak acceleration value $\ddot{z}_{peak}$ a simple one. The linear relationship is clearly visible in Figure 5-17. The track properties are not only determined by the track stiffness k_t, but also by the track mass m_t considered in the simulation. Varying the track mass within a representative range, Figure 5-18 is obtained. As can be expected from looking at Equation 5-10, the track mass influences the speed at which the peak maximum acceleration $\ddot{z}_{peak}$ occurs, albeit the effect is not as large as that of the track stiffness k_t. This is due to the fact that the unsprung vehicle

mass m_w is rather high in comparison to the track mass m_t, and the sum of the two determines the P2-resonance frequency.

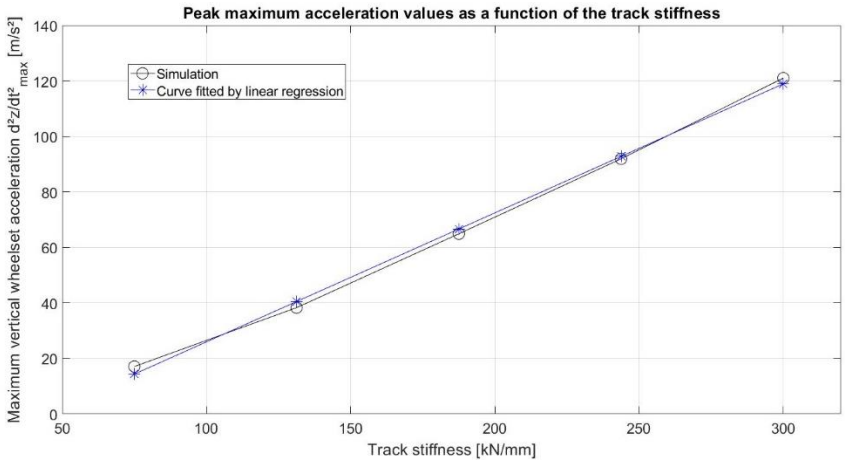

Figure 5-17 - Peak maximum acceleration values as a function of the track stiffness k_t, approximated by means of linear regression. The relationship is almost perfectly linear.

It is interesting to note that increasing the track mass m_t has the inverse effect of increasing the track stiffness k_t. To compare the analytical track model to the numerical track model, Table 3 shows analytically calculated values of the P2-eigenfrequency as well as the vehicle speed v at which the excitation frequency f_{exc} corresponds to the analytically calculated P2-frequency for the base model for different track masses m_t.

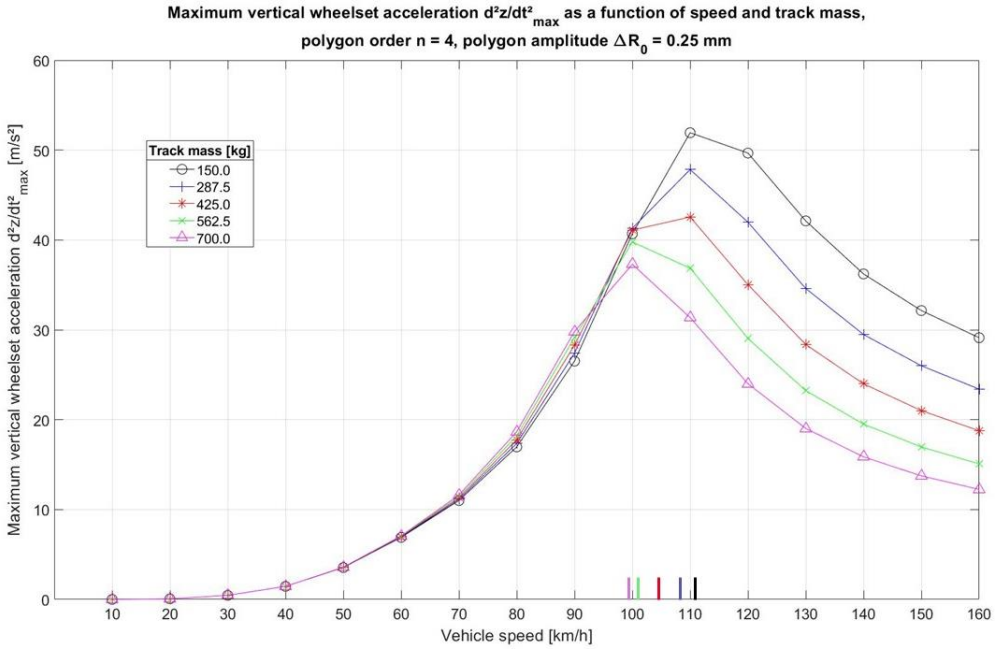

Figure 5-18 - The maximum acceleration peak position and value both shift with changing track mass. The calculation was performed using a fourth-order polygon with an amplitude of ΔR_0 = 0.25 mm.

The same effect that is achieved by changing the track mass m_t can also be achieved by changing the unsprung mass of the vehicle m_w, since variations in both masses change the total effective mass in Equation 5-10, altering the P2-resonance frequency, as shown in Table 3. The influence of the unsprung mass m_w is higher in general, since it is higher than usual track masses m_t.

Table 3 - P2-frequencies and vehicle speeds that lead to excitation frequencies corresponding to the P2-frequencies are shown for different values of the track masses, polygon order n used was 4.

Track mass [kg]	P2-frequency [Hz], analytically calculated	Vehicle speed v [km/h] at which the excitation frequency corresponds to the P2-frequency
150.00	42.90	111.59
287.50	41.54	108.05
425.00	40.30	104.83
562.50	39.16	101.88
700.00	38.12	99.16

However, an increase of the maximum accelerations $\ddot{z}_{max}$ with the unsprung mass m_w, like in Figure 5-12, is not a general rule. This is just a consequence of the parameters chosen for the base model. Sets of parameters also exist for which increasing the unsprung mass m_w leads to lower maximum accelerations $\ddot{z}_{max}$. If a set of parameters were chosen, for which increasing the unsprung mass m_w would bring the P2-resonance frequency f_{P2} further away from the excitation frequency f_{exc}, a decline in acceleration levels with increasing unsprung mass could be observed.

5.2.2.4 Influence of Vehicle Parameters

If all other parameters are fixed, changing only the wheel radius (without changing the unsprung mass) influences the time t taken for one wheel revolution. This means that the wheel rotation frequency ω is changed, changing the excitation frequency f_{exc}. If increasing the wheel radius R brings the excitation frequency f_{exc}, which corresponds to the product of the wheel rotation frequency ω and the polygon order n, closer to the P2-resonance frequency f_{P2}, the acceleration levels rise. If the opposite is the case, acceleration levels drop. Since the wheel radius R and unsprung mass m_w are never completely unrelated, the combination of both is varied, as explained in chapter 5.1.2. The results of this variation are shown in Figure 5-19.

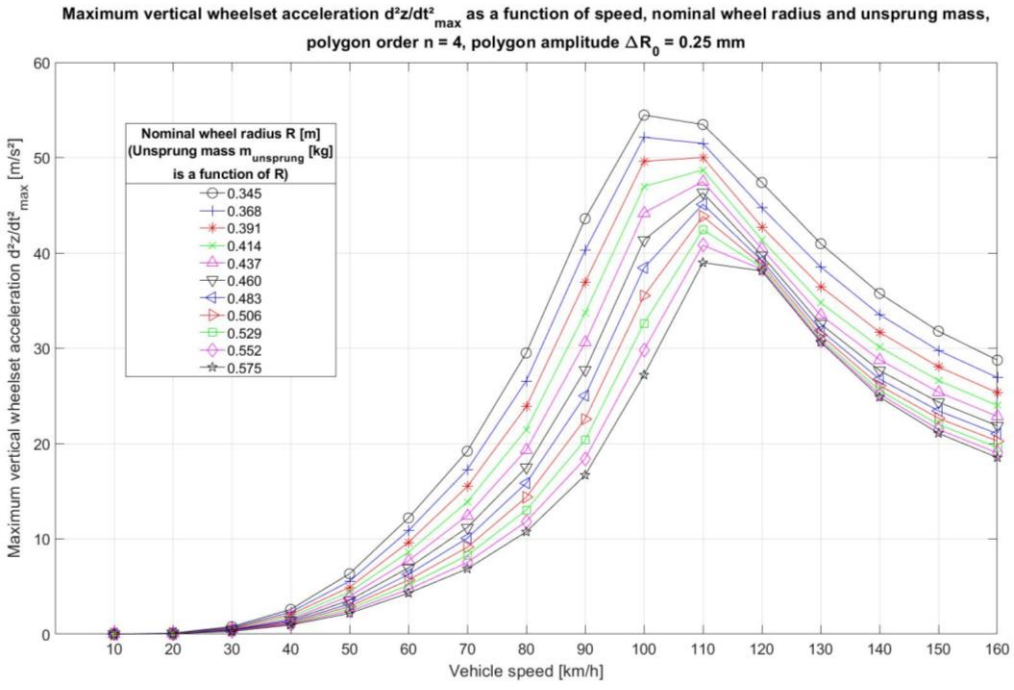

Figure 5-19 - The maximum accelerations as a function of vehicle speed, nominal wheel radius and unsprung mass, which is in turn a function of the nominal wheel radius.

Changing the wheel radius R, together with the unsprung mass m_w, does not have a definitive effect on the general acceleration levels $\ddot{z}$. The effect also depends on all other parameters that influence the P2-resonance frequency and the excitation frequency achieved by the polygonization.

The influences of the most important parameters have been shown in this section. A final interpretation of the obtained results is carried out in chapter 6.1.

5.3 Flats and Other Types of Discrete Defects

Flats and other types of discrete defects are restricted by EN15313 by limiting their maximum visible geometric sizes l, as shown in Figure 1-4. For newly formed flats, these should correspond to their actual lengths l. After a certain mileage, however, flats may become subject to plastic deformation around their edges. This effectively "lengthens" the flat, but this change can often not be detected with the naked eye.

The main goal of this section is to find out whether a simple correlation between the axle box accelerations $\ddot{z}$ that a flat induces and the flat length l exists, taking into account all known parameters of the vehicle-track system. A subgoal is to check whether the length limits in EN15313 are sensible from the point of view of dynamic loads, namely vertical accelerations $\ddot{z}$.

As described in chapter 5.1.4, the radius deviation function $\Delta R(\beta)$ used for the numeric analysis of flats is not the actual radius deviation as a function of the circumference angle β, but the kinematic trajectory that the wheel follows as it rolls over the flat with an infinitesimally small speed. This radius deviation function $\Delta R(\beta)$ can simply be derived for a newly formed flat of length l on a wheel with a nominal wheel radius R, φ_0 being half the angle of the flat spot on the circumference, see Figure 5-20 (a) for reference. For most of the circumference angle, the radius deviation $\Delta R(\beta)$ is zero. As the wheel rolls, the first edge of the flat is reached. When this happens, the wheel tilts around the edge and the wheel center follows a circular trajectory, until the surface of the flat hits the rail. From this moment on, the same process occurs in reverse and the wheel tilts around the second edge of the flat. The whole process is shown in Figure 5-20 (b). Flats, which are not ideal, are considered as well. To model such flats, the depth d is scaled with a factor smaller than one. The actual radius deviation of the wheel as a function of the circumference angle β is scaled with this factor, resulting in a flat that is

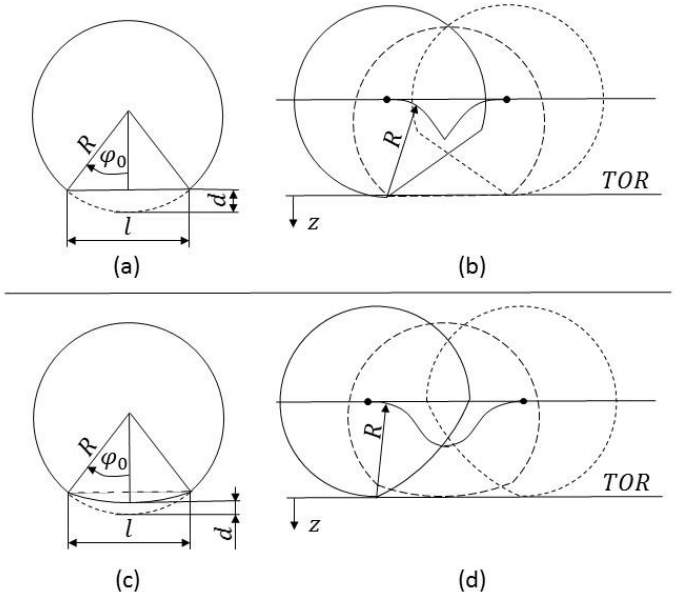

Figure 5-20 – (a) Dimensions on a flat. (b) Deriving the kinematic trajectory of a flat. (c) Dimensions of an imperfect flat. (d) Deriving the kinematic trajectory of an imperfect flat.

shown in Figure 5-20 (c). The radius deviation function $\Delta R(\beta)$ used to apply the unroundness in the numerical calculations is also the kinematic trajectory of the wheel. In the case of flats that are not ideal, the shape differs from that of an ideal flat and is shown in Figure 5-20 (d). It is derived numerically, using *MATLAB*.

For ideal flats, the trajectory during the tilting process is circular, and the position of the wheel center in the z-direction can be written as follows, where β_1 is the wheel rotation angle at which the radius to the first edge of the flat is vertical, β_2 is the wheel rotation angle at which the radius to the second edge of the flat is vertical, β_f is the wheel rotation angle at which the flat surface touches the rail and β is the current wheel rotation angle. The angles are shown in Figure 5-21.

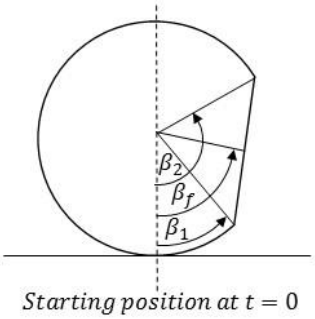

Figure 5-21 - Definition of the angles for Equation 5-11.

$$z(\beta) = \begin{cases} 0, & \beta < \beta_1 \\ R \cdot \cos(\beta - \beta_1), & \beta_1 \leq \beta < \beta_f \\ R \cdot \cos(\beta_2 - \beta), & \beta_f \leq \beta < \beta_2 \\ 0, & \beta \geq \beta_2 \end{cases} \qquad \text{Equation 5-11}$$

The function in Equation 5-11 corresponds to the radius deviation function $\Delta R(\beta)$ for the complete wheel and looks as shown in Figure 5-22. In *SIMPACK*, the method used for providing the software with data about the unroundness is the input via pointwise coordinates [10], the wheel rotation angle β being the independent and the radius deviation $\Delta R(\beta)$ being the dependent coordinate. For interpolation between the points provided to *SIMPACK*, the software uses cubic splines. The radius deviation $\Delta R(\beta)$ function is evaluated at some grid points and the coordinates are given to the simulation software.

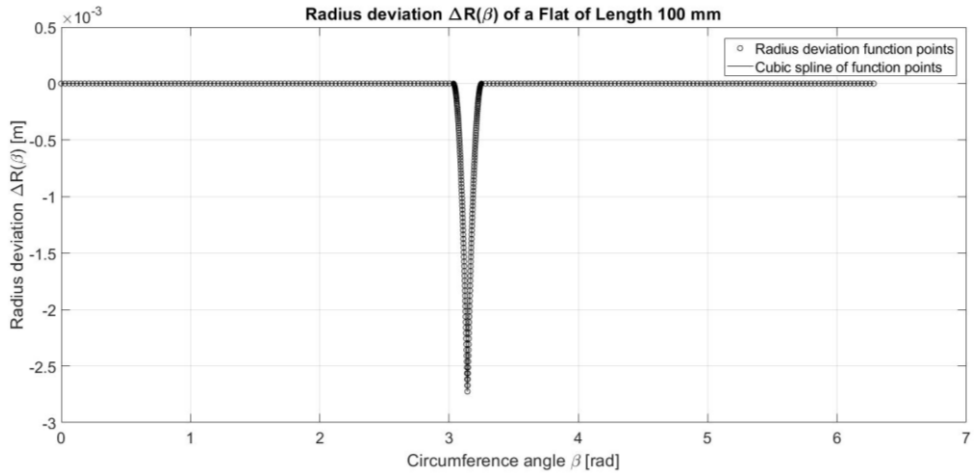

Figure 5-22 - Theoretical trajectory of a wheel with a nominal diameter of D = 920 mm and a flat of length l = 100 mm, used as radius deviation function.

5.3.1 Analytical Approach

The wheel trajectory function $z(\beta)$ is not differentiable at the angle β_f, which can be shown by evaluating the sign of the left and right side limits of the difference quotient, which is done in Equation 5-12 and Equation 5-13.

$$\lim_{\beta \to \beta_f^+} \frac{\Delta R(\beta) - \Delta R(\beta_f)}{\beta - \beta_f} > 0 \qquad \text{Equation 5-12}$$

$$\lim_{\beta \to \beta_f^-} \frac{\Delta R(\beta) - \Delta R(\beta_f)}{\beta - \beta_f} < 0 \qquad \text{Equation 5-13}$$

The lack of differentiability is the reason why the acceleration $\ddot{z}(\beta)$ as a function of the wheel rotation angle β resulting from the kinematic trajectory $z(\beta)$ of the flat cannot simply be calculated by differentiation of the trajectory. Differentiation of the wheel trajectory $z(\beta)$ leads to the theoretical vertical velocity $\dot{z}(\beta)$ of the wheel. It contains a step because the slope of the trajectory is not unambiguous at the time when the wheel is at the lowermost position. Differentiating further, a step yields an infinite slope, meaning that the acceleration $\ddot{z}(\beta)$ becomes infinite for an infinitesimally short amount of time, constituting a Dirac-impulse. In Figure 5-23, the qualitative kinematic vertical position $z(\beta)$, velocity $\dot{z}(\beta)$ and acceleration $\ddot{z}(\beta)$ are shown. Obviously, an infinite acceleration cannot occur. In [19], efforts have been made to avoid the lack of differentiability by applying a curvature to the flat part of a flat. This, however, introduces a new unknown quantity, which is the curvature that is applied. Another restriction of the analytical approach is the fact that loss of contact cannot be accounted for. A numerical model that can account for loss of contact, track and wheel-rail contact stiffness c_h is used for further investigations.

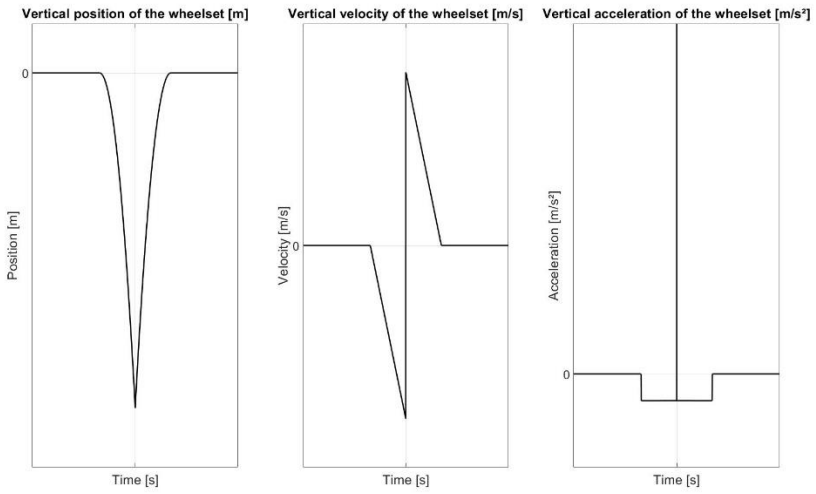

Figure 5-23 - Qualitative kinematic vertical position, velocity and acceleration of a wheel with a flat. The acceleration peak is of infinite magnitude and infinitesimally short duration.

5.3.2 Numerical Analysis

The singularity in the radius deviation function $\Delta R(\beta)$, which is explained in chapter 5.3.1, does not play a role in numerical simulations, because only the radius deviation function itself is evaluated, and no derivatives of the function. Pointwise coordinates are provided to the software and are splined to attain the radius deviation function $\Delta R(\beta)$ that is applied during

the simulation. A sufficiently large number of grid points needs to be provided to avoid overshooting, which can be seen in the right-hand graph of Figure 5-24.

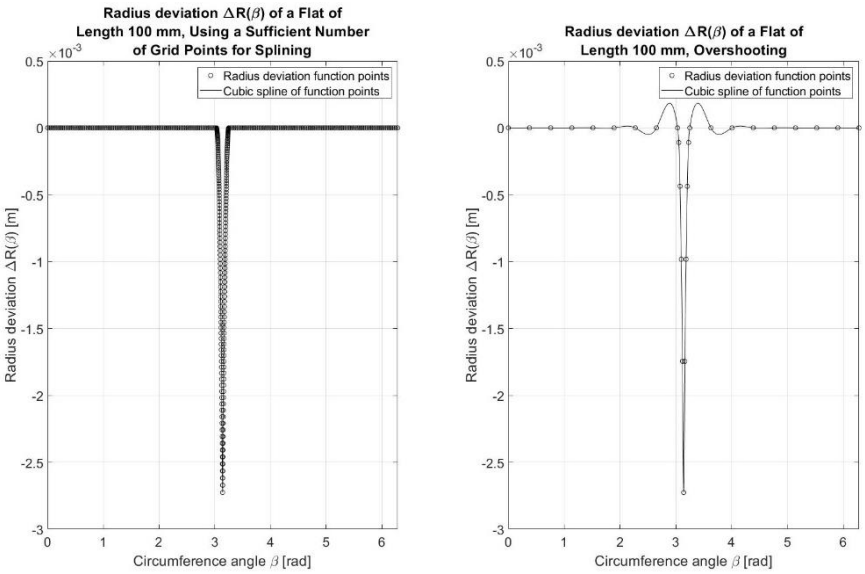

Figure 5-24 - Difference between splining a function using a sufficient number of grid points and too few grid points. If the number of grind points is too small, overshooting occurs (right-hand graph).

For all numerical investigations, the base model with the base parametrization and the base two-mass track model as described in chapters 5.1.2 and 5.1.3 is used, and all relative changes of the parameters are with respect to the base model. Only for validation, the parameters are modified to correspond with the parameters of the vehicle where the measurements were performed on. To verify that the numerical simulation provides realistic results and, thus, validate the model, axle box acceleration measurements from a commuter train with a flat of a known (visual) length l are compared against simulations with a flat of the same length.

5.3.2.1 Implementation of a Flexible Wheelset Model

A flexible wheelset is implemented into the base model to try to enable the simulation to reproduce the axle box acceleration measurements, which might contain the first bending eigenfrequency of the wheelset. The flexible wheelset is modeled using a one-dimensional Euler-Bernoulli beam. The simplified Euler-Bernoulli beam theory allows a quick and easy calculation of structural deformations, more explicitly, bending. The diameter of the simulated axle corresponds to the wheelset axle diameter of the vehicle that the axle box accelerations were measured on, which is 0.205 m. Two large, rigid masses that are visible in Figure 5-25 represent the influence of the wheel discs and all additional masses, including the gearbox that is connected to the wheelset. Only the axle between the wheel discs is modeled as flexible, the rest of the wheelset is modeled as rigid masses. The whole wheelset mass corresponds to the actual unsprung mass m_w of the vehicle where the axle box measurements were performed on for the validation model. For the base model, the whole wheelset mass m_w is linearly dependent on the wheel radius R and follows the law given in Equation 5-1 in chapter 5.1.2. The positions of the additional masses along the length of the beam are chosen so that the measured wheelset bending eigenfrequency of 110 Hz from chapter 4.2.1 is reproduced for a built-in wheelset.

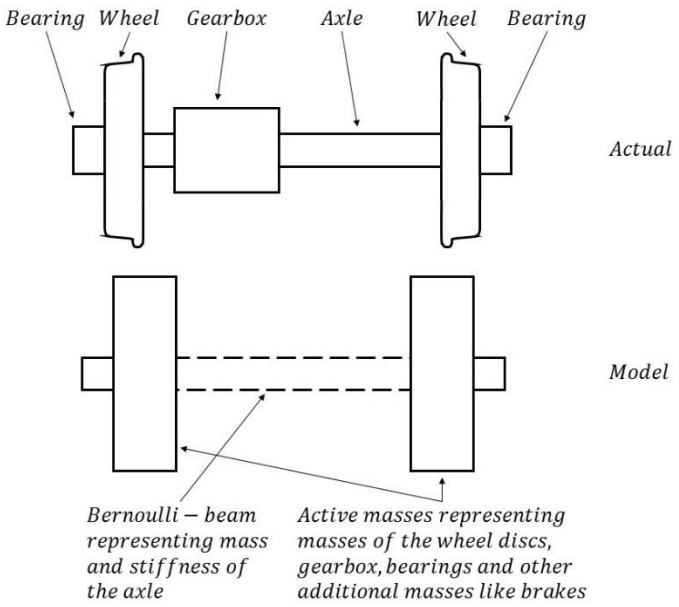

Figure 5-25 - Visual representation of the actual wheelset topology on top, and the model abstraction used to represent the elastic wheelset on the bottom of the Figure.

As can be seen in Figure 5-25, the rigid masses representing the wheel discs and additional masses are positioned closer to the center of the wheelset than the actual wheel discs. This is because they also represent all other additional masses, i.e. the gearbox, which is positioned closer to the center of the wheelset.

For comparison with the measured data, simulations are performed with model parameters that match the parameters of the vehicle where the axle box accelerations were measured on. The measurements are examined in chapter 4.2. The flat, which is investigated, has a length l of 12.4 mm (compare chapter 4.2), the radius deviation function $\Delta R(\beta)$ has been chosen according to the one in Figure 5-22. A two-mass track model with adjusted parameter values, as denoted in Table A-7, is used in order to obtain simulation results that match the measurements. A comparison of the results of the numerical calculation with the measurements is conducted in chapter 6.2.

5.3.2.2 Sensitivity Analysis

To study the influence of the system parameters on the axle box accelerations $\ddot{z}$ and get a general understanding of the most influential factors, a sensitivity analysis is performed, starting from the base model. For all further investigations, the base model is used. All calculations are performed in the time-domain over a timespan t which includes at least ten flat impacts, an example for a resulting calculation result of the axle box accelerations is shown in Figure 5-26. Out of each time integration, only the maximum absolute acceleration value is used, which is indicated in Figure 5-26. Negative values are also considered, and the absolute value is taken. The results of the sensitivity analysis can be seen in Figure 5-27, which shows how the absolute maximum acceleration values $\ddot{z}_{max}$ change with varying vehicle, track and flat parameters. Each parameter was varied within a representative range, which is the reason for different relative changes of each investigated parameter with respect to the base model.

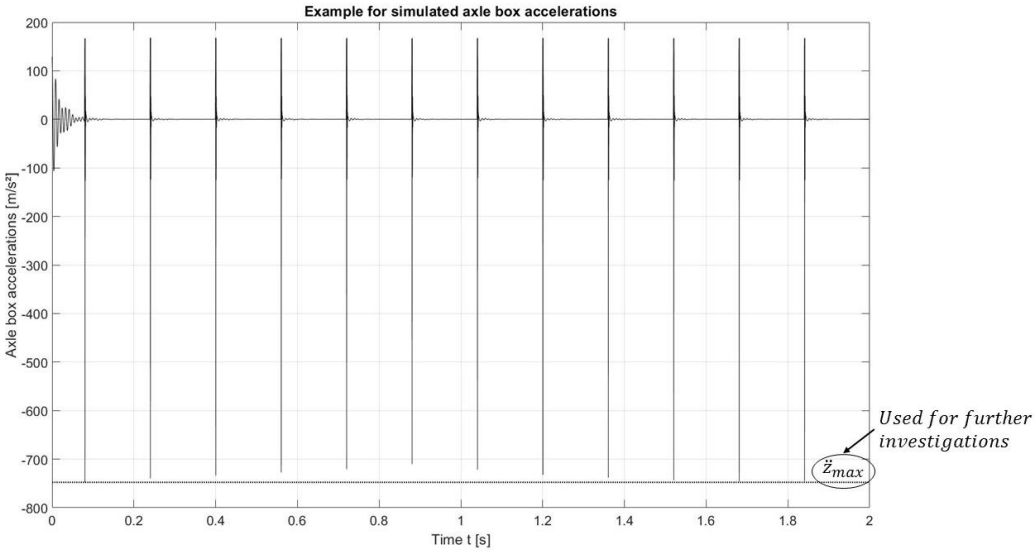

Figure 5-26 - Example for calculation results of the axle box accelerations.

This subsequently leads to differently scaled x-axes in Figure 5-27. The following findings can be reported as a result of the sensitivity analysis.

- The vehicle speed dependency of the maximum accelerations $\ddot{z}_{max}$ with a peak at a certain speed v_{crit} is reproduced well by the model.
- The parameters that determine the length limits l_{max} in EN15313 [2] (R, v_{max}, m_{axle}) have been determined as very influential in the sensitivity analysis.
- Other influential parameters have been determined to be the flat length l and depth d, the unsprung mass m_w, the track masses m_r and m_b and the contact reference damping d_{ref}.
- Less influential parameters are the rail pad and ballast stiffnesses c_r and c_b, the primary stiffness $c_{z,prim}$ and the secondary stiffness $c_{z,sec}$.

The contact damping d_{ref} has a relatively strong effect on the resulting acceleration values and a value for this parameter is very difficult to determine. Therefore, the standard value is used for all further analyses as it has proven to provide the most accurate results for the wheel-rail contact force calculation. It needs to be noted that the contact damping d_{eff} is a purely numerical quantity, and the strong influence on the resulting accelerations weakens the trust in the quantitative calculation results, because it can change the calculated maximum acceleration values $\ddot{z}_{max}$ by up to several percent. In the following section, the influence of single parameters is investigated in more detail. Since there is a very strong, nonlinear correlation between the vehicle speed v and the axle box accelerations $\ddot{z}$, and a maximum in the accelerations $\ddot{z}_{max}$ occurs at a specific vehicle speed v, called v_{crit}, all simulation results are shown over a speed range. Therefore, effects of parameters in the speed domain can also be investigated.

5.3.2.3 Influence of Flat Parameters

The first parameter investigated is the flat length l, which is one of the relevant parameters according to EN15313 [2]. Figure 5-28 shows how the absolute maximum acceleration values change with varying flat length l. Since the flat is modeled as ideally flat, the flat depth d also changes with varying flat length l as shown in Figure 5-30.

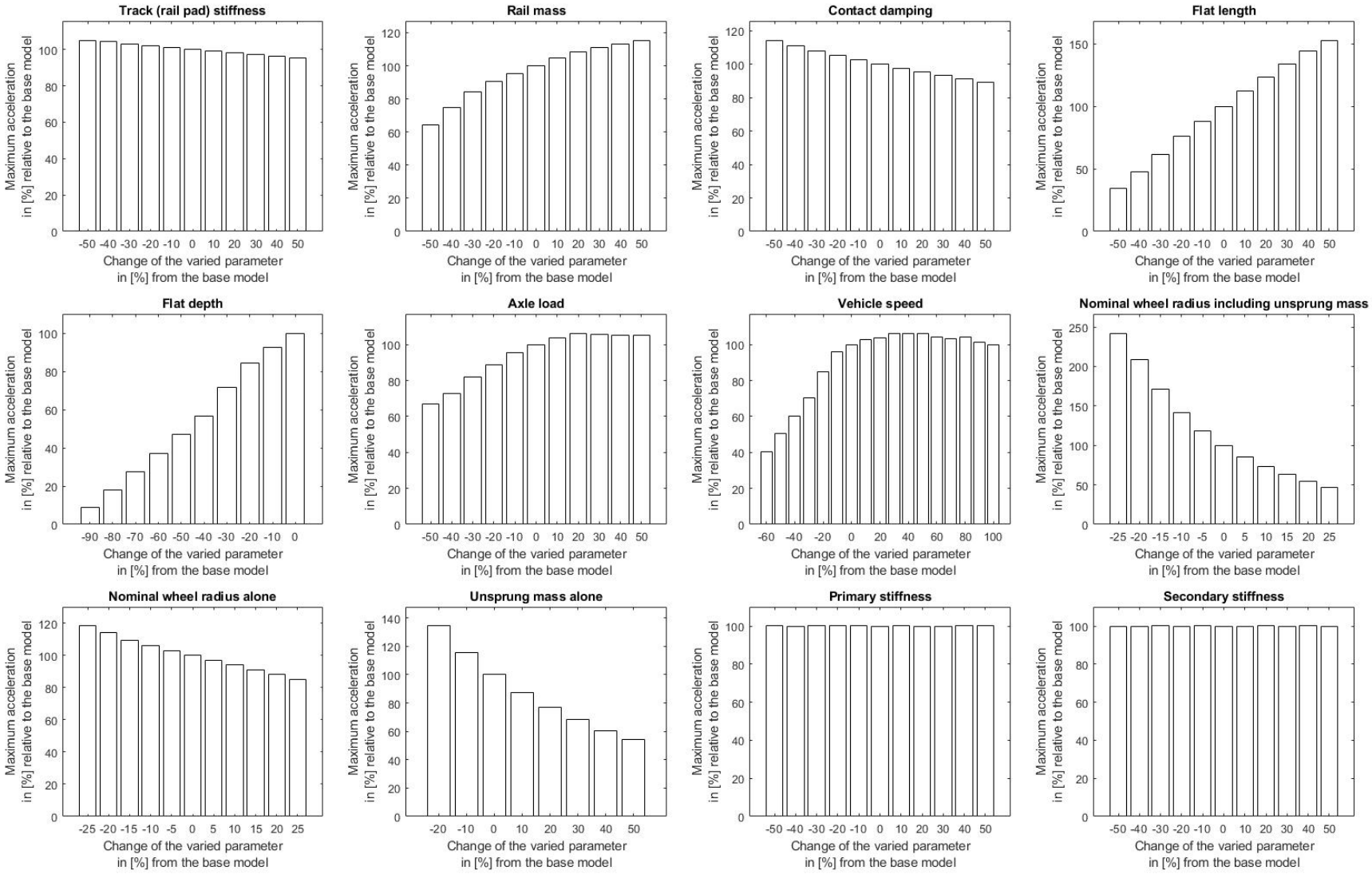

Figure 5-27 - Sensitivity analysis to find out the influence of each parameter on the maximum axle box accelerations. Relative changes are given with respect to the base model.

A monotonous increase is observed, similar to the relationship between the maximum acceleration values $\ddot{z}_{max}$ and the radius deviation amplitude ΔR_0 of a polygonized wheel from chapter 5.2.2, although in this case, the relationship is not linear.

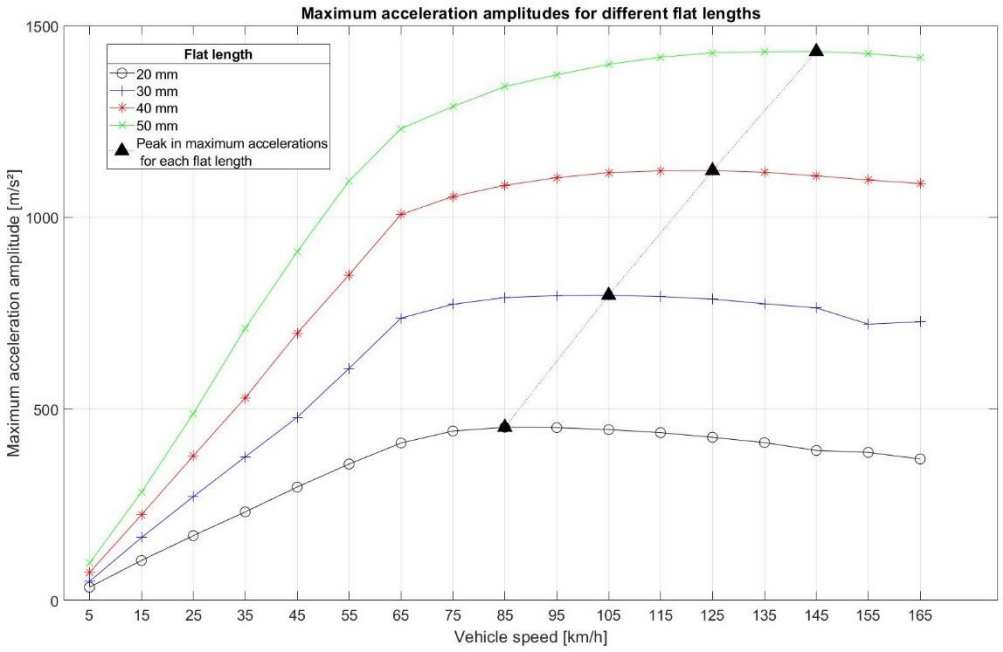

Figure 5-28 - Maximum acceleration amplitudes $\ddot{z}_{max}$ of ideal flats of different lengths l over a vehicle speed range. A shift of the peak in the curves can be observed for varying flat lengths.

It can also be observed that a shift of the peaks of the curves towards higher vehicle speeds occurs. This means that the vehicle speed v at which the peak maximum acceleration $\ddot{z}_{peak}$ occurs is different for different flat lengths l. Next, the length l of the flat is changed, keeping the depth d constant. The flats have a shape like shown in Figure 5-20 (c). The resulting absolute maximum acceleration values $\ddot{z}_{max}$ are shown in Figure 5-29.

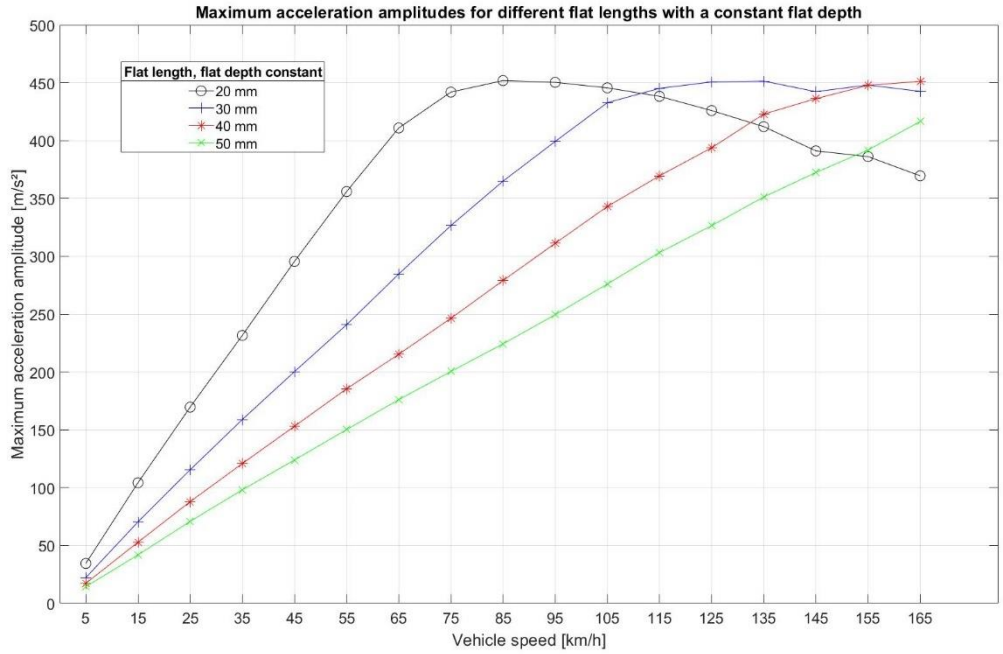

Figure 5-29 - Maximum acceleration amplitudes $\ddot{z}_{max}$ of imperfect flats of different lengths l with a constant flat depth d, which corresponds to the flat depth of a 20 mm flat, over a vehicle speed range.

For 40 mm and 50 mm long flats, no local peak in the maximum accelerations is found within the investigated speed range.

It is worth noting that the depth d of a flat has a far stronger effect on the maximum acceleration values than the length l. This may be explained by the fact that the maximum possible vertical displacement of the wheel z_{max} is determined by the depth of the flat and not by the length. The maximum possible vertical displacement z_{max} determines the maximum drop height and thus the maximum downwards velocity $\dot{z}$ that can be reached by the wheel, which has an influence on the deceleration $\ddot{z}$ when the downward motion of the wheel is stopped by contact between it and the rail. This becomes even clearer when the flat depth d is varied and the length l of the flat is kept constant, which was done to create Figure 5-31. The flats that are considered in this analysis have shapes like shown in Figure 5-30.

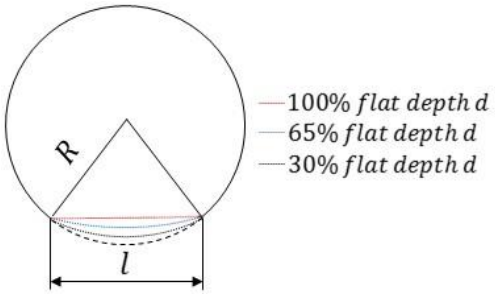

Figure 5-30 - Varying the flat depth d, while keeping the flat length l constant.

It is clear that the influence of the flat length l is of secondary importance for the values of the maximum accelerations $\ddot{z}_{max}$ that the axle box experiences.

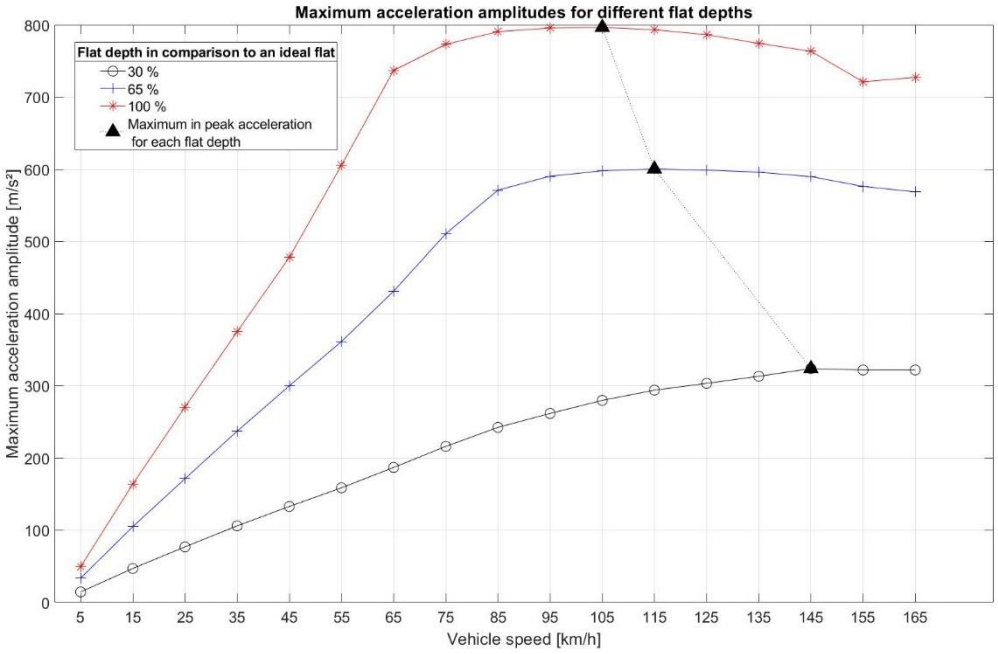

Figure 5-31 - Maximum acceleration amplitudes of a flat with a constant length of l = 30 mm. The depth was varied from the depth of an ideal flat to 30% of that depth.

5.3.2.4 Influence of the Track Properties

So far, only flat parameters (l, d) and the vehicle speed v have been investigated. Since the relative vertical velocity between the wheel and rail, $\dot{z}_{rel}$, have a major influence on the

resulting axle box accelerations $\ddot{z}$, the influence of the masses that represent the track is considered next. For the particular model used, the active track mass m_t is split into the rail mass m_r and the mass of the sleeper and ballast m_b, as shown in Figure 5-4 (b). Both the rail and the ballast extend very far in the running direction of the vehicle, but they are flexible, so their entire mass does not participate in oscillations induced by an out-of-round wheel. The active rail mass m_r used in the simulation represents the part of the mass of the rail that takes part in the oscillation. It has a large effect on the behavior of the absolute maximum accelerations $\ddot{z}_{max}$ in the speed domain, shifting the peak to lower vehicle speeds v. The mass representing the sleepers and ballast, called m_b, has very little effect on the resulting maximum accelerations $\ddot{z}_{max}$. Maximum acceleration values for different rail masses m_r used in the simulation are shown in Figure 5-32 as a function of vehicle speed v. The larger the active rail mass m_r, the longer the time t it takes for it to accelerate upwards during contact loss when the flat has entered the wheel-rail contact and the lower the maximum vertical velocity $\dot{z}_r$ it reaches during the short contact loss. The duration of contact loss becomes even shorter with rising vehicle speed v, allowing the rail mass even less time to reach a certain velocity $\dot{z}_r$.

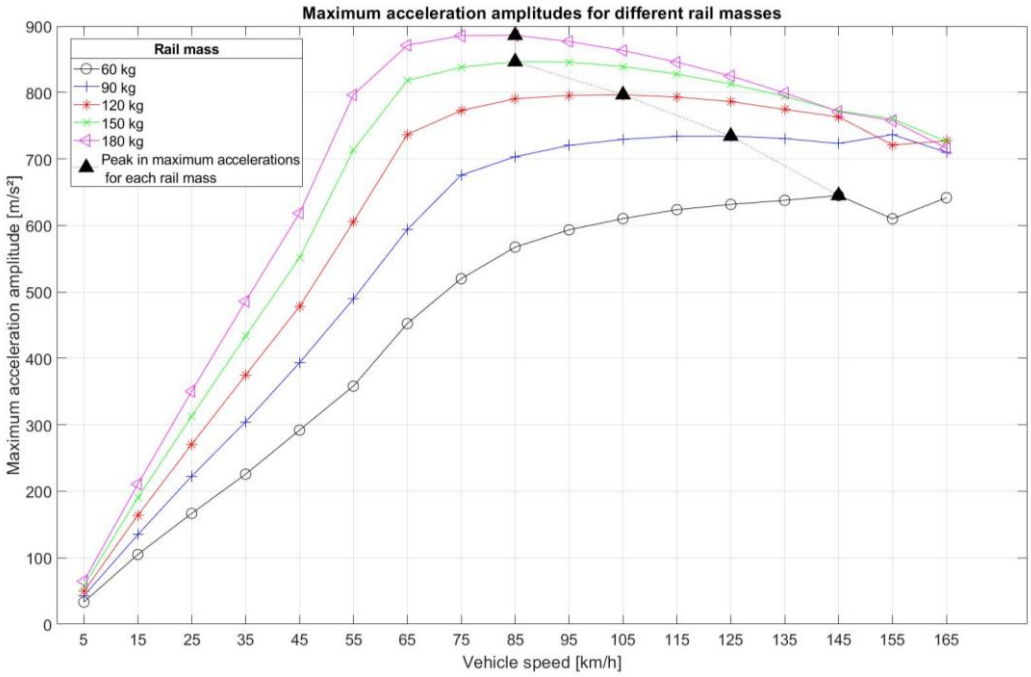

Figure 5-32 – Maximum acceleration values $\ddot{z}_{max}$ for different rail masses m_r considered in the simulation model.

This change in the dynamic characteristics of the track model leads to the shift of the peak of the maximum accelerations $\ddot{z}_{peak}$ to other vehicle speeds v. The stiffness values of the track, namely c_r and c_b, are not investigated in more detail, since they have a negligible effect on the axle box accelerations $\ddot{z}$, as it was found in the sensitivity analysis (see Figure 5-27).

5.3.2.5 Influence of the Vehicle Parameters

Many of the parameters of the vehicle itself have a significant influence on the observed axle box accelerations. Therefore, the influence of vehicle parameters is investigated next. Varying the nominal wheel radius R within a representative range yields Figure 5-34. It is worth noting that in Figure 5-34, only the influence of the wheel radius R is investigated, the unsprung mass

m_w is kept constant. With increasing wheel radius R, a flat of the same length l covers a smaller part of the circumference of the wheel and it does not reach the same depth d, as shown in Figure 5-33.

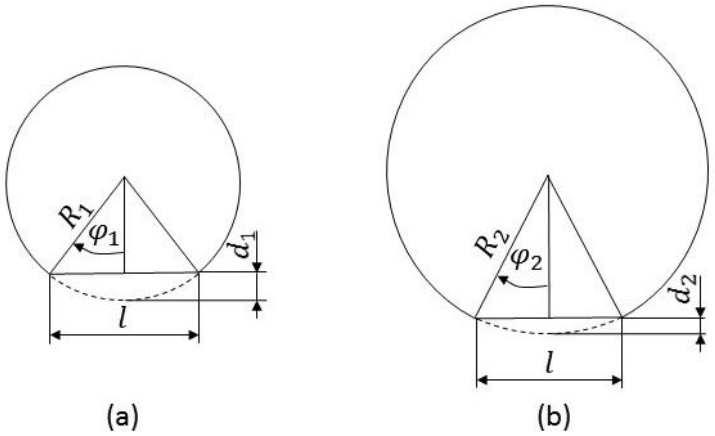

Figure 5-33 - (a) Perfect flat of length l on a wheel with radius R_1. (b) Perfect flat of the same length l, on a wheel with larger radius $R_2 > R_1$. Both the depth d_2 and circumference angle φ_2 of the wheel with the larger radius R_2 are smaller than d_1 and φ_1 for a flat of the same length l.

Since less of the circumference is covered by the flat, it is in the wheel-rail contact area for a shorter amount of time t, if the same vehicle speed v is assumed. As a result, the peak in the maximum accelerations $\ddot{z}_{peak}$ shifts in the speed domain and in magnitude with varying nominal wheel radius.

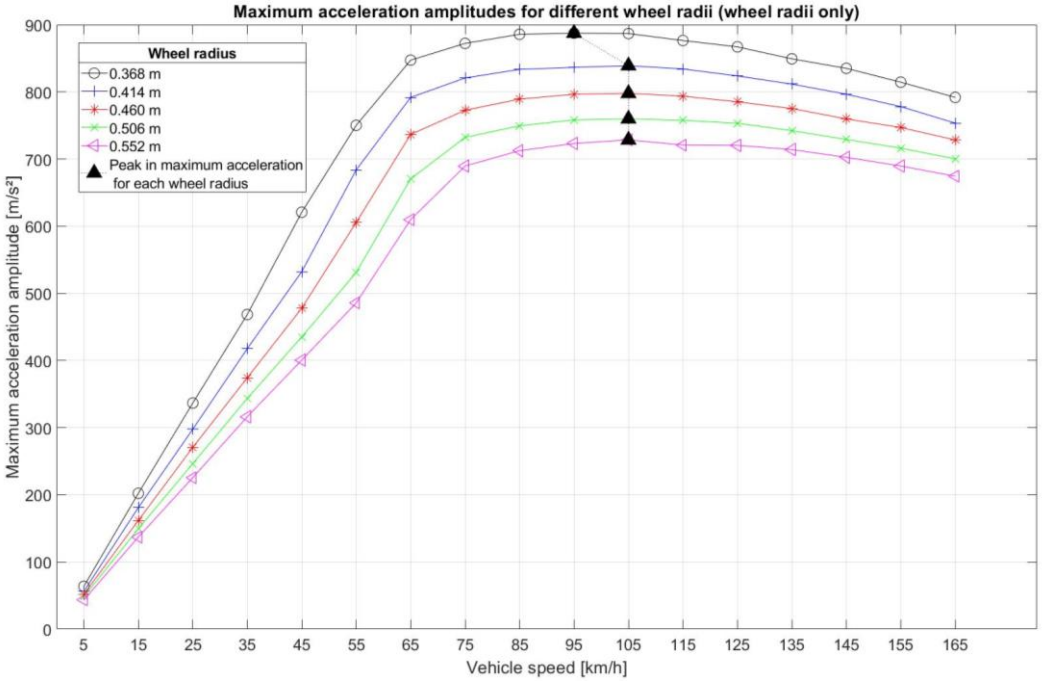

Figure 5-34 – Maximum acceleration values $\ddot{z}_{max}$ for different wheel radii R. In this case, the unsprung mass m_w was kept constant for all calculations.

The depth d of the flat also decreases with rising wheel radius R, and the maximum possible vertical displacement z_{max} of the wheel becomes smaller. As stated before, a change of the depth d leads to a change in the amplitudes of the maximum accelerations $\ddot{z}_{max}$, which can be seen in Figure 5-34.

Investigating the effects of the unsprung mass m_w, it is clearly visible from Figure 5-35 that a larger unsprung mass leads to smaller maximum axle box accelerations $\ddot{z}_{max}$. This seems unusual at first, as larger unsprung masses are usually connected to higher dynamic loads.

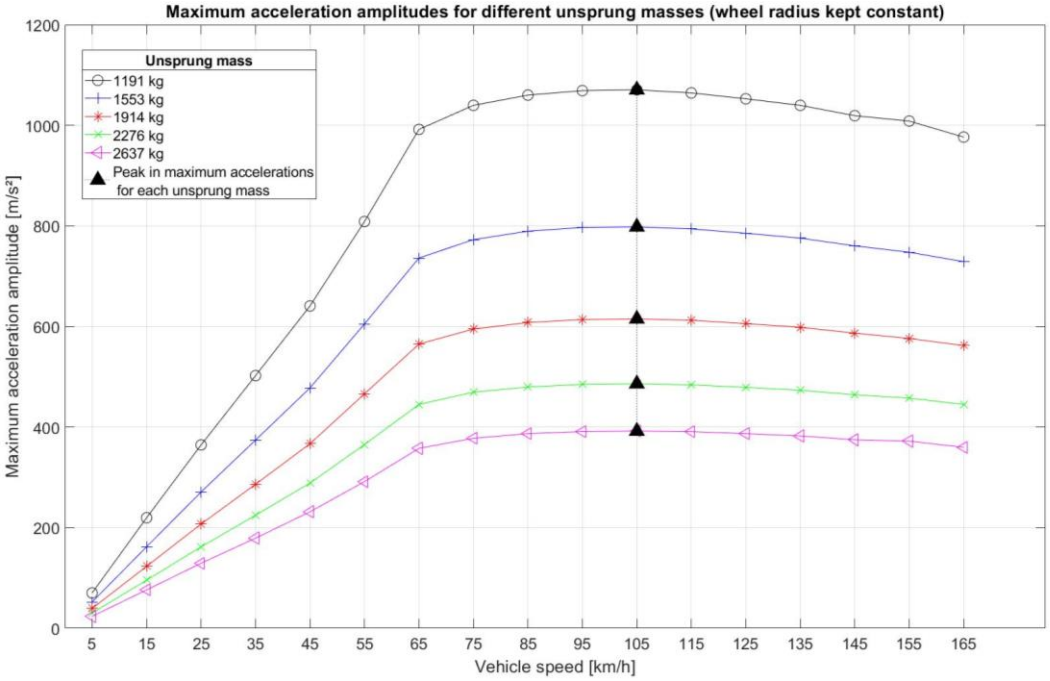

Figure 5-35 – Maximum acceleration values $\ddot{z}_{max}$ for different unsprung masses m_w. In this case, the wheel radius R was kept constant.

This effect can be observed because a higher unsprung mass m_w has more inertia. While the inertia of the wheelset rises with rising unsprung mass m_w, the force F_{prim} acting on the unsprung mass remains the same if all other parameters are kept constant. This, in turn, leads to a smaller downwards acceleration $\ddot{z}$ when the flat enters the wheel-rail contact area, and subsequently to a smaller vertical downwards velocity $\dot{z}$ that is reached, leading to a less detrimental impact and smaller maximum acceleration values $\ddot{z}_{max}$ when the wheel is decelerated by the wheel-rail contact. The relevant quantity for the downwards acceleration of the wheelset is the ratio between force acting on it via the primary springs, which is called F_{prim}, and the unsprung mass m_w.

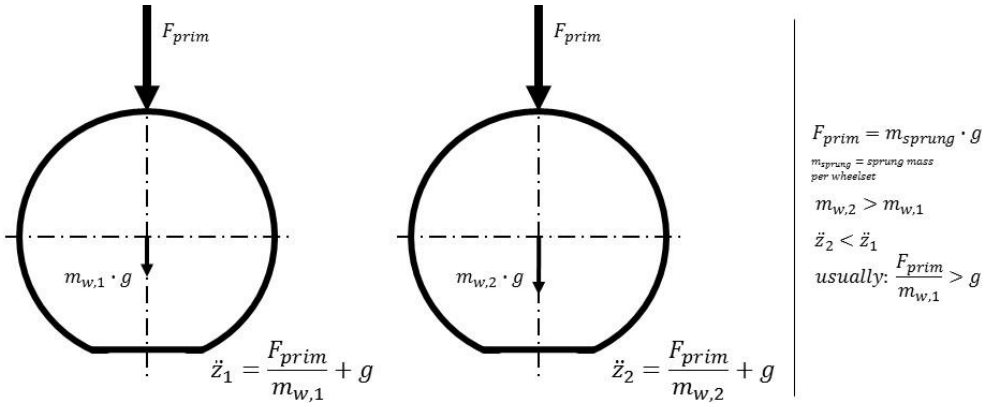

Figure 5-36 - Wheelsets with different unsprung masses m_w are subject to different vertical downwards accelerations $\ddot{z}$ if all other parameters are constant. The Q-force is zero because loss of contact is assumed while the flat is in the wheel-rail contact patch.

Usual values for this ratio are in the range of 40-70 m/s², whereas the gravitational acceleration is around 10 m/s², showing that the unsprung mass has a large effect on the downwards acceleration of the unsprung mass. This is shown in Figure 5-36 for two wheelsets with different unsprung masses m_w, with the same primary spring force F_{prim}. In Figure 5-34, the effects of the wheel radius R alone were investigated, and in Figure 5-35, the unsprung mass m_w alone was investigated. In reality, the unsprung mass m_w changes with the wheel radius R, they are never completely unrelated. For the next investigation, a linear relationship as explained in chapter 5.1.2 is assumed, the unsprung mass m_w being a function of the wheel radius R. The resulting maximum acceleration values $\ddot{z}_{max}$ are shown in Figure 5-37. Since both a larger wheel radius R and a higher unsprung mass m_w lead to smaller amplitudes of the maximum axle box accelerations $\ddot{z}_{max}$, the effects are amplified if the unsprung mass increases with the wheel radius, as can be clearly seen when comparing Figure 5-34, Figure 5-35 and Figure 5-37 with each other. It is worth noting that the rapid decline of the maximum acceleration values $\ddot{z}_{max}$ from Figure 5-37 might be the best representation of reality, because the relationship between the wheel radius R and unsprung mass m_w corresponds to that of actual vehicles, which can be found in the field.

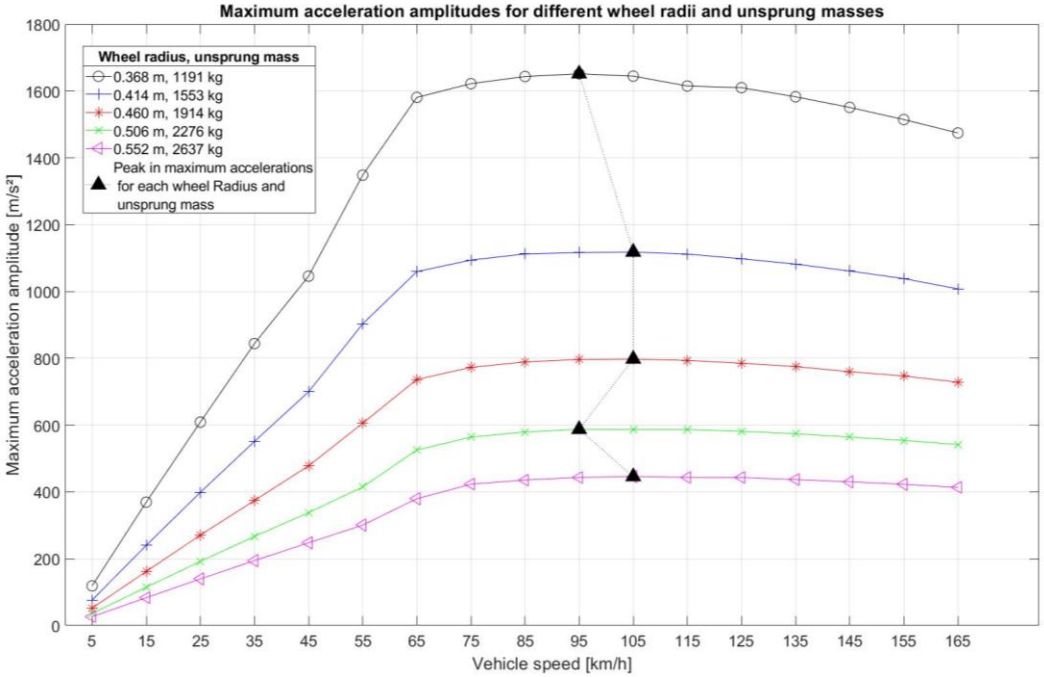

Figure 5-37 - Maximum acceleration amplitudes $\ddot{z}_{max}$ for different wheel radii R, with the unsprung mass m_w being a function of the wheel radius R.

Varying the axle load m_{axle} over the whole vehicle speed range, Figure 5-38 is obtained. A higher axle load leads to an increase in the force F_{prim} that the primary spring exerts on the unsprung mass m_w, which leads to higher downwards accelerations $\ddot{z}$ when the flat enters the wheel-rail contact patch. The higher downwards vertical accelerations $\ddot{z}$ lead to a higher vertical velocity $\dot{z}$ when the wheel is decelerated by the contact with the rail, leading to higher maximum acceleration values $\ddot{z}_{max}$. The effects of a higher axle load m_{axle} are similar to those of a larger flat depth d. However, for a larger flat depth d, the higher vertical velocity $\dot{z}$ of the wheel is the result of a greater drop height resulting from a higher maximum possible vertical displacement z_{max}, whereas for a higher axle load m_{axle}, it is the effect of greater downwards acceleration $\ddot{z}$.

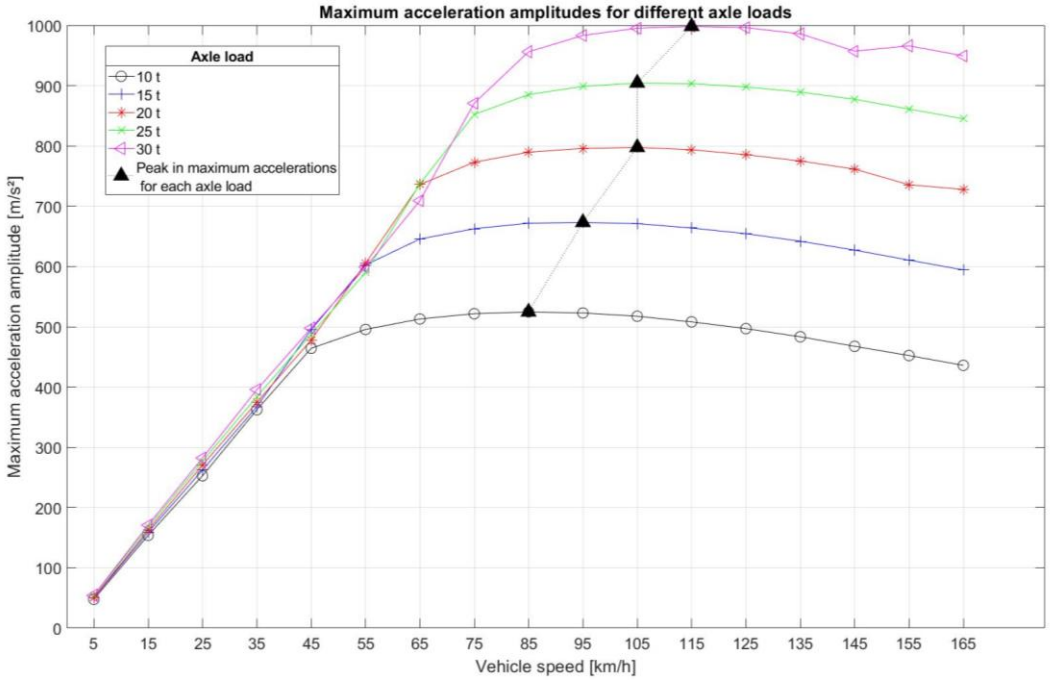

Figure 5-38 - Maximum acceleration amplitudes as a function of the considered axle load in tons.

The effects of the most influential vehicle-track system parameters have been investigated in this section. The results are further interpreted in chapter 6.2.

6 Discussion of the Findings

The results obtained from numerical simulations in chapter 5 are discussed for the two types of out-of-round wheels investigated. If measurements are available, they are compared to simulation results and discrepancies are discussed.

6.1 Polygonization

Regarding polygonization, measurements from the existing literature and data from an unroundness detection algorithm were reviewed. Since the measurements from the literature are only present in a graph and not in numerical form, and constitute measurements of the Q-force, which was not investigated within the scope of this thesis, a comparison of the quantitative simulated and measured results from the literature is omitted in this case. A damage index calculated by an unroundness detection algorithm [72] from axle box acceleration data measured on a polygonized wheelset of a metro train was used to check the plausibility of the calculation results. Since a wheel roundness measurement from the train where the acceleration measurements were performed on was available, this radius deviation data was used as an input for a numeric calculation. From the accelerations that were a result of the numerical simulation, a damage index was calculated using the same algorithm and it was compared against the damage index from the actual vehicle. For a relatively low track stiffness of k_t = 80 MN/m, both damage indices reached similar values of around 6, indicating that the numerical calculations provide quantitatively plausible results.

The calculations, which were performed within the scope of the current thesis in chapter 5.2.2.2, demonstrate that the maximum acceleration amplitudes $\ddot{z}_{max}$ scale linearly with the radius deviation amplitude ΔR_0 of a polygonization of given order n and given vehicle and track properties. This means that, for a given vehicle, track properties and polygonization order n, the axle box accelerations $\ddot{z}$ can actually be limited by limiting the polygonization amplitude ΔR_0, similar to the findings of the analytical analysis in chapter 5.2.1. A simple, linear correlation exists between the peak acceleration amplitude $\ddot{z}_{peak}$ and the track stiffness k_t, as was demonstrated in chapter 5.2.2.3.

However, after an extensive investigation of many parameters of the vehicle-track system in chapter 5.2.2, a simple relation between the acceleration response $\ddot{z}$ and the other vehicle, track and polygonization parameters has not been found. Those parameters are the track stiffness k_t and track mass m_t (chapter 5.2.2.3), the unsprung mass m_w of the vehicle, vehicle speed v and wheel radius R (chapter 5.2.2.4), as well as the order n of the polygonization (chapter 5.2.2.2). This effectively means that, by only limiting the polygonization amplitude ΔR_0, the implicit limit for the axle box accelerations $\ddot{z}_{lim}$ resulting from the limit for the polygonization amplitude ΔR_0 changes for different vehicle properties, track properties and polygon orders. This leads to cases in which the exact same vehicle, having the same polygonized wheels, being operated on two different types of tracks, is implicitly subjected to different axle box acceleration limits $\ddot{z}_{lim}$ that are a result of the polygonization amplitude limits, because the track influences the dynamic response. If the goal is limiting the dynamic loads resulting from a polygonized wheel, and the loads are correlated with the investigated axle box accelerations

(chapter 2.1) this is not a desirable approach, because the dynamic loads change depending on uncontrollable parameters like the track properties.

Additionally, because there is no clear correlation, checking the limit values for the maximum circularity defects Δr_{max} imposed by EN15313 [2] is not possible using axle box accelerations $\ddot{z}$, with no knowledge of the track properties.

6.2 Flats

Regarding flats, axle box measurement data are available to validate the model, which were investigated in chapter 4.2. Therefore, the first numerical calculations were not performed on the base model, but the model was adapted to the properties of the vehicle where the accelerations had been measured in the field. The speed dependency of the maximum accelerations $\ddot{z}_{max}$ is reproduced well by the model, as was found in chapter 5.3.2.2 and as is shown in Figure 6-1, the peak in the maximum accelerations at the vehicle speed v_{crit} corresponds well to the measurements. The speed dependency is a result of the unsprung mass (inertia) m_w. The vertical downward force F_{prim} acting on the wheelset is almost constant for small vertical wheelset movements, as shown in chapter 2.1. The unsprung mass weight force $m_w g$ also acts on the unsprung mass in the same direction as F_{prim} and is constant. This means that during the time of contact loss in the wheel-rail contact, the forces acting on the unsprung mass m_w are almost constant, which leads to a constant downwards acceleration $\ddot{z}$. The higher the vehicle speed v, the shorter the timeframe t in which the flat is within the wheel-rail contact patch.

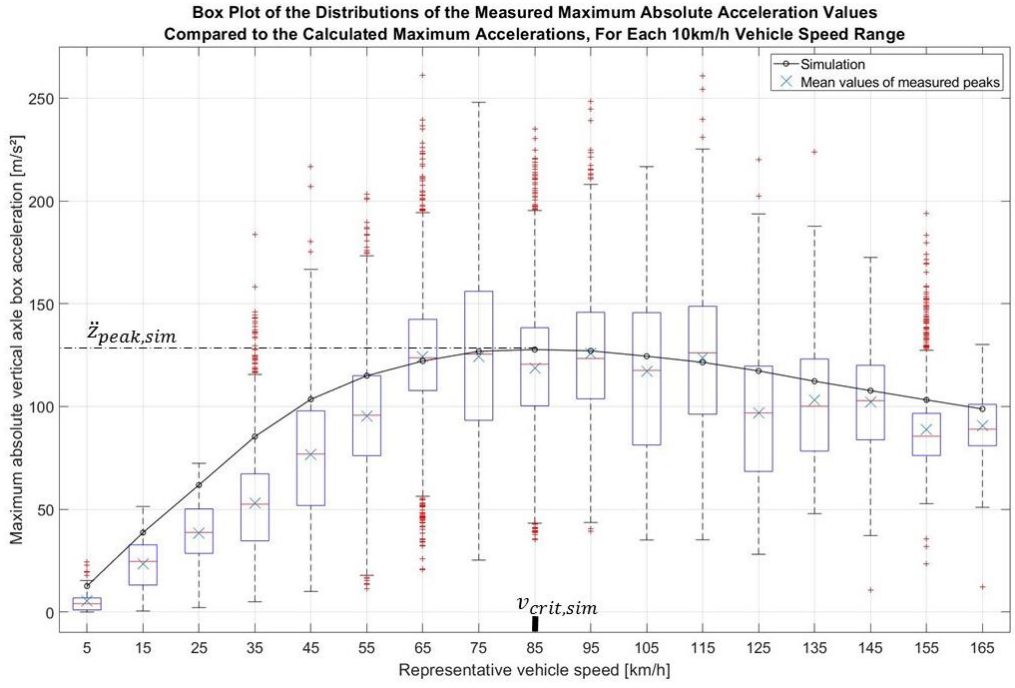

Figure 6-1 - Comparison of the measured and simulated absolute acceleration peaks. The distribution of the measurements is shown as box plots, outliers are marked as red crosses.

Starting at a certain vehicle speed v_{crit}, with a constant downwards acceleration, the amount of time t during which the flat is located in the wheel-rail contact patch becomes so short that there is very little time for the wheel to reach a high downwards velocity $\dot{z}$, which leads to a less detrimental impact and smaller maximum acceleration values $\ddot{z}_{max}$ when the downwards

movement of the wheelset is stopped by the rail. This is the most likely reason for the characteristic peak $\ddot{z}_{peak}$ in the maximum axle box accelerations at the speed v_{crit}. In simple words, because of the inertia of the unsprung mass m_w, the contact is re-established so quickly that it 'does not realize' that loss of contact has even occurred.

A comparison of a measurement and simulation result of a single flat impact, obtained from numerical calculations performed within the current thesis, is shown in Figure 6-2.

It can be found that the maximum absolute acceleration amplitudes $\ddot{z}_{max}$ agree very well, but there is much less agreement of the frequency of the oscillation (chapter 4.2.1) after the impact. What is excited in the current simulation is mainly the P1-resonance.

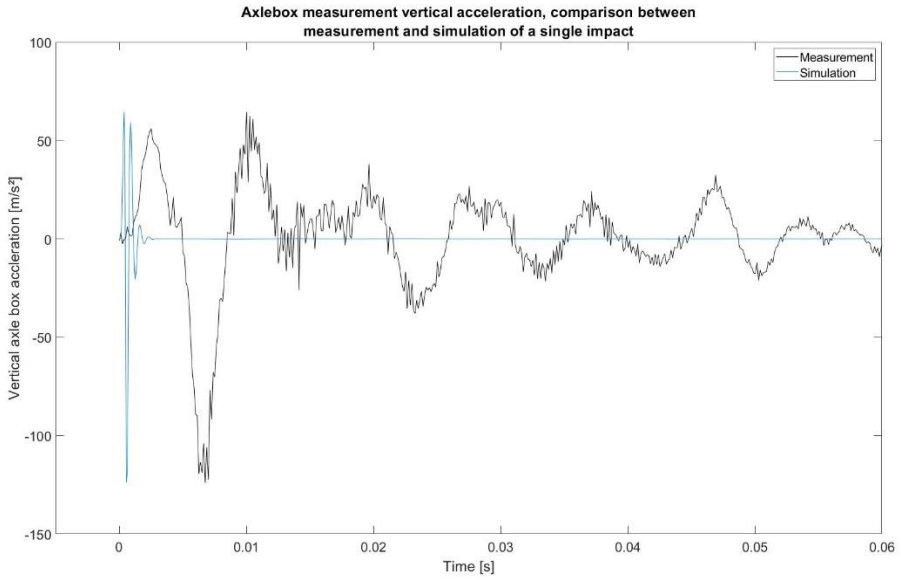

Figure 6-2 - Comparison between measured and simulated axle box acceleration data, obtained from time-step integrations with the numerical model created within the current thesis.

The P1-resonance is the oscillation of the unsprung mass m_w on the contact stiffness c_h [82] and is at around 1400 Hz for the particular set of parameters used in this model. The contact stiffness c_h is nonlinear, but the numeric value is in the order of magnitude of 1000 MN/m. This large contact stiffness c_h dominates the response of the system to the excitation by the flat. Because of the large numerical stiffness c_h and, thus, large eigenfrequency of the wheel-rail contact, the spike in the Q-force when the flat hits the rail is of a very short duration t. This duration time t corresponds to the inverse of the eigenfrequency f_{P1} of the wheel-rail contact, which is about 0.71 ms. As a result of the short duration t of the Q-force peak, the wheelset bending eigenmode almost does not deform in the simulation and is not excited by the flat hitting the rail. Therefore, the oscillation frequency f after the flat impact seen in the measurements cannot be reproduced, unlike the maximum acceleration values $\ddot{z}_{max}$, which have been used for all evaluations. Simulation models from the literature show similarly high oscillation frequencies in the axle box accelerations, ranging from a few hundred to 1000 Hz (e.g. [83] or [84]). More information on why the bending eigenmode oscillation frequency could not be fully reproduced can be found in Appendix B.

The calculation results for maximum acceleration values $\ddot{z}_{max}$ obtained from calculations with the validated model, using other parameters, could be trusted to be accurate because of the

good agreement with the measured data. However, it must be kept in mind that discrepancies between measurements and calculations may be several percent, because of the strong influence of some parameters that are difficult to handle and do not have an exact value, like the contact reference damping d_{eff}, like already stated in chapter 5.3.2.

The investigations on the influences of vehicle, track and flat parameters on the maximum acceleration levels $\ddot{z}_{max}$ were performed using the base model in chapter 5.3.2. The results generally show an increase of maximum acceleration levels $\ddot{z}_{max}$ with the length of the flat l (chapter 5.3.2.3). However, some of the other parameters that were investigated have an even stronger influence on the resulting acceleration levels. Especially the active track rail mass m_r, flat depth d, unsprung mass m_w, wheel radius R, axle load m_{axle} and vehicle speed v also affect the resulting maximum accelerations $\ddot{z}_{max}$, as was found in the sensitivity analysis in chapter 5.3.2.2. This means that limiting the flat length l only limits the maximum acceleration values $\ddot{z}_{max}$ if all other factors are kept constant. If the same flat of length l is present on two vehicles which differ in at least one of the stated parameters, different maximum acceleration values can be expected. Moreover, the speed dependency of the length limits l_{max} of the current standard EN15313 [2], which are smaller for higher maximum vehicle speeds v_{max}, is not sensible from a dynamic standpoint. Higher vehicle speeds v do not necessarily lead to higher maximum values in the axle box accelerations $\ddot{z}_{max}$. The opposite is the case, a decrease in the maximum acceleration values $\ddot{z}_{max}$ with rising vehicle speeds v can be seen if a certain speed v_{crit} is exceeded. Because of the characteristics of the speed dependency and the strong influence of track parameters (chapter 5.3.2.4), judging whether a wheel is fit for service only using the flat length l is not conclusive from a standpoint of dynamic loads, namely accelerations of the axle box. For a given vehicle on a given track, however, limiting the length l of a flat does limit the maximum acceleration response $\ddot{z}_{max}$ it induces, if a newly formed flat is considered.

7 Conclusion and Further Work

For both polygonization and flats, it was found in this investigation that there appears to be no direct correlation between the geometric dimensions l and ΔR_0 of the defects and the resulting dynamic effects. A conclusion for each of the two investigated wheel defects is presented in the following subchapters 7.1 and 7.2. Concluding the task of performing a market analysis and investigating the available automatic wheelset inspection systems, it becomes clear that most of the systems found assess measurements of dynamic quantities, which are not limited by the current European standard EN15313.

7.1 Polygonization

Completing the task to check for a simple conversion from the circularity defect limit values Δr_{max} to maximum acceleration values $\ddot{z}_{max}$, such a correlation could not be found because of the complex, mostly nonlinear relationships between vehicle and track parameters and the acceleration response. Especially parameters that are difficult to assign a value to and change continuously, like the track stiffness k_t, have a strong influence on the acceleration response $\ddot{z}$ of the wheelset axle box. Additionally, the track properties can change very rapidly along the track length s. Determining the polygonization amplitude ΔR_0 from the axle box accelerations $\ddot{z}$ is not explicitly possible because the same accelerations $\ddot{z}$ are observed for different sets of parameters of the vehicle-track system. An example for this are two vehicles which only differ in the order n of their polygonization by a factor of two, driving on two different tracks, which have P2-resonance frequencies, which differ by a factor of two as well. In this example, the peak $\ddot{z}_{peak}$ in the maximum acceleration amplitudes occurs at the same vehicle speed v. Additionally, the influence of the vehicle speed v is strongly nonlinear and cannot be easily accounted for, like in the analytical analysis in chapter 5.2.1. This also means that assessing whether or not a wheel is fit for service using the circularity defect Δr is not conclusive from the standpoint of dynamic loads. Radius deviations do not cause component failure, but overloading does [85]. Since no direct correlation exists between the circularity defect Δr and the maximum axle box accelerations $\ddot{z}_{max}$, the circularity defect Δr appears not to be a good method to assess the potential damage of wheelsets, completing the task of assessing the current limits provided in the standard EN15313 [2]. Therefore, the addition of limit values $\ddot{z}_{lim}$ for the resulting accelerations $\ddot{z}$ to the standard could be considered, simply because they contain more information about the dynamic processes within the vehicle-track-system, and not just the out-of-roundness, which only constitutes the excitation.

Further work concerning polygonized wheels and their dynamic responses could deal with expanding the track model to more closely represent the track types, which can be found in the field. This could be done by introducing a state-dependent instead of a linear track model, as well as modeling the rail as a beam. Additionally, sleepers could be introduced to the model. To parametrize this new model, actual track measurements could be used. A validation of the model with measured axle box accelerations $\ddot{z}$ from a track and vehicle with known properties is another working item, which could be addressed in the future.

7.2 Flats

The task to find out whether a simple correlation exists between the length l of a flat and the accelerations $\ddot{z}$ it induces has led to the conclusion that no direct correlation between the two quantities has been found. The influence of uncontrollable parameters, like the track properties, on the resulting maximum accelerations $\ddot{z}_{max}$, has found to be too large. Furthermore, the track properties may change continuously along the track, but can also change very rapidly if a vehicle moves to a different type of track (e.g. ballast track and slab track). Another important factor is the unknown flat depth d. If a flat has been present on the vehicle for some time, it can be worn out around the edges, and may not be perfectly flat, even though it maintains its visual length l. This change in the radius deviation $\Delta R(\beta)$ along the circumference changes the dynamic response caused by the flat, as has been shown in chapter 5.3.2.3. Therefore, the flat length l cannot be deduced from acceleration measurements $\ddot{z}$. This conversely also means that the flat length l appears not to be a good measure for the axle box accelerations $\ddot{z}$ a flat causes, which in turn means it is not a good measure to assess the potential damage of the wheelset, completing the task of assessing the current tread defect length limits from EN15313. Instead, the dynamic effects themselves, namely the axle box accelerations $\ddot{z}$, could be used to assess whether a wheelset is still fit for service. They do not only contain information about the unroundness, but as well contain information about the dynamic processes resulting from it.

Further work may deal with creating a more detailed track model, using beam elements to model the rails and modeling discrete sleepers. Moreover, a further investigation into the excitation of the wheelset bending eigenmode could be conducted, to try to replicate not only the maximum acceleration values $\ddot{z}_{max}$, but also the oscillation frequency f. It may be investigated whether the current wheel-rail contact model is suitable for replicating frequencies outside of the frequency band that is relevant for vehicle dynamics, which starts at 0 Hz and ends at around 20 Hz. A more detailed study on the shape of new and worn flats might be conducted.

List of References

[1] H. Hertz, "Ueber die Berührung fester elastischer Körper," *Journal für die reine und angewandte Mathematik 92,* pp. 156-171, 1881.

[2] *EN 15313:2016; European technical standard; In-service wheelset operation requirements,* 2016.

[3] L. Afferrante and M. Ciavarella, "Corrugation Models and the Roaring Rails Enigma: A Simple Analytical Contact Mechanics Model Based On a Perturbation of Carter's Solution," *Journal of Mechanics of Materials and Structures, Vol. 4 No. 2,* pp. 191-209, February 2009.

[4] Siemens, [Online]. Available: https://www.siemens.com/press/de/pressebilder/index.php?content=EW. [Accessed 18 May 2019, 13:00 CET].

[5] A. Haigermoser, Schienenfahrzeuge Vorlesungsskriptum (Rail Vehicles Lecture Manuscript), Graz: TU Graz, 2002.

[6] R. Deuce, A. Ekberg and E. Kabo, "Mechanical deterioration of wheels and rails under winter conditions – mechanisms and consequences," *Journal of Rail and Rapid Transit,* 2018.

[7] A. Johansson and J. Nielsen, "Out-of-round railway wheels - wheel-rail contact forces and track response derived from field tests and numerical simulations," *Proceedings of the Institution of Mechanical Engineers Vol. 217 Part F: Journal Rail and Rapid Transit,* pp. 135-146, 2003.

[8] A. Johansson, Dissertation: Out-of-Round Railway Wheels - Causes and Consequences, Göteborg, Sweden: Chalmers University of Technology, 2005.

[9] K. Knothe and S. Stichel, Schienenfahrzeugdynamik, Berlin Heidelberg: Springer Verlag, 2003.

[10] Dassault Systemes Simulia Corp., "SIMPACK 2018x Documentation," 2017.

[11] J. C. O. Nielsen and A. Johansson, "Out-of-round railway wheels - a literature survey," *Proceedings of the Institution of Mechanical Engineers Vol 214 Part F: Journal of Rail and Rapid Transit,* pp. 79-91, 2000.

[12] Y. Wu, X. Du, H.-j. Zhang, Z.-f. Wen and X.-s. Jin, "Experimental analysis of the mechanism of high-order polygonal wear of wheels of a high-speed train," *Journal of Zhejiang University-SCIENCE A 18(8),* pp. 579-592, 2017.

[13] L. Baeza, A. Roda, J. Carballeira and E. Giner, "Railway Train-Track Dynamics for Wheelflats with Improved Contact Models," *Nonlinear Dynamics Vol. 45,* pp. 385-397, 2006.

[14] R. Dukkipati and R. Dong, "The Dynamic Effects of Conventional Freight Car Running over a Dipped-joint," *Vehicle System Dynamics, Vol. 31,* pp. 95-111, 1999.

[15] R. Dukkipati and D. Renguang, "Impact Loads due to Wheel Flats and Shells," *Vehicle System Dynamics, Vol. 31,* pp. 1-22, 1999.

[16] S. Newton and R. Clark, "An investigation into the dynamic effects on the track of wheelflats on railway vehicles," *Journal of Mechanical Engineering Science, Vol. 21(4),* p. 287–297, 1979.

[17] R. Zunsong, "An investigation on wheel/rail impact dynamics with a three-dimensional flat model," *Vehicle System Dynamics, Vol. 57, No.3,* pp. 369-388, 2019.

[18] R. Uzzal, A. Ahmed and R. Bhat, "Modelling, validation and analysis of a three-dimensional railway vehicle–track system model with linear and nonlinear track properties in the presence of wheel flats," *Vehicle System Dynamics, Vol. 51, No. 11,* pp. 1695-1721, 2013.

[19] M. J. Steenbergen, "The role of the contact geometry in wheel–rail impactdue to wheel flats," *Vehicle System Dynamics 46(8),* pp. 713-737 , 2008.

[20] M. Steenbergen, "The role of the contact geometry in wheel–rail impact due to wheel flats: Part II," *Vehicle System Dynamics, Vol. 46,* pp. 713-737, 2008.

[21] O. Prof. Dr. Ing. Krettek, "UNRA Abschlussbericht," 1992.

[22] "SCHADKATALOG RÄDER / RADSATZWELLEN / RADSÄTZE - Teil 1," Internationaler Eisenbahnverband, 2007.

[23] *Hegenscheidt-MFD GmbH,* Hegenscheidt Platz, 41812 Erkelenz, Germany, Tel: +49 2431 860.

[24] *MRX Technologies, Siemens AG Affiliate,* 24 Drummond Place West, Perth WA 6005, Australia, Tel: +61 8 9227 4588.

[25] *NEXTSENSE GmbH,* Straßganger Str. 295, 8053 Graz, Austria, Tel: +43 316 2324000.

[26] *BeenaVision,* 600 Pinnacle Ct, Norcross, GA. 30071, USA, Tel: +1-678-597-3156.

[27] *Bombardier Transportation,* Eichhornstraße 3, 10785 Berlin, Germany, Tel.: +49 30 986 07 0.

[28] *IBM,* 2 Riverway, Houston, TX 77056, USA, Tel: +1 713-297-7900.

[29] *MER MEC S.p.A.,* Via Oberdan, 70, 70043 Monopoli (BA), Italy, Tel: +39 080 9171.

[30] *RIFTEK LLC,* 22 Logoisky tract, 220090 Minsk, Republic of Belarus, Tel: +375-17-357-36-57.

[31] *Hottinger Baldwin Messtechnik GmbH,* Lemböckgasse, 63/2 A-1230 Wien, Austria, Tel: +43 1 865 84 41.

[32] *DB Systemtechnik GmbH,* Pionierstraße 10, 32423 Minden (Westf), Germany, Tel: +49 571 3935550.

[33] *Schenck Process Europe GmbH,* Pallaswiesenstraße 100, 64293 Darmstadt, Germany, Tel: +49 6151 15310.

[34] *voestalpine SIGNALING Siershahn GmbH,* Bahnweg 1, 56427 Siershahn, Deutschland, Tel: +49 2623 60860.

[35] *INNOtec Systems GmbH,* Am Hellbrunn 57, 55234 Eppelsheim, Germany, Tel: +49 6735 9417590.

[36] *Lloyd's Register Rail Europe BV,* Catharijnesingel 33, 3511 GC Utrecht, Netherlands, Tel: +31 30 7524 711 .

[37] *Österreichische Bundesbahnen AG,* Am Hauptbahnhof 2, 1100 Wien, Austria, Tel: +43 1 93000 0.

[38] *Perpetuum Ltd,* Unit 7 The Quadrangle, Abbey Park, Abbey Industrial Estate, Romsey, UK, Tel: +44 (0)23 8076 5888.

[39] *PCB Synotech GmbH,* Porschestraße 20, 41836 Hückelhoven, Germany, Tel: +49 2433 4444400.

[40] *SKF,* SE-415 15, Göteborg, Sweden, Tel: +46 31 337 10 00 .

[41] *I-moss NV,* Corbielaan 5, 3060 Bertem, Belgium, Tel: +32 16 369 885.

[42] *RAFAMET S.A.,* Ul. Staszica 1, 47-420 Kuźnia Raciborska, woj. śląskie, Poland, Tel: +48 327 213 300.

[43] *Siemens Mobility GmbH,* Leberstraße 34, 1110 Vienna, Austria, +43 517 070.

[44] *PATENTES TALGO S.L.U.,* Paseo del Tren Talgo 2, 28290 Las Matas - Madrid, Spain.

[45] *Müller-BBM Austria GmbH,* Opernring 4, 8010 Graz, Austria, Tel: +43 316 32 55 22-0 .

[46] *Deutzer Technische Kohle GmbH,* Lindenallee 16, 15738 Zeuthen , Tel: +49 33762 2287 123.

[47] *Frauscher Sensortechnik GmbH,* Gewerbestraße 1, 4774 St. Marienkirchen, Austria, Tel: +43 7711 2920-0.

[48] *Wabtec Corporation,* 1001 Air Brake Avenue, Wilmerding, PA 15148 - USA, Tel: +1 888-264-0011.

[49] Hegenscheidt MFD, [Online]. Available: https://www.hegenscheidt-mfd.com/railway/radsatzdiagnose-system-argus-ii/. [Accessed 25 February 2019, 13:20 CET].

[50] Hegenscheidt MFD, [Online]. Available: https://www.hegenscheidt-mfd.com/wp-content/uploads/2011/07/Argus_04.jpg. [Accessed 25 February 2019, 12:35 CET].

[51] E. Toensing, Interviewee, [Interview]. 24 July 2018.

[52] NEXTSENSE GmbH, [Online]. Available: https://www.nextsense-worldwide.com/de/branchen/bahn.html. [Accessed 26 February 2019, 13:00 CET].

[53] [Online]. Available: https://rail.trimble.com/wp-content/uploads/Datasheet-Trimble-TreadView-English-US-Letter.pdf. [Accessed 26 February 2019, 13:09 CET].

[54] "AVIS," [Online]. Available: https://pdfs.semanticscholar.org/d973/3a5babb56298ac84263dd8c37e98b407602f.pdf. [Accessed 26 February 2019, 13:15 CET].

[55] MERMEC, [Online]. Available: http://www.mermecgroup.com/de/pageview2.php?i=87&sl=1. [Accessed 26 February 2019, 13:20 CET].

[56] RIFTEK Ltd., [Online]. Available: https://riftek.com/eng/products/~show/instruments/railway-devices/automated-systems-for-wheel-sets-control. [Accessed 26 February 2019, 13:30 CET].

[57] P. Mittermayr, Interviewee, *ÖBB.* [Interview]. 8 May 2018.

[58] "Argos-Systems," Hottinger Baldwon Messtechnik GmbH, [Online]. Available: http://www.argos-systems.eu/?page_id=2744. [Accessed 17 January 2019, 13:52 CET].

[59] Hottinger Baldwin Messtechnik, [Online]. Available: http://www.argos-systems.eu/?page_id=2486. [Accessed 17 January 2019, 14:11 CET].

[60] *Siemens-Internal Commercial System Specification Document for MRX WDMS*, 2016.

[61] "DB Systemtechnik," [Online]. Available: https://www.db-systemtechnik.de/resource/blob/1664918/7ca00abef0bbd915f8528146e061036b/27_p_D_detektionsanlage_dafur-data.pdf. [Accessed 26 February 2019, 13:35 CET].

[62] Schenck Process GmbH, [Online]. Available: https://www.schenckprocess.com/de/produkte/gleisfahrzeuge-raddiagnose. [Accessed 26 February 2019, 13:40 CET].

[63] INNOtec Systems GmbH, [Online]. Available: http://www.innotec-systems.de/index.php/lasca.html . [Accessed 26 February 2019, 13:48 CET].

[64] "Voestalpine," [Online]. Available: https://www.voestalpine.com/signaling/static/sites/signaling/.downloads/produkte/wdd-wim/voestalpine_signaling_atlas_fo_diagnose_von_raddefekten_und_ladungsgewichten.pdf. [Accessed 26 February 2019, 13:55 CET].

[65] "TagMaster North America," [Online]. Available: https://tagmasterna.com/wp-content/uploads/2016/05/Gotcha.pdf. [Accessed 27 March 2019, 16:16 CET].

[66] F. Schmid, Wheel Rail Best Practice Handbook, Birmingham: Network Rail, 2010.

[67] Perpetuum Ltd., [Online]. Available: https://perpetuum.com/rail-applications/. [Accessed 26 February 2019, 14:00 CET].

[68] "PCB Synotech GmbH," [Online]. Available: https://www.synotech.de/produkte_skript/downloads/marketing/SYN_Sensoren%20fuer%20Bahn-%20und%20Schienenverkehr_Applikationsbroschuere_DEU_1409.pdf. [Accessed 26 February 2019, 14:02 CET].

[69] "SKF," [Online]. Available: https://www.skf.com/binary/21-302819/17140_2%20EN%20-%20Insight%20PR_tcm_12-302819.pdf. [Accessed 26 February 2019, 14:08 CET].

[70] "i-moss NV," [Online]. Available: https://www.i-moss.com/sites/default/files/2016-06/WORM_EN_0.pdf. [Accessed 26 February 2019, 14:10 CET].

[71] RAFAMET S.A., [Online]. Available: https://www.rafamet.com/en/products/machines-for-railways/diagnostic-systems/detection-of-flat-spots-on-wheel-profile. [Accessed 26 February 2019, 14:14 CET].

[72] "Siemens Mobility GmbH," [Online]. Available: http://www.schienenfahrzeugtagung.at/download/PDF2014/DiN03-Mooshammer_Woels.pdf. [Accessed 5 April 2019, 12:20 CET].

[73] Talgo, [Online]. Available: https://www.talgo.com/en/maintenance-equipment/. [Accessed 26 February 2019, 14:16 CET].

[74] *Siemens-Internal Commercial System Specification Document for Talgo D.S.R.,* 2016.

[75] "Mueller BBM," [Online]. Available: http://www.muellerbbm.com/fileadmin/user_upload/gmbh/Bilder/Broeschueren/MBBM-ARRoWWheelMS_en.pdf. [Accessed 26 February 2019, 14:20 CET].

[76] Deutzer Technische Kohle GmbH, [Online]. Available: http://deutzer.de/services/strassenbahn/211-flachstellen-und-polygonermittlung. [Accessed 26 February 2019, 14:21 CET].

[77] Frauscher, [Online]. Available: https://www.frauscher.com/de/ueberwachen/. [Accessed 26 February 2019, 14:25 CET].

[78] Wabtec Corporation, [Online]. Available: https://www.wabtec.com/products/7314/railbam%C2%AE-bearing-acoustic-monitor. [Accessed 5 April 2019, 10:56 CET].

[79] T. Meinders and P. Meinke, "Rotor Dynamics and Irregular Wear of Elastic Wheelsets," Institute B of Mechanics, University of Stuttgart, Stuttgart, Germany.

[80] K. Ellermann, Mehrkörperdynamik Vorlesungsskriptum (Multi-Body-Dynamics Lecture Macuscript), Graz: TU Graz, 2014.

[81] "Simpack Rail Information Page," [Online]. Available: http://www.simpack.com/industrial_sectors_rail.html. [Accessed 19 January 2019; 16:14 CET].

[82] Andersson, Event, M. Berg and S. Stichel, Rail Vehicle Dynamics, Stockholm: Railway Group KTH, Centre for Research and Education in Railway Engineering, 2005.

[83] J. Xuesong, "An investigation into the mechanism of the polygonal wear of metro train wheels and its effect on the dynamic behaviour of a wheel/rail system," *Vehicle System Dynamics, Vol. 50, No. 12,* pp. 1817-1834, December 2012.

[84] L. Jing, "Further study on the wheel–rail impact response induced by a single wheel flat: the coupling effect of strain rate and thermal stress.," *Vehicle System Dynamics Vol. 55, No. 12,* pp. 1946-1972, 2017.

[85] V. Läpple, Einführung in die Festigkeitslehre, 3. Auflage, Wiesbaden: Vieweg+Teubner Verlag, 2011.

[86] J. Kalker, "A Fast Algorithm for the Simplified Theory of Rolling Contact," *Journal Vehicle System Dynamics Vol. 11,* pp. 1-13, 1982.

[87] F. Heitmeier, Maschinendynamik I Vorlesungsskriptum (Machine Dynamics Lecture Manuscript), Graz: TU Graz, 2015.

[88] K. Strehmel, R. Weiner and H. Podhaisky, Numerik gewöhnlicher Differentialgleichungen, Springer Spektrum, 2012.

List of Tables

List of Figures

All figures for which no source is declared in the figure caption were created by the author of the present thesis. All figures which were created by the author, especially explanations of existing automatic wheelset inspection systems, represent the author`s interpretation of the depicted situation.

Appendices

Appendix A

Description of the MBS Model

The vehicle model is a modified version of the *SIMPACK* training model, an explanation of which is found in the documentation [10]. It is equipped with a total of two secondary springs, four primary springs, four axle guide bearings, four primary vertical dampers, two secondary vertical dampers, two lateral and two anti-yaw dampers, as well as an anti-roll bar, a traction rod and a bump stop for each bogie, respectively.

Table A-4 - Mass properties of the base model. Moments of inertia are given with reference to the COG of each mass, while the *x*-, *y*- and *z*-coordinates give the position of each mass relative to the inertial system.

Description	**Mass [kg]**	**I_{xx} [kgm²]**	**I_{yy} [kgm²]**	**I_{zz} [kgm²]**	***x* [m]**	***y* [m]**	***z* [m]**
Car body	67 111	29 998	129 932	1 229 932	0	0	-1
Bogie frame front	2 615	1 722	1 476	3 076	9.5	0	-0.6
Bogie frame back	2 615	1 722	1 476	3 076	-9.5	0	-0.6
Axle guide 11	10^{-6}	10^{-6}	10^{-6}	10^{-6}	10.595	1	-0.497
Axle guide 12	10^{-6}	10^{-6}	10^{-6}	10^{-6}	10.595	-1	-0.497
Axle guide 21	10^{-6}	10^{-6}	10^{-6}	10^{-6}	8.405	1	-0.497
Axle guide 22	10^{-6}	10^{-6}	10^{-6}	10^{-6}	8.405	-1	-0.497
Axle guide 31	10^{-6}	10^{-6}	10^{-6}	10^{-6}	-8.405	1	-0.497
Axle guide 32	10^{-6}	10^{-6}	10^{-6}	10^{-6}	-8.405	-1	-0.497
Axle guide 41	10^{-6}	10^{-6}	10^{-6}	10^{-6}	-10.595	1	-0.497
Axle guide 42	10^{-6}	10^{-6}	10^{-6}	10^{-6}	-10.595	-1	-0.497
Wheelset 1	1 915	740	74	740	10.78	0	-0.460
Wheelset 2	1 915	740	74	740	8.22	0	-0.460
Wheelset 3	1 915	740	74	740	-8.22	0	-0.460
Wheelset 4	1 915	740	74	740	-10.78	0	-0.460

Table A-5 - Force element properties of all force elements mainly acting in the *z*-direction of the base model.

Suspension component (force element used)	Stiffness [N/m]	Damping [Ns/m]
Primary spring (component force element)	1 220 000	-
Primary damper (component force element)	600 000	Nonlinear, see Figure A-1 for reference
Axle guide bearing (component force element)	12 000 000	3 000
Secondary spring (component force element)	430 000	-
Secondary vertical damper (serial spring and damper)	6 000 000	25 000

Table A-6 - Mass and force element properties of the base track model.

Track model		Mass [kg]	Stiffness [N/m]	Damping [Ns/m]
One-mass spring-damper		330	150 000 000	188 000
Two-mass spring-damper	Rail	120	300 000 000	188 000
	Sleeper and ballast	300	150 000 000	188 000

Table A-7 - Track parameters used for the validation model.

Track Model element	Mass [kg]	Stiffness [N/m]	Damping [Ns/m]
Rail	80	200 000 000	188 000
Sleeper and ballast	150	150 000 000	188 000

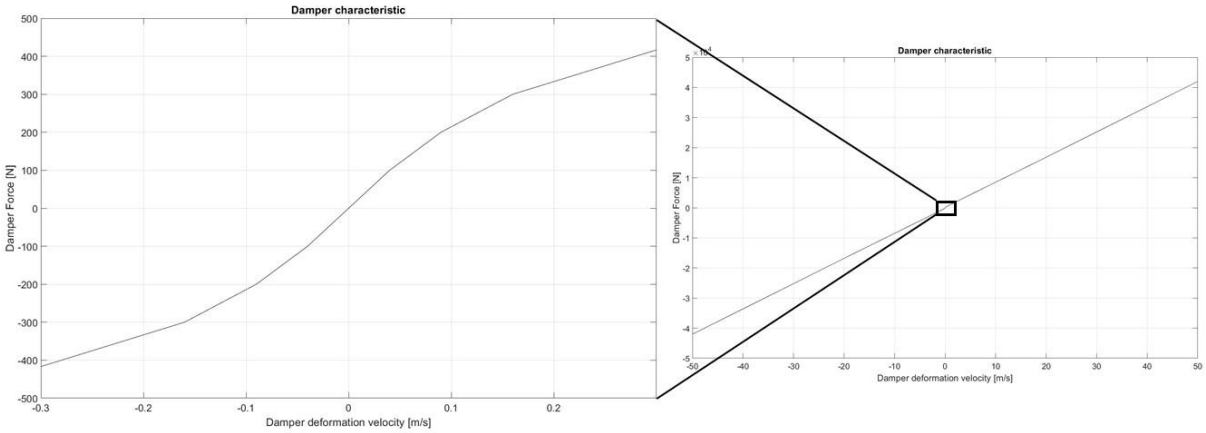

Figure A-1 - Damper characteristic of the primary vertical damper in the base model.

Appendix B

Literature Survey

As explained in chapter 5.3.2, the stiff wheel-rail contact, with numerical stiffnesses of up to 2000 MN/m, was the suspected reason for the difficulties in exciting the eigenmode and inducing an oscillation with the first wheelset bending eigenfrequency. The maximum acceleration values $\ddot{z}_{max}$, on the other hand, have been replicated very well. Many options have been investigated to remedy the situation, yet none of the investigated solutions was able to help excite the eigenmode of the wheelset. A literature review has been performed, finding similar, high-frequency oscillations of the wheel-rail normal force Q (P1-resonance frequency f_{P1}) and axle box accelerations $\ddot{z}$, resulting from the high contact stiffness c_h. The frequencies found in the literature are shown in Table B-8.

Table B-8 – Frequency values of the wheel-rail contact force or axle box acceleration oscillations, from simulation models from the literature.

Wheel-rail force or acceleration oscillation frequency [Hz]	Source
~330	[18]
~555	[16]
~588	[83]
~1000	[84]

Investigations with the model of the current thesis

Investigations with only the wheelset model from the model of the current thesis were performed, the weight force of the vehicle acting on the wheelset via the primary springs was replaced by a constant force F_{prim}, as shown in Figure B-2. Instead of a flat, an additional force $Q_{excitation} = Q_{exc}$ in the rail wheel contact was applied to simulate the peak in the Q-force induced by the flat. The goal was to find out what behavior the Q-force would need to show in order to excite the bending eigenmode of the wheelset, as observed in the measurements.

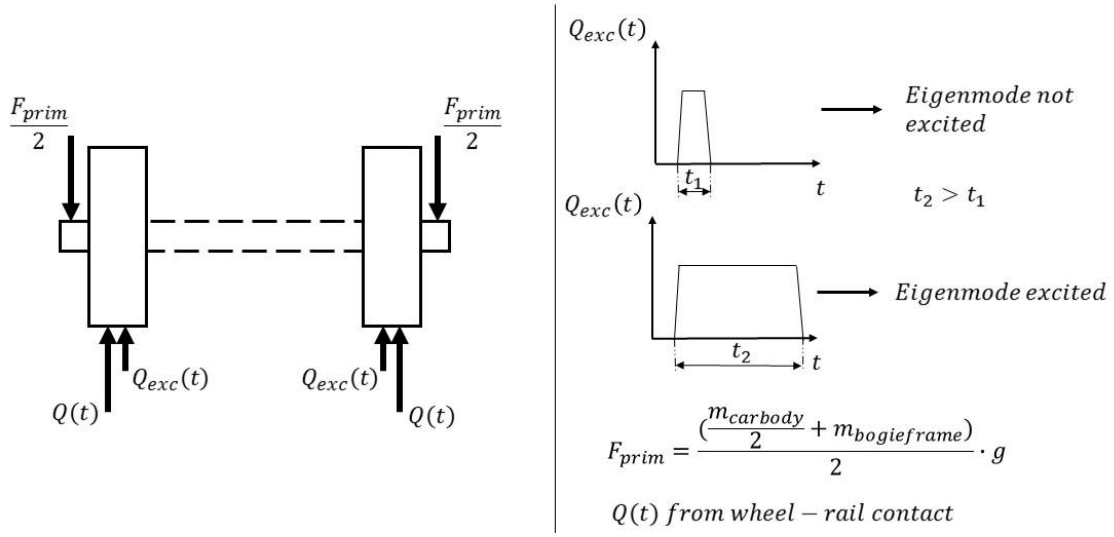

Figure B-2 - Investigations on the excitation of the first bending eigenmode.

The result of this investigation was that the duration t of the Q-force acting in the wheel-rail contact patch is of major importance for the excitation of the wheelset eigenfrequency. Owing to the short Q-force peak because of the high contact stiffness c_h, the bending eigenmode could not be excited. Many different approaches have been used to counteract this issue, they are listed and explained in Table B-9. Since the high-frequency oscillation resulting from the wheel-rail contact model could not be eliminated, this investigation will deal with the resulting maximum acceleration amplitudes, which correspond very well to the measurements, as discussed in chapter 6.2.

Table B-9 - Approaches to excite the bending eigenmode.

Approach	Result
Varying the reference damping in the wheel-rail contact (normal force calculation)	No difference or unrealistic Q-force or axle box acceleration amplitudes
Varying the stiffness of the wheel-rail contact by changing the Young`s modulus considered in the *Hertzian* normal force calculation	Unrealistic Q-force or axle box acceleration amplitudes
Varying the track parameters in wide ranges (stiffness, damping of the force elements and varying the mass)	No difference or unrealistic Q-force or axle box acceleration amplitudes
Applying a large radius to the flat, effectively making it into a long local defect	The bending eigenmode could be excited, albeit the speed dependency of the axle box accelerations with a peak at a certain vehicle speed could not be reproduced, the increase was monotonic over the whole vehicle speed range
Use of a stiff track	Eigenfrequency of the wheel-rail contact can be lowered, but not to the required extent
Modeling the flat using a track excitation instead of applying an unroundness to the wheel	No change in results
Using the Discrete Elastic contact (see *SIMPACK* documentation for reference [10])	Slightly different results, but no general change in the frequency domain can be observed
Reducing the vehicle speed, so no loss of contact occurs in the wheel-rail contact	Main oscillation still occurs at a high frequency
Checking whether the axle bearing or the acceleration sensor mount could be the source of the characteristic frequency of 110-117 Hz in the measurements instead of the wheelset bending eigenmode	Both the bearing and the acceleration sensor mount are too stiff to oscillate at a frequency this low

Appendix C

Fourier Analyses of measured acceleration data packets at different vehicle speeds, each of which is one second long, are shown in Figure C-3, Figure C-4 and Figure C-5. These are further examples for the explanations from chapter 4.2.

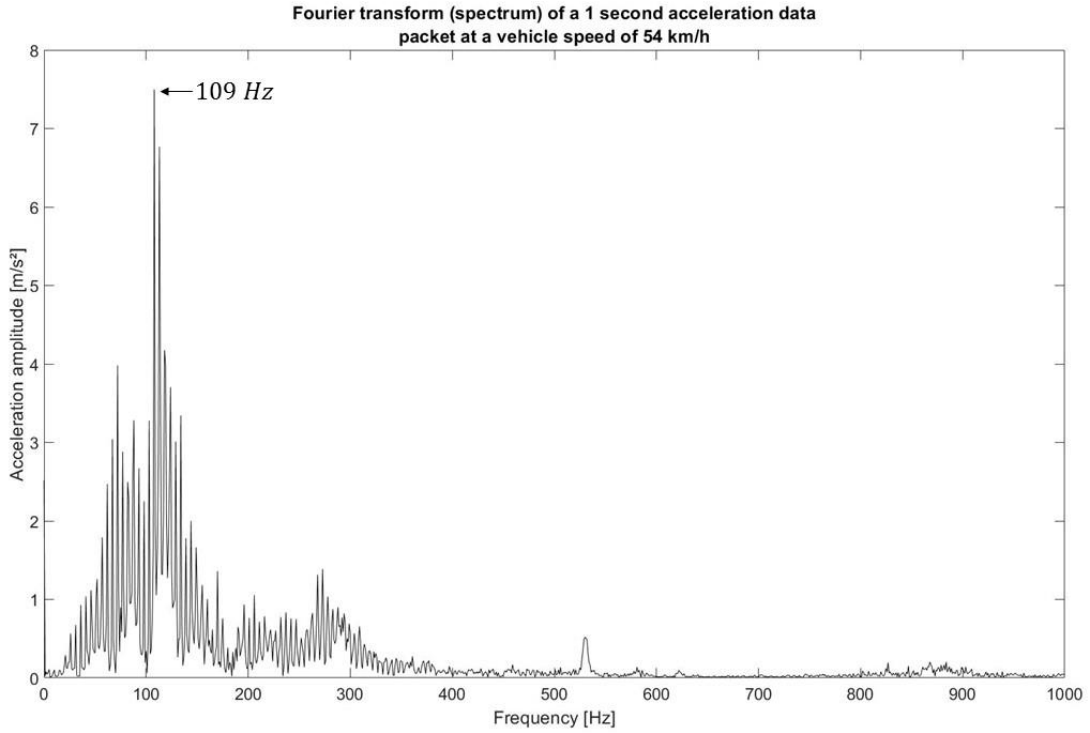

Figure C-3 - FFT of an acceleration data packet, which is one second long, at a vehicle speed of 54 km/h. The maximum peak is located at 109 Hz.

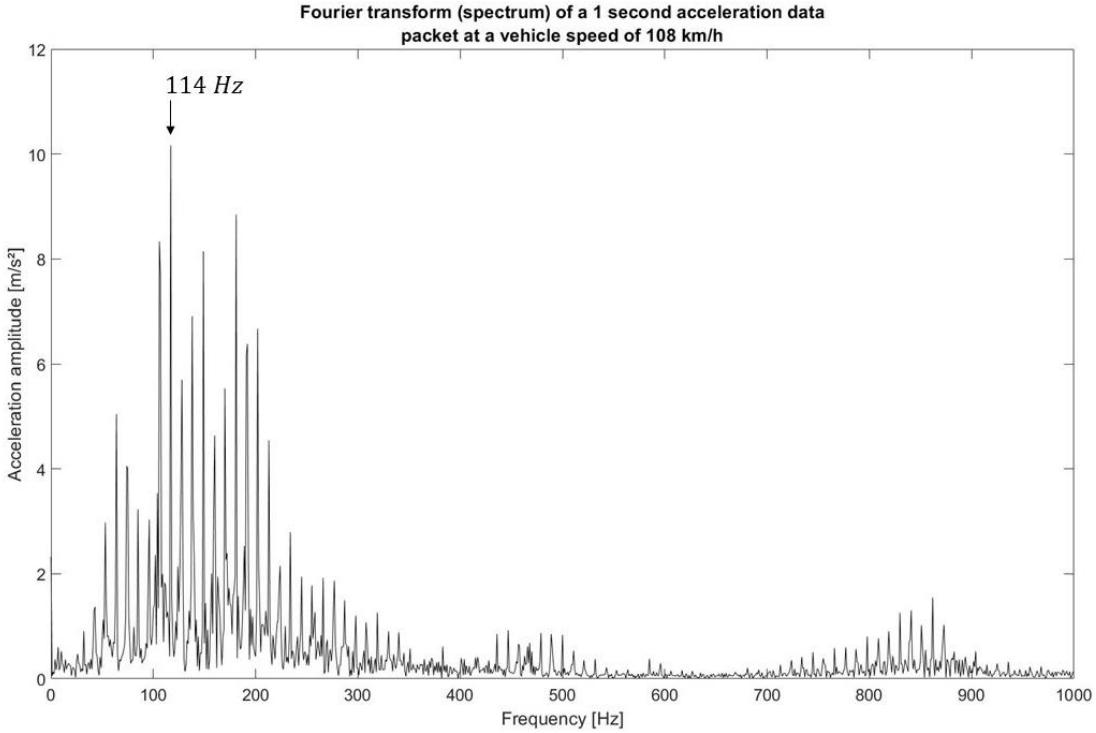

Figure C-4 - FFT of an acceleration data packet, which is one second long, at a vehicle speed of 108 km/h. The maximum peak is located at 114 Hz.

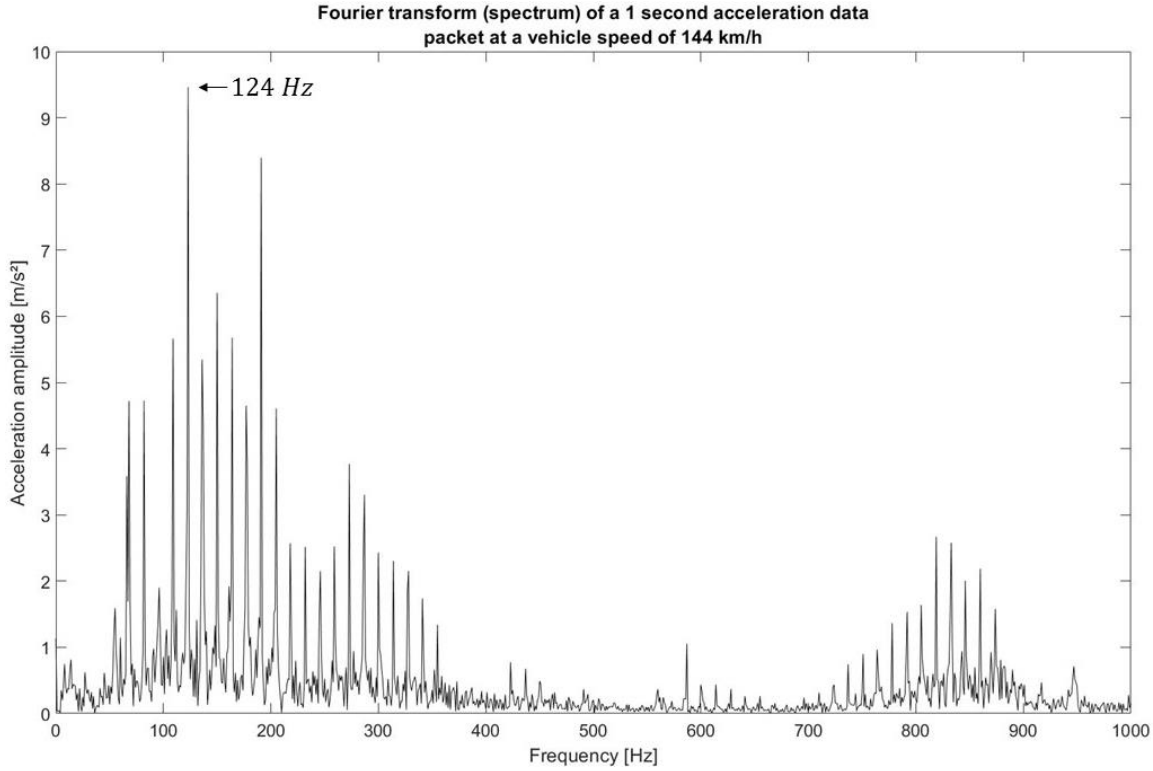

Figure C-5 - FFT of an acceleration data packet, which is one second long, at a vehicle speed of 144 km/h. The maximum peak is located at 124 Hz.